Titre: Title:	Optimization of Mechanical Properties for Laser Powder Bed Fusion A20X Alloy
Auteur: Author:	Heidar Karimialavijeh
Date:	2024
Type:	Mémoire ou thèse / Dissertation or Thesis
Référence: Citation:	Karimialavijeh, H. (2024). Optimization of Mechanical Properties for Laser Powder Bed Fusion A20X Alloy [Thèse de doctorat, Polytechnique Montréal]. PolyPublie. https://publications.polymtl.ca/59455/

URL de PolyPublie: PolyPublie URL:	https://publications.polymtl.ca/59455/
Directeurs de recherche: Advisors:	Étienne Martin
Programme: Program:	Génie mécanique

POLYTECHNIQUE MONTRÉAL

affiliée à l'Université de Montréal

Optimization of mechanical properties for laser powder bed fusion A20X alloy

HEIDAR KARIMIALAVIJEH

Département de génie mécanique

Thèse présentée en vue de l'obtention du diplôme de Philosophiæ Doctor

Génie mécanique

Septembre 2024

POLYTECHNIQUE MONTRÉAL

affiliée à l'Université de Montréal

Cette thèse intitulée :

Optimization of mechanical properties for laser powder bed fusion A20X alloy

présenté par **Heidar KARIMIALAVIJEH**

en vue de l'obtention du diplôme de Philosophiæ Doctor

a été dûment accepté par le jury d'examen constitué de :

Rachid Boukhili, président
Étienne MARTIN, membre et directeur de recherche
Oguzhan Tuysuz, membre
Mohsen MOHAMMADI, membre externe

DEDICATION

To the guiding lights of my journey, whose unwavering love and support have shaped my path, and to the city cradled among four mountains, a testament to resilience and inspiration.

ACKNOWLEDGEMENTS

Special thanks to Etienne for his passionate mentorship.

Heartfelt appreciation to my lovely Farnaz for her unwavering support.

And to my parents, for everything.

RÉSUMÉ

L'alliage A20X est un composite à matrice d'aluminium (AMC) haute performance récemment mis au point pour la fusion sur lit de poudre laser (LPBF). Sa grande résistance et sa légèreté en font un excellent candidat pour diverses industries du transport, en particulier l'aviation et l'aérospatiale. Les pièces destinées à ces applications requièrent généralement une combinaison de propriétés, notamment une résistance élevée à la traction, une résistance à la corrosion pour assurer la durabilité et la longévité dans des environnements difficiles, et une résistance à la fatigue pour supporter des cycles de contraintes répétés sans se fissurer ou se briser lors de décollages et d'atterrissages répétés. Cette thèse se concentre sur le développement de nouveaux procédés capables d'optimiser les propriétés de l'alliage A20X fabriqué par LPBF.

Le traitement thermique de mise en solution n'est pas toujours nécessaire pour les alliages d'aluminium LPBF en raison de l'état sursaturé causé par des vitesses de refroidissement élevées. Dans la première partie de ce travail, l'effet du vieillissement direct sur les propriétés mécaniques est étudié. Le vieillissement direct a entraîné un adoucissement significatif du LPBF A20X. Après le vieillissement direct, les précipités existants ont augmenté de taille tout en maintenant une fraction de volume de précipité et une taille de grain constantes. Cela se traduit par une réduction des propriétés mécaniques.

Dans la deuxième partie, le durcissement par précipitation conventionnelle a été étudié. La teneur en argent de l'A20X a facilité la précipitation sur des plans atomiques spécifiques. Un processus de vieillissement en deux étapes - nucléation à basse température suivie d'une croissance à haute température - a permis de réduire l'espacement des précipités et d'améliorer la résistance à la traction, mais au prix d'une moindre résistance à la corrosion due aux réactions galvaniques entre les précipités et la matrice.

Dans la troisième partie de ce travail, l'effet des paramètres de balayage laser des contours sur les défauts proches de la surface, la rugosité de la surface et la performance de fatigue à faible cycle du LPBF A20X a été étudié. La rugosité de la surface a été fortement influencée par l'empilement des bassins de fusion pendant l'impression, qui a été directement affecté par la vitesse de balayage des contours. Par conséquent, la durée de vie en fatigue la plus longue a été obtenue pour les échantillons fabriqués avec une vitesse de balayage des contours et une distance de décalage faibles.

ABSTRACT

The A20X alloy is a high-performance aluminum matrix composite (AMC) recently developed for laser powder bed fusion (LPBF). Its high strength and light weight make it an excellent candidate for various transportation industries, particularly aviation and aerospace. Components for these applications typically require a combination of properties, including high tensile strength to withstand significant surface stress and loads, corrosion resistance to ensure durability and longevity in harsh environments, and fatigue resistance to endure repeated stress cycles without cracking or breaking during repeated take-offs and landings. This thesis focuses on developing post-fabrication heat treatment and laser contour strategies to optimize these properties for LPBF A20X.

Solution heat treatment is not always required for LPBF aluminum alloys due to the supersaturated state caused by high cooling rates. In the first part of this work, the effect of direct aging on mechanical properties is investigated. Direct aging resulted in significant softening of LPBF A20X. After direct aging, the existing precipitates grew while maintaining a constant precipitate volume fraction and grain size, thereby reducing mechanical properties. Moreover, the heterogeneous plastic flow phenomenon observed in the as-printed A20X gradually disappeared due to the annihilation of the Mg/Ag walls along the grain boundaries.

In the second part, conventional precipitation hardening was studied. The silver content in A20X facilitated precipitation on specific atomic planes. A double-step aging process—low-temperature nucleation followed by high-temperature growth—reduced precipitate spacing and improved tensile strength, though at the cost of lower corrosion resistance due to galvanic reactions between the precipitates and the matrix.

In the third part, the effect of laser contour scanning parameters on near-surface defects, surface roughness, and low cycle fatigue performance of LPBF A20X was investigated. Surface roughness was significantly influenced by the stacking of melt pools during printing, which was directly affected by contour scan speed. Consequently, the longest fatigue life was achieved in specimens fabricated with low contour scan speed and offset distance.

TABLE OF CONTENTS

DEDICATION III

ACKNOWLEDGEMENTS IV

RÉSUMÉ ……… V

ABSTRACT ……… VI

TABLE OF CONTENTS VII

LIST OF TABLES XI

LIST OF FIGURES XII

LIST OF SYMBOLS AND ABBREVIATIONS XX

CHAPTER 1 INTRODUCTION 1

CHAPTER 2 LITERATURE REVIEW 3

- 2.1 Laser powder bed fusion (LPBF) 3
- 2.2 Aluminum and its alloys 5
  - 2.2.1 Brief history 5
  - 2.2.2 Strengthening mechanism in aluminum alloys 6
  - 2.2.3 Aluminum alloys classification 9
- 2.3 Laser powder bed fusion of aluminum alloys 12
  - 2.3.1 Microstructure of LPBF aluminum alloys 14
- 2.4 New generation of LPBF aluminum alloys 15
- 2.5 LPBF processability of A20X 15
- 2.6 Role of alloying elements present in A20X 16
  - 2.6.1 Copper (Cu) 16
  - 2.6.2 Magnesium (Mg): 17
  - 2.6.3 Addition of silver (Ag) to Al-Cu-Mg alloys 17

2.6.4 Effect of iron (Fe) and silicon (Si) 18

2.6.5 Effect of titanium (Ti) and boron (B) 18

2.7 Strengthening mechanisms of A20X alloy 20

2.8 Microstructure and mechanical properties of A20X alloy 21

2.9 Heat treatment of aluminum alloys 24

2.9.1 Solution treatment 24

2.9.2 Age hardening treatment 28

2.10 Laser contour scanning of LPBF alloys 32

CHAPTER 3 SCIENTIFIC APPROACH 34

3.1 Critical evaluation of literature review 34

3.2 Research objectives 36

CHAPTER 4 ARTICLE 1: DIRECT AGING OF ADDITIVELY MANUFACTURED A20X ALUMINUM ALLOY 38

4.1 Abstract 38

4.2 Introduction 38

4.3 Experimental procedure 40

4.3.1 Powder and LPBF process 40

4.3.2 Post-process heat treatment 41

4.3.3 Microstructural characterization 41

4.3.4 Mechanical testing 42

4.4 Results and discussion 42

4.4.1 Microstructure of as-printed A20X 42

4.4.2 Effect of direct aging on the A20X LPBF microstructure 43

4.4.3 Effect of direct aging on plastic flow in LPBF A20X 48

4.4.4 Effect of direct aging on Tensile properties 53

4.5 Conclusions ... 55

CHAPTER 5 ARTICLE 2: EFFECT OF PRECIPITATION HARDENING ON THE MICROSTRUCTURE, MECHANICAL, AND CORROSION PROPERTIES OF ADDITIVELY MANUFACTURED A20X ALUMINUM ALLOY ... 57

5.1 Abstract ... 57

5.2 Introduction ... 57

5.3 Experimental procedure ... 59

5.3.1 Powder and LPBF process ... 59

5.3.2 Post-process heat treatment ... 60

5.3.3 Microstructural characterization ... 61

5.3.4 Mechanical testing ... 62

5.3.5 Corrosion experiments ... 62

5.4 Results and discussion ... 63

5.4.1 As-printed microstructure ... 63

5.4.2 Effect of heat treatment on the micro-hardness of LPBF A20X ... 65

5.4.3 Effect of heat treatment on the microstructure of LPBF A20X ... 66

5.4.4 Effect of heat treatment on stress-strain curves of LPBF A20X ... 71

5.4.5 Effect of heat treatment on the tensile properties of LPBF A20X ... 74

5.4.6 Effect of heat treatment on the corrosion properties of LPBF A20X ... 80

5.5 Conclusions ... 82

CHAPTER 6 ARTICLE 3: EFFECT OF LASER CONTOUR SCAN PARAMETERS ON LOW CYCLE FATIGUE PERFORMANCE OF A20X FABRICATED BY LASER POWDER BED FUSION ... 84

6.1 Abstract ... 84

6.2 Introduction ... 84

6.3 Materials and methods 86

  6.3.1 Feedstock material and sample fabrication 86

  6.3.2 Microstructure and surface characterization 89

  6.3.3 Fatigue testing and fractography 89

6.4 Results and discussion 91

  6.4.1 As-built microstructure analysis 91

  6.4.2 As-built surface roughness analysis 96

  6.4.3 Effect of laser contour parameters on LCF 100

  6.4.4 Fracture analysis 102

6.5 Conclusions 105

CHAPTER 7 CONCLUSION AND SUGGESTION FOR FUTURE WORK 107

7.1 Optimizing Strength and Fatigue of A20X Alloy 107

7.2 Conclusions 108

7.3 Limitations and suggestions for future work: 111

REFERENCES 114

LIST OF TABLES

Table 2.1 Chemical composition of A20X (wt.%) [45]. 16

Table 2.2 Measured grain size, yield stress (YS), ultimate tensile strength (UTS), and percentage of elongation (El%) of the studied materials [56]. 23

Table 2.3 Crystal structures of different intermetallics observed in the Al-Cu-Mg-Ag system. .. 31

Table 4.1 Nominal chemical composition of the A20X powder (wt. %) 40

Table 5.1. LPBF A20X chemical composition measured with ICP-OES and LECO analysis (wt. %). 60

Table 5.2. Corrosion parameters acquired from polarization curves. 81

Table 6.1. Contour scanning parameters used in the fabrication of fatigue specimens. Two passes were applied to the S5 condition and only one for the other conditions. 88

LIST OF FIGURES

Figure 2-1 Two views of 3D-printed heat exchangers: cross-section (left) and top view (right) [2]. 3

Figure 2-2 Cost per unit of production for additive and conventional manufacturing methods (a) based on part complexity, and (b) based on production volume [3]........ 4

Figure 2-3 Schematic of LPBF machine (Adapted from [3]). 5

Figure 2-4 Schematic of solid solution hardening mechanism: (a) thwarting movement of dislocations (b) interstitial and substitutional solid solution. 7

Figure 2-5 (a) Schematic phase diagram demonstrating the precipitation hardening mechanism, (b) alloy microstructure at different steps of precipitation hardening [18]........ 8

Figure 2-6 Heating curve of T6 heat treatment including solutioning and aging treatment [19] . . 9

Figure 2-7 Microstructure of AA6061 specimens fabricated on the unheated powder bed. Fig. 4 (a) and (b) perpendicular to build direction. (c) and (d) build direction. Cracks, porosity, melt-pool, and melt-track banding are evident in the microstructure (Adapted from [21])........ 13

Figure 2-8 Relative density of the as-built unmodified AA6061 fabricated using LPBF with variable laser power and scan speed. (Adapted from [21]). 13

Figure 2-9 SEM images showing the clear distinction between the microstructure of AlSi10Mg developed by (a) cast and (b) LPBF (Adapted from [24])........ 14

Figure 2-10 Effect of energy density on porosity content of LPBF A20X........ 16

Figure 2-11 Bright field TEM image of Al-4Cu-0.3Mg-0.4Ag solutionized at 525°C, WQ and aged at 250 °C for 10h.The beam is parallel to <110> [46]........ 18

Figure 2-12 SEM micrographs showing: (a) matrix alloy showing dendritic structure; (b) alloy containing 0.2% solute titanium showing finer cells; (c) alloy containing 0.2% solute titanium and 4.5% TiB2 showing considerable decrease in grain size compared to the matrix alloy [48]. 20

Figure 2-13 . EBSD-IPF maps of A20X printed using different laser energy densities; (a) 92.5 J/mm^3, (b) 52.9 J/mm^3 , (c) 82.9 J/mm^3, (d) 64.9 J/mm^3 , and (e) 41.4 J/mm^3 [36].. 20

Figure 2-14 Engineering tensile flow curves of the studied cast and LPBF A205 in as-received and T7 conditions (Adapted from [56]). 22

Figure 2-15 SEM micrographs of the starting microstructures of the LPBF and cast materials; (a,b) LPBF A205 (c,d) cast A205 (Adapted from [57]). 22

Figure 2-16 Phase diagram of the Al-Cu binary system showing the temperature range for different heat treatments for the alloys (a) with 4.5 wt.% Cu and (b) with 5.65 wt.% Cu [14]. 25

Figure 2-17 Effect solution treatment temperature and duration on tensile strengths of Al-Si-Mg alloy [60]. 26

Figure 2-18 SEM microstructure of laser printed AlSi10Mg samples heat treated in different conditions: (a) 450 °C for 2h; (b) 500 °C for 2h; (c) 550 °C for 2h [61]. 26

Figure 2-19 Si particle size (right axis) and particle distribution (left axis) as a function of solution heat treatment in laser printed AlSi10Mg (Adapted from [59]). 27

Figure 2-20. Effect of solution treatment temperature on (a) tensile flow behavior, (b) tensile properties [59]. 27

Figure 2-21 SEM microstructure of Aluminum A205: (a) as-cast microstructure showing Al_2Cu at grain boundaries(1000X); (b) Microstructure of solution treated A205 showing agglomeration of TiB_2 particles at grain boundaries (1000 X); (c) SEM micrograph showing the colonies of TiB_2 at grain boundaries [15]. 28

Figure 2-22:Evolution of Al-4%Cu strength during aging at 150 °C [14]. 30

Figure 2-23 Hardness evolution of LPBF-A7068 alloy as function of aging temperature (135, 150,165, and 180°C) [68]. 32

Figure 2-24 Effect of laser contour scan parameters on surface deep valley and average roughness of LPBF Inconel 718 [71]. 33

Figure 2-25 Effect of laser contour power and speed on fatigue performance of Inconel 718 [71]. 33

Figure 4-1 Schematic illustration of the LPBF-built parts. (b) Geometry and dimensions of the tensile specimens used in this study. All dimensions are in mm. The build direction (BD) and radial direction (RD) of tensile bars are presented here. 41

Figure 4-2 Microscopic characterization carried out on as-printed A20X in the plane parallel to the build direction. (a) Fine cellular structure, precipitates (θ), and TiB_2 particles observed in SEM micrograph, (b) EBSD IPF map depicting grain orientations with respect to the build direction. The build direction (BD) and radial direction (RD) correspond to the specimen axis in Figure 4-1. 43

Figure 4-3 Micro-hardness variations with aging temperature and time for the LPBF fabricated A20X alloy. The hardness range of as-printed A20X is distinguished using two black lines (considering the standard deviation). SEM micrographs of direct-aged A20X after 12 and 30 hours of heat treatment for different temperatures are shown. The grain sizes are shown in the top-right corners of the SEM micrographs. Red arrows highlight disruption of grain boundary precipitates during direct aging.................................. 44

Figure 4-4 Average precipitate (θ) size and volume fraction as functions of temperature and duration of aging treatment in LPBF-A20X. 46

Figure 4-5. TEM-EDS map showing the distribution of precipitate forming elements in (a) as-printed, and (b) direct aged at 220 °C for 30 hrs A20X... 47

Figure 4-6 TEM bright field images and corresponding SAED patterns: (a,b) as-built and (c,d) aged at 220 °C for 30h. Reflections from the Al matrix and Al_2Cu precipitate are indexed in yellow and green, respectively. ZA denotes the zone axis. SAED patterns were acquired from regions highlighted by red dashed circles................................. 48

Figure 4-7 Comparison between tensile properties of A20X in (a) as-printed and direct aged at 200 °C, (b) 180 °C and 220 °C (as-printed tensile graph is shown in both graphs for comparison purposes). 49

Figure 4-8 Stress decrements as a function of onset strain for each serration during plastic deformation in specimens with highest degree of dynamic strain aging (DSA) observed in this study. As-printed and aged at 200 C for 1 hr ([200,1]) specimens are shown using black and red curves, respectively. 51

Figure 4-9 Dislocation density measured by X-ray diffraction for LPBF-printed A20X direct-aged at various temperatures and durations. 52

Figure 4-10 TEM-EDS map showing agglomeration of alloying elements around TiB_2 particles in specimen direct aged at 220 °C for 30 hrs. The yellow arrow indicates a solute (Cu, Mg, and Ag) cluster. 53

Figure 4-11 Effect of direct aging on mechanical properties of LPBF A20X including : (a) yield stress, (b) ultimate tensile strength (UTS), and (c) elongation at failure. 54

Figure 4-12 SEM images from fracture surface of A20X alloy upon tensile testing: (a) as-built; (b) direct-aged at 200 °C for 1 hr; (c) direct-aged at 200 °C for 30 hrs. 55

Figure 5-1 (a) Schematic illustration of the LPBF-built parts. (b) Geometry and dimensions of the tensile specimens used in this study. All dimensions are in mm. The build direction (BD) and radial direction (RD) of tensile bars are presented here. 60

Figure 5-2. Microscopic characterization depicting the microstructure of as-printed A20X in a plane parallel to build direction: (a) SEM micrograph showing the equiaxed microstructure with Al_2Cu precipitates and TiB_2 particles, (b) EBSD-IPF map showing the random orientation of the grains with respect to build direction. 63

Figure 5-3. TEM-EDS map of the as-printed A20X showing a Cu-rich precipitate network along grain boundaries and segregation of Ag and Mg. 64

Figure 5-4. TEM analysis showing the precipitate type and habitat planes in as-printed A20X. (a) TEM bright field image showing intra-cellular and grain boundary precipitates, (b) selected area electron diffraction pattern from [001] and [011] zone axes showing the presence of stable θ and absence of meta-stable precipitates such as θ'. 65

Figure 5-5. Aging curves show microhardness evolutions during the aging treatment as a function of temperature and duration of LPBF A20X. (a) Aging curves of single-aging treatment performed at three different temperatures including 150 °C,175 °C, and 200 °C, (b) Aging curve of double aging treatment including a pre-aging step (4 hr at 165 °C) followed by aging treatment at 185 °C for different durations. 66

Figure 5-6. EBSD-IPF maps show the grain orientation (with respect to build direction) and size in different heat treatment states. (a) solution-treated (2 hr at 520 °C + water quench),

(b) under-aged condition (aged at 175 °C for 4 hr), (c) peak-aged condition (aged at 175 °C for 24 hr), (d) over-aged condition (aged at 175 °C for 48 hr), (e) double-aged condition (165 °C for 4 hr + 185 °C for 12 hr). 67

Figure 5-7. SEM back-scattered electron (BSE) micrographs showing the microstructure of LPBF A20X in different heat treatment states. (a) solution-treated (2 hr at 520 °C + water quench), (b) under-aged condition (aged at 175 °C for 4 hr), (c) peak-aged condition (aged at 175 °C for 24 hr), (d) single-aged condition (aged at 175 °C for 48 hr), (e) double-aged condition (165 °C for 4 hr + 185 °C for 12 hr). 68

Figure 5-8. Bright-field TEM images along with their respective SAED patterns for LPBF A20X at different stages of age hardening treatment. (a) under-aged condition (aged at 175 °C for 4 hr), (c) peak-aged condition (aged at 175 °C for 24 hr), (d) single-aged condition (aged at 175 °C for 48 hr), (e) double-aged condition (165 °C for 4 hr + 185 °C for 12 hr). Yellow, red, and green indexes show the aluminum matrix, θ', and θ precipitates. 69

Figure 5-9. TEM-EDS map showing elemental distribution in different precipitates observed in age-hardened A20X. (a) Ω precipitates along the $\{111\}_\alpha$ planes, (b) θ'precipitates along the $\{200\}_\alpha$ planes... 71

Figure 5-10. Effect of heat treatment on tensile flow of A20X at: (a) room temperature (25 °C), (b) high temperature (150 °C).. 73

Figure 5-11. Work hardening rate as a function of true strain for as-printed, solutionized, and DA185-12 conditions tested at : (a) 25 °C, (b) 150°C... 74

Figure 5-12. Effect of heat treatment on room and high-temperature tensile properties of LPBF A20X. (a) yield strength (YS), (b) ultimate tensile strength (UTS), (c) elongation at failure. 75

Figure 5-13. Room temperature yield strength of specimens aged at 175°C and double-aged specimens as a function of interparticle spacing (blue curve) and grain size (red curve). 76

Figure 5-14. SEM micrographs showing fracture morphology in tested specimens: (a) Single-aged (A175-48) tested at 25 °C, (b) Single-aged (A175-48) tested at 150 °C, (c) double-aged tested at 25 °C, (d) double-aged tested at 150 °C. 78

Figure 5-15. EBSD micrographs acquired from a region beneath the fracture surface of DA185-12 tested at room temperature, (a) kernel average misorientation (KAM) map, (b) phase map showing Al matrix and TiB_2 particles. 78

Figure 5-16. Yield and tensile strength of various aluminum alloys fabricated using LPBF acquired from the literature [20,56,58,178,224,225]. All the presented data are from alloys in the T6 and T7 states. 79

Figure 5-17. Polarization curves showing the effect of heat treatment on corrosion behavior of LPBF-A20X. 80

Figure 5-18. Corrosion morphology of LPBF A20X after polarization test in 3.5% NaCl solution. (a,b) as-printed, (c,d) solution-treated condition, (e,f) A175-24- peak-aged condition, (g,h) A175-48- over-aged condition, and (i,j) DA185-12- over-aged condition. Intra-granular corroded regions are highlighted with yellow arrows. 82

Figure 6-1. A20X powder (a) chemical composition in wt.%, and (b) particle size distribution used to fabricate fatigue specimens. 87

Figure 6-2. (a) A 3D view of the printed fatigue specimens attached to the build plate in a vertical (build direction) orientation. The specimens were surrounded by protective cases printed simultaneously. (b) The LCF specimen dimensions (mm) used in this study. The build direction (BD) and the LCF sample radial direction (RD) are shown here. 87

Figure 6-3. Representative LCF (a) stress-strain curves at different cycles, and (b) maximum, minimum stress evolution during the test taken from condition S1 (850 mm/s, 50 μm). 90

Figure 6-4. Microscopic characterization performed in the bulk region of as-printed A20X along the build direction taken from condition S1 (850 mm/s, 50 μm). (a) SEM micrograph showing fine cellular structure and the presence of intermetallic phases and TiB_2 particles, (b) IPF map showing grain orientations with respect to the build direction, and (c) EBSD {001}, {110}, and {111} pole figures of as-printed A20X. The build direction (BD) and radial direction (RD) correspond to the specimen axis shown in Fig. 2 (b). 92

Figure 6-5. SEM micrographs of the contour region microstructure in specimens built with different laser parameters: (a) S1 (850 mm/s, 50 µm), (b) S4 (350 mm/s, 50 µm), and (c) S7 (850 mm/s, 100 µm). The average grain size is shown in the top right corner of each image. 93

Figure 6-6. Optical micrographs from gauge cross-section of the as-built LCF specimens. The contour condition for each condition ID is presented in Table 6.1. These images were taken prior to LCF testing. 94

Figure 6-7. SEM micrograph showing the two types of pores observed below the surface of specimens processed with different laser contour parameters. (a) Low magnification, and (b) high magnification back-scattered images showing keyhole porosities generated by low laser contour scanning speed (350 mm/s) in S4 condition. The melt pool boundary is highlighted using a dashed line, and keyhole pores using yellow arrows. (c) Low magnification and (d) high magnification secondary electron images showing lack of fusion voids containing non-melted particles in S7 condition built using a large laser contour offset (100 µm) and high contour scan speed (850 mm/s). 95

Figure 6-8. Surface roughness parameters for the as-built A20X specimens are shown as functions of (a, b) laser contour scan speed and (c, d) offset distance. Conditions grouped in (a) and (b) have the same contour offset distance (50 µm) but different scan speeds. Conditions grouped in (c) and (d) have the same contour scan speed (850 mm/s) but different offset distances. 97

Figure 6-9. Schematic representation of the effect of laser scan speed on surface roughness. (a) Deep valleys are created when melt pools are small due to high laser scan speed. (b) Shallow valleys are created when melt pools are large and deep due to low laser scan speed. SEM image comparing the surface roughness created by (c) high (S1 (850 mm/s)) and (d) low (S4 (350 mm/s)) laser scan speed. 98

Figure 6-10. Optical 3D micrographs showing the surface roughness of as-printed specimens with different laser contour scan speeds and offset distances: (a) S1, (b) S2, (c) S3, (d) S4, (e) S6, and (f) S7. In (g), the condition S5 with double contour scan strategy is shown. Details for all conditions are listed in Table 1. White arrows highlight the surface connected particles. 100

Figure 6-11. Fatigue lifetime of A20X alloy as a function of (a) contour parameters and (b) arithmetic surface roughness (R_a) and depth of deepest valley on the surface with respect to median line (R_v). 102

Figure 6-12. Typical surface image of LCF tested specimen (S1 condition). (a) SEM surface image showing secondary crack formation (yellow arrows) along melt pool boundaries (yellow dashed line). (b) Side view of a valley formed along a melt boundary. (c) Side view of a lack of fusion region observed at the surface of the specimens. 103

Figure 6-13. Fracture surface showing valley crack initiations in (a) sample S2 (600 mm/s, 50 μm), (b) sample S3 (475 mm/s, 50 μm) and (c) sample S4 (350 mm/s, 50 μm). The red dashed lines highlight surface valleys causing crack initiation. Yellow arrows indicate subsurface keyhole pores. 104

Figure 6-14. Fracture surface of samples showing cracks initiating at surface valleys connected to lack of fusion pores in (a) Condition S1 (850 mm/s, 100 μm), (b) S5 condition with double contour scanning (850 mm/s, 50 μm), (c) S6 condition (850 mm/s, 100 μm) and (d) S7 condition (850 mm/s, 100 μm). The red arrows indicate lack of fusion pores. 104

LIST OF SYMBOLS AND ABBREVIATIONS

AM	Additive manufacturing
α	Alpha phase (Aluminum)
AMC	Aluminum matrix composite
Ra	Arithmetic mean roughness
BD	Build direction
N_f	Cycles to failure
CE	Counter electrode
DA	Double-aging
DSA	Dynamic strain aging
EBSD	Electron back-scattered diffraction
EDS	Energy dispersive spectrometer
FCC	Face-centered-cubic
GPZ	Guinier–Preston zone
GS	Grain size
IPF	Inverse-pole figure
LAGB	Low angle grain boundaries
LCF	Low cycle fatigue
LPBF	Laser powder bed fusion
R_v	Maximum valley depth roughness
R_z	Maximum height roughness
MMC	Metal matrix composite
OCP	Open circuit potential
PLC	Portevin-Le Chatelier

RD	Radial direction
R_q	Root mean square average roughness
θ	Theta precipitate
θ'	Theta-prime precipitate
θ''	Theta-double-prime precipitate
R_t	Total height roughness
Ω	Omega precipitate
SAED	Selected area electron diffraction
SCE	Standard calomel electrode
SEM	Scanning electron microscope
SHT	Solution heat treatment
SSS	Super-saturated solid solution
TEM	Transmission electron microscope
UTS	Ultimate tensile strength
YS	Yield strength
XRD	X-ray diffraction

CHAPTER 1 INTRODUCTION

The environmental changes over the last decades have raised concerns regarding the sustainability of aviation industry. Lowering fuel consumption of aircraft not only mitigates the environmental footprint of airplanes but also promises substantial economic benefits. Therefore, reducing fuel consumption and developing lighter aircraft have become paramount imperatives in the modern era of aviation. Modifying and upgrading the aero-engines to increase their fuel consumption efficiency has proven to be a potent solution. Moreover, weight reduction (through the utilization of lightweight components with complex geometries) and mechanical performance improvement are of special interest.

Fabrication of complex aircraft components using conventional manufacturing techniques such as machining and casting is highly expensive. Additive manufacturing (AM) has proven its versatility in fabricating components with complex geometries using a layer-by-layer approach. The fast-paced development of additive manufacturing techniques, such as laser powder bed fusion (LPBF), capable of processing materials, has fostered optimism in the aerospace industry. The application of additive manufacturing techniques allows the fabrication of near-net-shape components at lower costs compared to conventional methods. Moreover, several high-performance lightweight alloys have been developed exclusively to be used with additive manufacturing techniques eliminating the limitations with AM processing of legacy alloys.

Aluminum and its alloys have long been excellent candidates for structural components that require a high strength-to-weight ratio. Additionally, their high thermal conductivity makes them suitable for applications such as heat exchangers and casings. However, fabricating conventional work-hardenable aluminum alloys using laser powder bed fusion (LPBF) presents several challenges, including solidification cracking, directional microstructure, and anisotropic properties. A20X, a high-performance aluminum alloy specifically developed for LPBF, addresses many of these issues. As a metal matrix composite (MMC) containing ceramic particles (TiB_2), it enables the production of crack-free parts with a fine, equiaxed grain structure and random texture. This makes A20X an excellent candidate for large aircraft components, such as bearing housings, frames, exhaust cases, combustor liners, heat exchangers, and stationary flow path components. These parts demand high tensile strength, fatigue resistance, and corrosion resistance. Since A20X is a newly developed alloy, further enhancements to its properties are necessary to improve aircraft performance and reduce weight.

This study evaluates two approaches for maximizing the mechanical performance of LPBF A20X: precipitation hardening and laser contour scanning. The first objective investigates the effect of direct aging at various temperatures and durations on the microstructure and mechanical properties of LPBF A20X. The second objective examines the impact of conventional aging on the alloy's microstructure, corrosion resistance, and mechanical properties. Lastly, the study explores the effect of laser contour scanning on surface roughness and low-cycle fatigue performance. This provides a practical solution for reducing surface roughness in complex AM parts, especially when traditional finishing techniques such as vibratory finishing or shot peening are not feasible.

This thesis contains seven chapters as follows: In Chapter 2 a review of the existing literature on processing and post-fabrication of LPBF aluminum alloys is provided. In Chapter 3 the missing links in the literature are identified to define the objectives of the thesis accordingly. In Chapters 4-6, original research papers addressing the objectives defined in Chapter 3 are presented. Chapter 7 summarizes the key findings of this study along with suggestion for the future work.

CHAPTER 2 LITERATURE REVIEW

2.1 Laser powder bed fusion (LPBF)

Additive manufacturing (AM) or three-dimensional (3D) printing is a cutting-edge technology for the production of geometrically complex components that are challenging to manufacture using conventional methods such as casting, machining, or welding. The AM technique enables rapid construction of customized near-net-shape parts suitable for industrial applications, as shown in Figure 2-1 Moreover, AM offers enhanced design flexibility, optimized part functionality, and reduced design-to-manufacture time, eliminating the need for custom tooling and operator presence during the process [1].

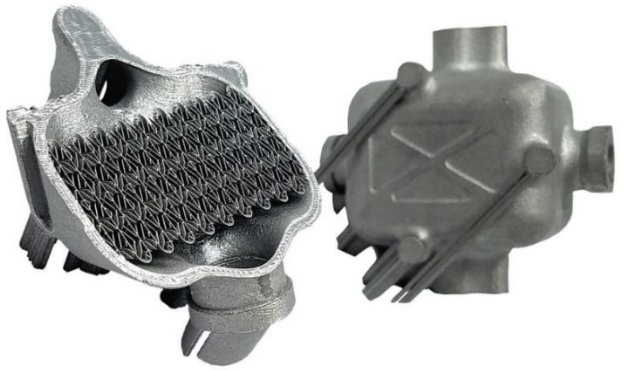

Figure 2-1 Two views of 3D-printed heat exchangers: cross-section (left) and top view (right) [2].

The final part cost is affected by the degree of complexity and the production volume, as shown in Figure 2-2. Additive manufacturing is preferred over conventional manufacturing processes for the construction of complex parts, as shown in Figure 2-2 (a). Conversely, conventional manufacturing is more beneficial than AM for large production volumes, as shown in Figure 2-2 (b). The overall cost to manufacture an AM part is significantly high in batch production due to process complexities. The high costs of machines, material preparation, qualification, and post-processing adversely affect high-volume production using AM. Moreover, due to size limitations, AM techniques are not capable of manufacturing large parts. Therefore, conventional manufacturing methods are preferred for the mass production of larger parts in many industries

[3]. However, in spite of the limitations, AM is generally chosen over conventional processes for the production of customized components at low production volumes.

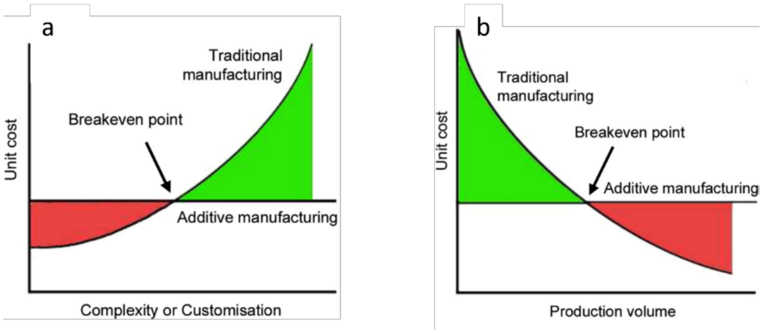

Figure 2-2 Cost per unit of production for additive and conventional manufacturing methods (a) based on part complexity, and (b) based on production volume [3].

Laser powder bed fusion (LPBF) or selective laser melting (SLM) is a well-known metal AM method. Parts are manufactured through the layer-by-layer fusion of metal powder using a laser beam. As shown in Figure 2-3, the laser melts the metal powder layer by layer until the final part is fabricated. Upon completion of each layer, a new layer of metal powder is deposited on the surface using a re-coater to build the next layer. The metal powder accumulated in the bed provides support for the printed part, eliminating the need for support structures during processing [4]. Unlike other AM techniques, LPBF is not limited to a specific group of material and can be optimized to print different materials such as metal, ceramics, and polymers [5].

Several alloys have been developed for AM, and aluminum alloys are no exception. Aluminum alloys such as AlSi10Mg and other Al-Si alloys, A357, and A356 are being widely used with additive manufacturing techniques[6,7]. Processing of aluminum alloys using LPBF introduces multiple challenges during the fabrications. One of the primary challenges during the production of aluminum parts using LPBF technique is the poor flowability of aluminum powder, which significantly affects spreading step [8] . Moreover, due to the high reflectivity and conductivity of the aluminum, high powder lasers are required to fuse aluminum powders [9]. A thin film of aluminum oxide around powder particles reduces the processability of aluminum alloys with LPBF by preventing the remelting of previously printed layers and leaving porosities behind [10,11] .

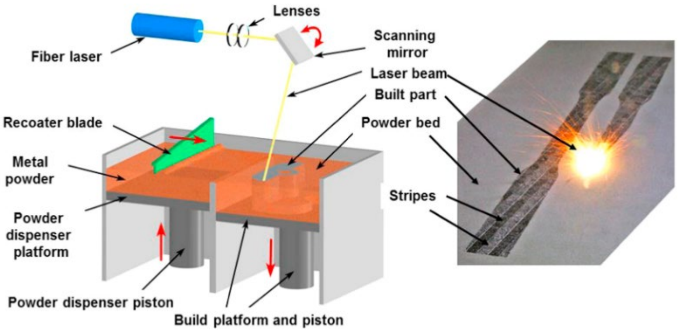

Figure 2-3 Schematic of LPBF machine (Adapted from [3]).

2.2 Aluminum and its alloys

The excellent combination of light weight, strength, and corrosion resistance has made aluminum and its alloys great candidates for different applications, ranging from aerospace and automotive to medical applications. Aluminum alloys can be used to replace many conventional alloys with similar strength but heavier weights. The formation of a surface oxide layer (~ 4 nm) makes aluminum highly resistant against progressive corrosion, which degrades conventional materials like steels. The addition of alloying elements can significantly improve the properties of aluminum. The thermal conductivity of aluminum is around 60% of that of copper, which makes it suitable for heat exchanger applications in industries producing cylinder heads and home appliances [12].

2.2.1 Brief history

It is probably difficult to believe that aluminum was considered as a precious metal like gold and silver several years ago. Aluminum constitutes around 8% of elements found in the earth's crust, which is more than any other element. It can also be found in the form of numerous minerals. Reaction of aluminum and oxygen leads to the formation of highly stable oxides and silicates that conserve aluminum in its pure form. The first pure aluminum piece was obtained by Friedrich Wohler in 1827. Henri Sainte-Claire Deville invented a method to extract aluminum in larger volumes in 1854. In 1865, in the book *From the Earth to the Moon*, Jules Verne eloquently described aluminum as, "**This valuable metal possesses the whiteness of silver, the indestructibility of gold, the tenacity of iron, the fusibility of copper, the lightness of glass. It is easily wrought, it is very widely distributed, forming the basis of most of the rocks, is three times lighter than iron, and seems to have been created with the express purpose of**

furnishing us with the material for our projectile." At the time, the high price of aluminum was a barrier for industrial applications, hence the research to develop a large-scale and economic extraction method began. In 1886, Charles M. Hall in the US and Paul L. T. Héroult in France simultaneously found a method of extraction based on the electrolysis of alumina (Al_2O_3) dissolved in cryolite (Na_3AlF_6). Bauxite ore was the most available type of aluminum mineral used in this process. Karl Josef Bayer began to produce aluminum in industrial scale using the "Hall–Héroult" method. Aluminum turned to the most used non-ferrous metal, and it was used in a variety of applications ranging from construction and transportation to cookware production [13].

2.2.2 Strengthening mechanism in aluminum alloys

Pure aluminum has very low strength, thus, strengthening techniques are necessary to improve the mechanical properties of aluminum. The mechanical properties of aluminum can be improved through the addition of certain alloying elements. Each of these element has a specific effect on the alloy properties, which improves the strength of the alloy through three different mechanisms, including solid solution strengthening, grain boundary strengthening, and precipitation hardening. The strengthening mechanism is defined by the type and amount of alloying elements added to the alloy. New alloys are designed to benefit from all different mechanisms simultaneously.

2.2.2.1 Solid solution strengthening

Addition of certain alloying elements to molten aluminum forms a solid solution with higher strength than pure aluminum. The extent of increase in the strength of the material depends on the solubility and atomic size of the element in aluminum. The solute atoms are randomly distributed in the aluminum lattice, creating a strain field due to the atomic size mismatch between aluminum and the solute atoms. Depending on the size of the atom, the strain can be tensile or compressive. The strain created in the aluminum lattice by these solute atom acts as a barrier to the movement of dislocations, resulting in alloy hardening (see Figure 2-4 (a)) [14,15]. The increased strength of the alloy is proportional to the severity of strain created by the size and concentration of the solute atoms (see Equation 1) [16].

$$\sigma_y \propto \varepsilon_s^{\frac{3}{2}} C^{\frac{1}{2}} \tag{2.1}$$

C is the concentration of solute and ε_s is the lattice strain caused due to atomic size mismatch. Depending on the atomic size difference between the solute and solvent, there can be two different types of solid solutions in metals, as shown in Figure 2-4 (b). When the solute atoms are small enough to fit between the solvent atoms, the interstitial solid solution will form. This can cause volume expansion in the lattice structure due to the smaller size of interstitial atoms. On the other hand, a substitutional solid solution forms when the solute atoms replace some of the solvent atoms in the lattice.

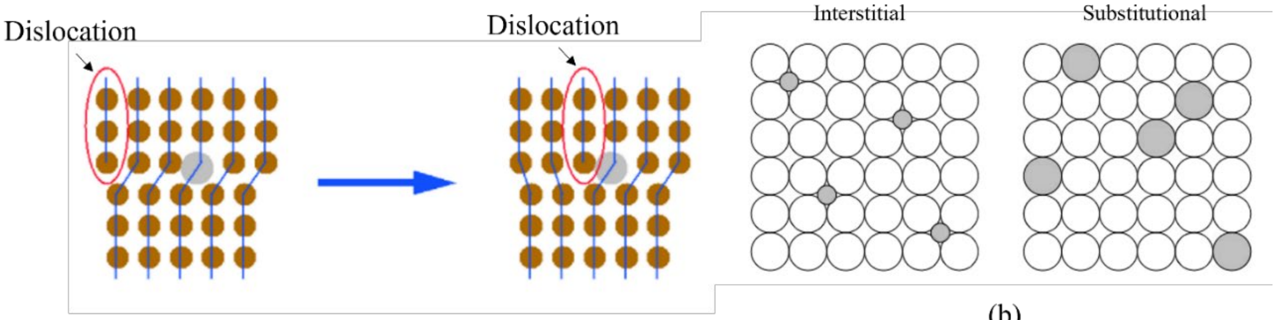

(a) (b)

Figure 2-4 Schematic of solid solution hardening mechanism: (a) thwarting movement of dislocations (b) interstitial and substitutional solid solution.

2.2.2.2 Grain boundary strengthening

During plastic deformation of polycrystalline metals, grain boundaries act as pinning sites against dislocation motion. Therefore, a higher number of grain boundaries means more barriers against dislocation motion, resulting in increases material strength. In 1950, the studies of E.O.Hall and N.J.Petch resulted in the famous Hall-Petch law that relates the yield strength of the material to grain size, as shown in Equation 2.

$$\sigma_y = \sigma_0 + kd^{\frac{1}{2}}, \tag{2.2}$$

where σ_y is the yield stress, σ_0 is the resistance against dislocation movement inside a grain, k is a measure of the local stress required to initiate plastic deformation, and d is the grain size. Grain refinement is the only method of strengthening that improves both strength and toughness. Other strengthening methods increase strength but reduce the toughness and ductility of the material [15,17].

2.2.2.3 Precipitation hardening treatment

Precipitation hardening is the primary strengthening mechanism in A20X and the focus for this research. Figure 2-5 (a) illustrates the phase diagram of a binary alloy. In an alloy containing c_0% of **B**, the solubility of **B** atoms in **A** atoms decreases by lowering the temperature from **T_1** to **T_2**. Conversely, increasing the temperature from **T_2** to **T_1**, increases the solubility of **B** atoms, dissolving all existing **β** phase in the **α** phase. This forms a uniform **α** phase, called solid solution, and the process is called solutioning treatment. After solutioning, if the material is quenched rapidly from **T_1** to room temperature, the atoms will not have enough time to diffuse and form the equilibrium **α+β** structure. Since solubility is significantly lower at the room temperature, the alloy remains in a super-saturated state (see Figure 2-5 (b)). Re-heating the alloy at a certain temperature provides enough driving force for atoms to escape the solid solution state and form small **β** particles called precipitates. The process of re-heating the alloy for precipitation is called the aging treatment. The temperature for this step of heat treatment is much lower than the solutioning treatment and takes hours to complete as the diffusion in solid state is very slow [18].

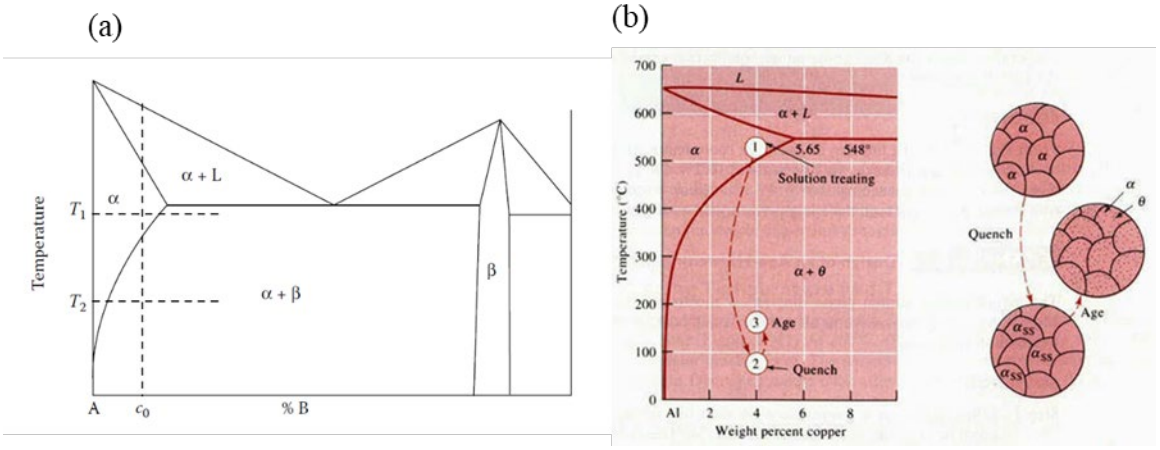

Figure 2-5 (a) Schematic phase diagram demonstrating the precipitation hardening mechanism, (b) alloy microstructure at different steps of precipitation hardening [18].

Figure 2-6 indicates the heating curve of a T6 heat treatment typically used for an alloy manufactured by LPBF. The solution heat treatment is performed at 535 °C for 2 h followed by water quenching to create a super-saturated solid solution. In the next step, the alloy is artificially aged at 158 °C for 10 h .The heating rate is kept at 10 °C/min to avoid incipient melting during the solution treatment [19].

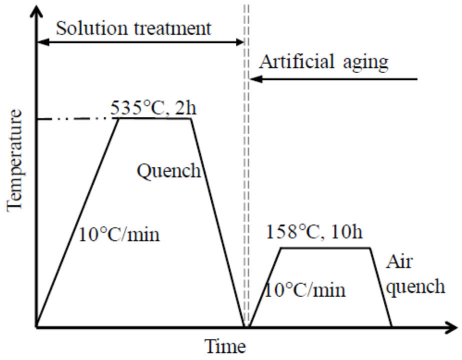

Figure 2-6 Heating curve of T6 heat treatment including solutioning and aging treatment [19] .

2.2.3 Aluminum alloys classification

Aluminum alloys are conventionally categorized into wrought and cast alloys. Another division is based on the method of property development. Alloys that respond favorably to precipitation hardening are considered heat-treatable alloys, while alloys that obtain their properties through mechanical deformation and annealing treatments are considered as wrought alloys. The most widely used classification system is based on the principal alloying element in the alloy. In this system, wrought alloys are shown with a four-digit number and cast alloys are presented with a three-digit number [12].

2.2.3.1 1xxx & 1xx.x Aluminum

This family of alloys includes pure aluminum (purity > 99%), mostly used for electrical and chemical applications. The alloys are resistant against corrosion and benefit from excellent thermal and electrical conductivities. However, due to the absence of alloying elements, the mechanical properties of these alloys are low, which can be improved slightly improved through strain hardening [12,14].

2.2.3.2 2xxx & 2xx.x Aluminum

The main alloying element in this family of aluminum alloys is copper (Cu), with magnesium (Mg) also added as a secondary alloying element. This family of alloys can be solution-treated to achieve a higher level of mechanical properties. Casting alloys in this group, such as A201, A202, A204, and A206, are amongst the strongest casting aluminum alloys. Aging treatment is also used in some cases to further improve mechanical properties. The corrosion resistance of these alloys is not as excellent as other aluminum alloys, and some alloys of this family are prone to intergranular corrosion. The 2xxx family is extensively used in applications requiring high strength/weight ratio, such as automotive, aerospace, and structural parts. Certain alloys of this family can maintain their mechanical properties at elevated temperatures. These alloys require heat treatment to reach optimal strength and ductility. A20X belongs to this family of alloys since its main alloying elements are copper and magnesium [14].

2.2.3.3 3xxx & 3xx.x Aluminum

Wrought alloys:

Manganese (Mn) is the principal alloying element in 3xxx wrought alloys that are categorized as non-heat-treatable alloys. Only a limited amount of manganese can be added to these alloys, which increases their strength by about 20% more than 1xxx alloys. A3003 is the most famous alloy in this family, used for applications requiring good workability [12].

Cast alloys:

Alloys in this family are the most widely used in the casting industry. They usually contain silicon in addition to magnesium or copper. Common alloys include Al-Si-Mg, Al-Si-Cu, and Al-Si-Cu-Mg alloys. These alloys contain 5-20% silicon (Si), up to 4.5% copper (Cu), and up to 1% magnesium (Mg), which can be varied to meet the strength requirements for automotive applications such as piston material. Two main strengthening mechanisms in these alloys are solid solution strengthening and precipitation hardening. Alloys containing copper and magnesium exhibit good high temperature mechanical properties. The addition of silicon to aluminum alloys decreases the coefficient of thermal expansion, making them great candidates for engine applications like cylinder blocks and pistons [12,14].

2.2.3.4 4xxx & 4xx.x Aluminum

The main alloying element in this category is Si, which can be added up to 12% to the aluminum. The addition of silicon reduces the melting point of aluminum significantly, which results in high flowability of aluminum-silicon alloys. These characteristics make Al-Si alloys great candidates for welding purposes. Most alloys in this family are non-heat treatable; however, the addition of copper or magnesium improves their response to heat treatments. Casting Al-Si alloys exhibit excellent ductility and impact behavior, making them the top choice for applications like bridge railings [12].

2.2.3.5 5xxx & 5xx.x Aluminum

Magnesium (Mg) is the principal alloying element in this series of aluminum alloys. The addition of magnesium to aluminum results in an alloy with relatively high strength and reasonable strain hardening properties. Magnesium can be added to aluminum in higher quantities compared to manganese, making it a more effective strengthening element .

2.2.3.6 6xxx & 6xx.x Aluminum

Magnesium and silicon are the main alloying elements in this family. The amounts of these elements are designed to be sufficient for the formation of magnesium silicide (Mg_2Si) precipitates, putting this alloy in the family of heat-treatable aluminum alloys. Mg-Si aluminum alloys exhibit decent formability and machinability properties, and they respond favorably to T6 heat treatment [12].

2.2.3.7 7xxx & 7xx.x Aluminum

The addition of 1-8% zinc as the principal alloying element, along with small amounts of magnesium, results in a heat-treatable aluminum alloy with a high level of mechanical properties. Adding copper and chromium to these alloys improves their properties. This category of alloys is widely used in the structural part and load-bearing sections of the aircraft. The high strength of Al-Zn alloys results in susceptibility to stress corrosion cracking, which can be compensated through over-aging to balance the strength, ductility, and corrosion resistance of the alloy [14].

2.2.3.8 8xxx & 8xx.x Aluminum

This sub-division of alloys usually contains tin (Sn), along with small amounts of copper and nickel, to impart strength in the cast alloy. Since tin acts as a self-lubricating metal, alloys in this family are usually used in bearing applications to minimize mechanical erosion. In wrought alloys, a wide range of elements are added to improve mechanical properties [12].

Precipitate hardening treatment can be employed to improve the mechanical properties of heat-treatable aluminum (Al) alloys. During this heat treatment, intermetallic dispersoids are distributed in the microstructure, resulting in considerable strengthening of the alloy. Chemical composition of the alloy significantly impacts the precipitation behavior. Precipitation hardening treatments involve two main steps: solution treatment followed by a rapid quench, and aging treatment. Aluminum alloys manufactured by additive manufacturing techniques such as LPBF require a post-processing heat treatment to optimize their mechanical properties. Due to the rapid cooling rates (10^6-10^7 °C/s) inherent in LPBF, the heat treatment of LPBF alloys should be redesigned accordingly to reach the maximum potential strength of the alloy [20].

2.3 Laser powder bed fusion of aluminum alloys

Fabrication of aluminum alloys using traditional techniques involves multiple challenges, such as coarse microstructure due to slow cooling, offset defects, shrinkage, slag inclusion, and elemental segregation that are detrimental to mechanical properties. Moreover, aluminum alloys like the 6xxx series are difficult to produce using wrought techniques due to the presence of hard intermetallics (precipitates) [19]. The laser powder bed fusion technique can be utilized to fabricate complex structures made of aluminum alloys that are challenging to process using conventional methods. The unique combination of aluminum properties and the LPBF process can be used in various applications. Multiple studies have investigated the efficiency of heat exchanger fabricated using laser powder bed fusion, showing significant improvement compared to their conventional counterparts.

Numerous studies have been published over the last few years indicating the adaptation of already existing alloys for the LPBF process. However, alloys that exhibit good fluidity are known to be an excellent match for LPBF. Al-Si-Mg alloys are widely used with laser-based manufacturing techniques [22]. These alloys benefit from a low thermal expansion and a short solidification range, which results in a good fluidity of molten alloy. On the other hand, wrought alloys from 2xxx, 6xxx and 7xxx classified as precipitate hardenable alloys are prone to hot tearing due to their large solidification range and coefficient of thermal expansion [7]. This family of alloys has not been adapted for laser-based manufacturing techniques due to a pretty narrow processing window and susceptibility to hot cracking like AA6061[21,22]. Figure 2-7 indicates the crack formed across the microstructure in LPBF AA6061 due to the large solidification range

[22]. However, by adding certain alloying elements to crack susceptible alloys, they can be improved significantly, but considering the flexibility required for LPBF materials, most of the attention has been focused on crack-free alloys to maximize their mechanical properties.

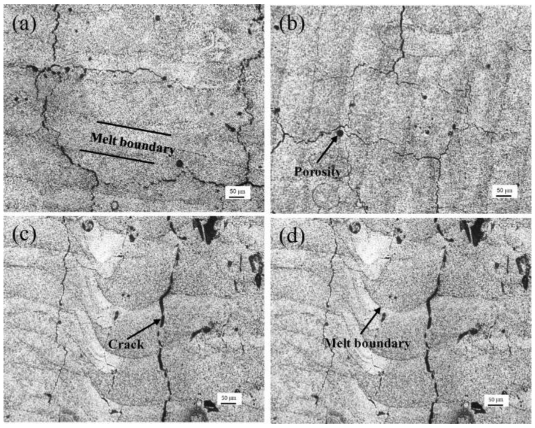

Figure 2-7 Microstructure of AA6061 specimens fabricated on the unheated powder bed. Fig. 4 (a) and (b) perpendicular to build direction. (c) and (d) build direction. Cracks, porosity, melt-pool, and melt-track banding are evident in the microstructure (Adapted from [21]).

Figure 2-8 illustrates the processing window of unmodified LPBF AA6061, indicating its narrow processing window. This results in a maximum relative density of 95% over a wide range of scanning speed. This relative density is almost 4% lower than similar Al-Si-Mg alloys that can attain a density of over 99% [21].

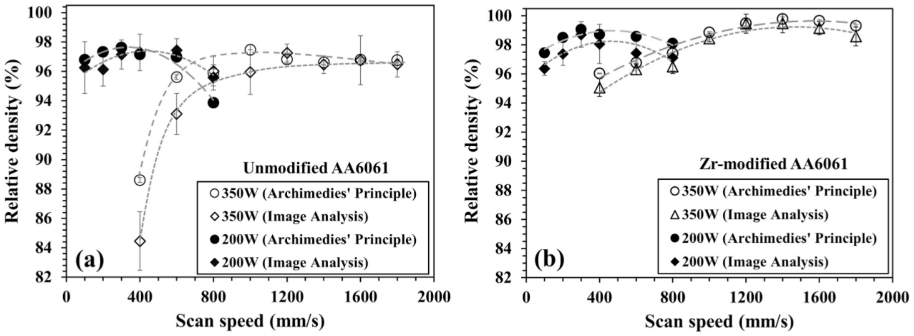

Figure 2-8 Relative density of the as-built unmodified AA6061 fabricated using LPBF with variable laser power and scan speed. (Adapted from [21]).

Aluminum alloys currently being used with LPBF possess mechanical properties lower than heat treatable wrought alloys like AA7075 ,which are not adaptive to the LPBF process due to major cracking issues [8]. Some of these alloys do not respond well to heat treatment compared to conventional alloys. On the other hand, LPBF fabricated parts require stress relief after printing, which significantly softens the alloy [23]. Thus, subsequent precipitation hardening is necessary to recover the high strength before the stress-relieving process. However, the high temperatures involved in solution treatment can alter the refined structure left from laser printing, leading to mechanical properties that are similar to or lower than those of wrought or cast alloys [27]. Thus, optimizing the alloy composition to retain its fine structure during post-fabrication treatments seems to be the most effective method to prevent degradation of mechanical properties. Moreover, some of these alloys do not respond well to heat treatment compared to conventional alloys [20].

2.3.1 Microstructure of LPBF aluminum alloys

Figure 2-9 compares the microstructure of AlSi10Mg fabricated using LPBF and cast methods, showing the highly refined structure in printed structure compared to cast alloy. Fabricating aluminum alloys using LPBF results in a fine microstructure without the addition of any refinement agent. Whereas specific alloying elements are added to obtain a refined microstructure during the casting process of aluminum alloys, promoting nucleation during solidification [24]. Increasing the cooling rate transforms the microstructure from dendritic to equiaxed , which enhances mechanical properties [8].

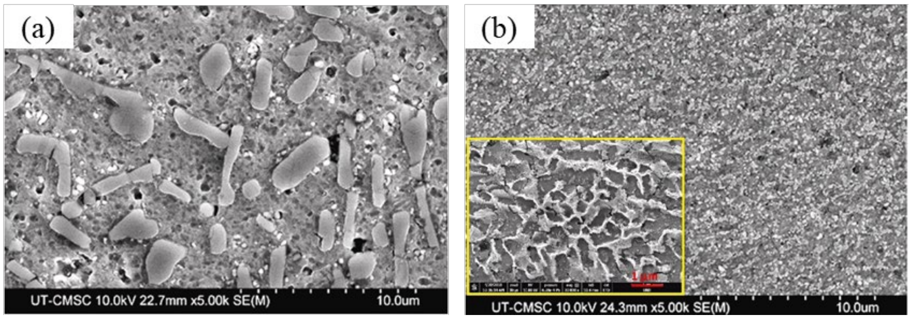

Figure 2-9 SEM images showing the clear distinction between the microstructure of AlSi10Mg developed by (a) cast and (b) LPBF (Adapted from [24])

Moreover, the amount of inclusions such as oxide particles or slag particles observed in LPBF alloys is significantly lower than cast alloys, due to the smaller volume of molten metal and the controlled environment of LPBF [24]. Furthermore, complex alloys fabricated using conventional techniques such as casting and forging are more likely to suffer from elemental segregation.

However, the extremely high cooling rates (10^3-10^7 K/s) during the LPBF process mitigate this issue by suppressing the diffusion of alloying elements [25,26]. Due to the complex thermal profile and high cooling rates, in laser-printed alloys often exhibit heterogenous and non-equilibrium microstructure [27,28]. For instance, Xu et al. [29] and Tucho et al. [30] reported the formation of meta-stable Laves and Niobium (Nb) rich phase in as-printed IN718, which act as sink points for alloying elements [29,30]. Gabrysiak et al.2021 reported the formation of an Al-Mn-Ce rich meta-stable phase in an alloy containing 6% Mn and 2% Ce, which disappears after stress relief heat treatment [31].

2.4 New generation of LPBF aluminum alloys

Due to the increasing demand for high-strength aluminum alloys suitable for LPBF applications, most research is focused on addressing challenges associated with the compatibility of precipitation hardenable alloys with LPBF. Hot cracking of aluminum alloys can be controlled by adding alloying elements that shorten the solidification range or by using nucleation agents to promote the formation of a highly equiaxed structure rather than a columnar one [32]. Inoculants such as Zr, Sc, TiB_2, and LaB_6 are either added to the powders or formed in-situ [33]. Moreover, in-situ alloying has proven to be an effective method for creating a highly equiaxed structure to minimize cracking in high-strength aluminum alloys [34]. The addition of ceramic particles to aluminum matrix has proven to be promising in addressing both these challenges regarding the processability of the alloy and improving the mechanical and tribological properties of LPBF alloys.

2.5 LPBF processability of A20X

A20X is the newest member of LPBF heat-treatable metal matrix composites. It is a refined version of conventional aluminum alloys developed for AM to provide design flexibility and optimum mechanical properties. A20X alloy belongs to the 2xxx family that contains copper as the primary alloying element. Copper contributes to the strengthening of the alloy through solid solution and precipitation hardening mechanism (see Table 2.1 for composition). Furthermore, alloying elements like magnesium and silver are added to A20X alloys to modify the precipitation kinetics and promote precipitation on specific atomic planes. A20X is a metal matrix composite that takes advantage of TiB_2 inoculants to improve the LPBF processability. TiB2 has proven to be the most effective reinforcer in aluminum alloys [44]. During solidification process, a thin layer of Al_3Ti will be formed around TiB2 particles, turning it into a highly effective grain nucleant that results in grain refinement and controls hot cracking by migrating to the remaining liquid phase. Moreover, TiB_2 particles do not react with aluminum at extremely high temperatures, which is an advantage for LPBF techniques with high processing temperatures [35].

Table 2.1 Chemical composition of A20X (wt.%) [45].

Al	Cu	Mg	Ag	Ti	B	Si	Fe	Others
Bal	4.7	0.33	0.76	3.44	1.47	0.04	0.03	0.25 max

Ghasri-Khouzani et al. [36] investigated the effect of laser scan parameters and layer thickness on the LPBF processability of A20X. The effect of energy density on the porosity content of LPBF-printed parts is presented in Figure 2-10, showing high relative density (≥ 99.5%) for a wide range of laser scan parameters. The wide processing window of LPBF A20X is attributed to the presence of secondary particles and alloying elements promoting heterogeneous nucleation during solidification.

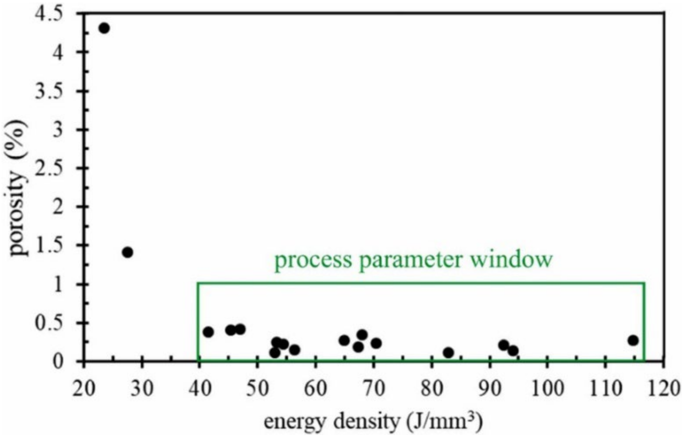

Figure 2-10 Effect of energy density on porosity content of LPBF A20X

2.6 Role of alloying elements present in A20X

2.6.1 Copper (Cu)

Copper improves the strength of aluminum through two different mechanisms including solid solution and precipitation hardening. The difference in atomic sizes of aluminum and the dissolved copper creates a strain field in the alloy lattice, which increases the strength of the alloy by hindering the movement of dislocations. Figure 2-5 indicates the phase diagram of the binary Al-Cu system. For the alloys containing less than 5.7% copper, a homogeneous solid solution of copper and aluminum forms at higher temperatures. At lower temperatures, the solubility of copper in aluminum decreases significantly, leading to the formation of the Al_2Cu phase (θ). Solution and aging treatments facilitate the distribution of Al_2Cu across the aluminum matrix in the form of small dispersoids, which enhances the mechanical properties [37].

2.6.2 Magnesium (Mg):

Addition of magnesium (Mg) in small amounts is beneficial to improve the mechanical properties of aluminum through solid solution strengthening. For instance, the addition of 1% magnesium increases the strength of Al by 30-40 MPa. Addition of Mg to Al-Cu binary alloys increases the peak strength achievable through precipitation hardening. Magnesium changes the precipitation behavior and improves the fatigue properties of the alloy significantly by creating new intermetallic phases, making the Al-Cu-Mg alloy a great candidate for aerospace applications [38]. Formation of the S phase (Al_2CuMg) is similar to the θ phase in the Al-Cu binary system. Precipitation of S phase (Al_2CuMg) includes the nucleation of finely distributed coherent GPZ and GPBZ (Guinier-Preston-Bagariatskij zones) and evolution of meta-stable phases like θ'', θ', and S' that results in the precipitation of non-coherent equilibrium phases (θ & S) [39]. The observation of the S phase is highly dependent on the Cu:Mg ratio of the alloy [40].

2.6.3 Addition of silver (Ag) to Al-Cu-Mg alloys

Inclusion of silver (Ag) improves the response of the Al-Cu-Mg alloys to heat treatment. Silver also improves the stability of mechanical properties at elevated temperatures [41]. In the Al-Cu-Ag system, silver atoms migrate to the interface between the Al matrix and the precipitates thwarting the coarsening of θ' precipitates [42]. The Al-Cu-Mg-Ag alloys such as A201 and A205 are known to have good mechanical properties up to 200 °C compared to other cast alloys [43]. The enhanced properties are due to the formation of Ω precipitates on the $\{111\}$ planes. In face centered cubic (FCC) metals like aluminum, the $\{111\}$ planes are the most active crystal planes during plastic deformation. Strengthening through precipitation on this family of planes improves mechanical properties significantly by prohibiting the movement of dislocations. Thus, the formation of Ω precipitates on the $\{111\}$ plane is known to be more effective than θ' precipitates on the $\{100\}$ planes. Moreover, Ω exhibits better coarsening resistance than θ'[44]. Coexistence of Mg and Ag results in the formation of solute clusters on {111}, inducing the formation of Ω precipitates [45]. Multiple factors affect the formation of Ω precipitates in Al-Cu-Mg-Ag systems. According to Hutchinson et al. [46] precipitation of the S phase depletes the available magnesium atoms in the solid solution. Consequently, few magnesium atoms are available to form Cu-Mg clusters on {111}, which prevents nucleation of the Ω phase . Figure 2-11 illustrates the microstructure of the Al-4 Cu-0.3Mg-0.4Ag solution- and age-treated at 250 °C for 10 hr showing θ', S, and Ω precipitates in the aluminum matrix. According to Forde [47], long aging heat treatments adversely affect the mechanical properties of Al-Cu-Mg-Ag alloys like A201. The author reported considerable decrease of yield strength in A201 samples age-treated at 205 °C for 1000 hr, attributed to Ostwald ripening of Ω precipitates.

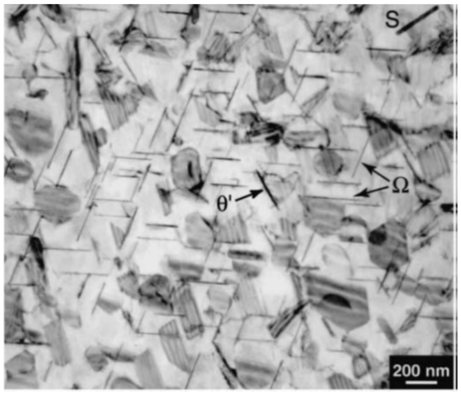

Figure 2-11 Bright field TEM image of Al-4Cu-0.3Mg-0.4Ag solutionized at 525°C, WQ and aged at 250 °C for 10h.The beam is parallel to <110> [46].

2.6.4 Effect of iron (Fe) and silicon (Si)

Iron (Fe) and Si are added in extremely small amounts and are considered as impurities in A20X. In the equilibrium state, Al, Si, and Fe combine to form the $FeSiAl_8$ and $FeSiAl_5$, which appear as long needles [43].

2.6.5 Effect of titanium (Ti) and boron (B)

Addition of pure titanium (Ti) to Al alloys results in a significantly finer microstructure. Titanium induces the formation of peritectic Al_3Ti, an intermetallic particle known to be a great nucleant for aluminum crystals, creating fine microstructure. During solidification, dissolved titanium agglomerates at the solid-liquid interface, hindering the growth of dendrites and resulting in fine equiaxed microstructure [48]. Titanium is also added in combination with boron (B) in metal matrix composites (MMCs). Matrix-reinforcing particles like TiB_2 have attracted the attention of material researchers to produce MMCs, which are versatile ceramic materials for applications requiring high strength-to-weight ratios. These MMCs are added to Al to improve mechanical properties, wear resistance, and solidification behavior to eliminate hot tearing in manufacturing processes associated with high cooling rate process like LPBF. Since the melting temperature of these particles is much higher than that of the alloys during the melting process, they remain solid. As the solidification process begins, the TiB_2 particles can either be distributed evenly across the microstructure or be pushed to regions that solidify last, such as grain boundaries and inter-dendritic regions, depending on the solidification rate. Moreover, due to the excellent coherence between TiB_2 particles and aluminum, these particles act as grain nucleators along their {0001} faces [49,50]. It has also been reported that TiB_2 particles act more as grain refiners than grain nucleators by thwarting grain growth. According to Forde 2015 [47], TiB_2 acts as a grain refiner only in the presence of excessive amount of free Ti, resulting in the formation of peritectic Al_3Ti coating on the surface of TiB_2 , which acts a grain nucleator [51]. Figure 2-12 illustrates the effect of addition of titanium in its free form or as titanium boride particles. By adding 0.2% titanium to aluminum, peritectic Al_3Ti forms, resulting in a significant drop in grain size from 300 to less than 100 μm. Moreover, the addition of titanium-boride particles to the alloy slightly decreases grain size through agglomeration of titanium boride at grain boundaries, hindering grain growth [48]. EBSD-IPF micrographs of LPBF-A20X acquired by Ghasri-Khouzani et al. [36] are shown in Figure 2-13. The grain structure maintained its equiaxed microstructure over a wide range of processing window, with no sign of epitaxial grain growth observed. This was attributed to the presence of free titanium as an alloying element and TiB_2 particles.

According to Du et al. [35], reinforcement particles can affect the precipitation kinetic of intermetallics during aging treatment. Mismatches in thermomechanical properties, such as the coefficient of thermal expansion between the matrix and reinforcing particles, result in plastic deformation and high dislocation density around reinforcing particles. Dislocations act as nucleation sites, promoting the heterogeneous distribution of precipitates, which is detrimental to the mechanical properties of the alloy.

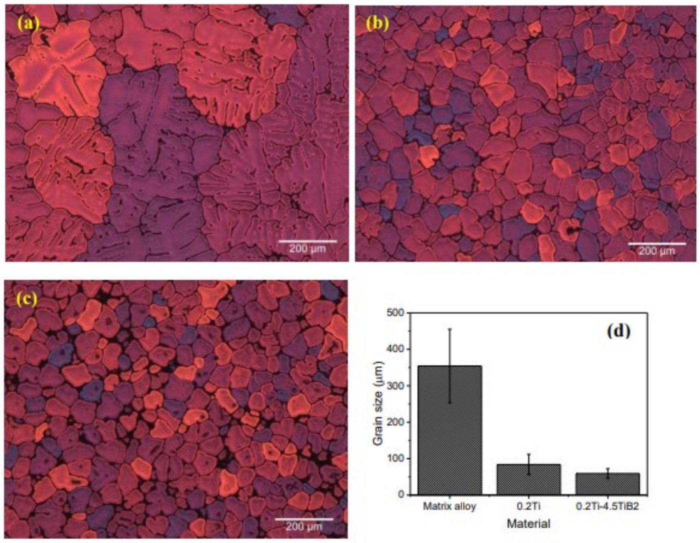

Figure 2-12 SEM micrographs showing: (a) matrix alloy showing dendritic structure; (b) alloy containing 0.2% solute titanium showing finer cells; (c) alloy containing 0.2% solute titanium and 4.5% TiB2 showing considerable decrease in grain size compared to the matrix alloy [48].

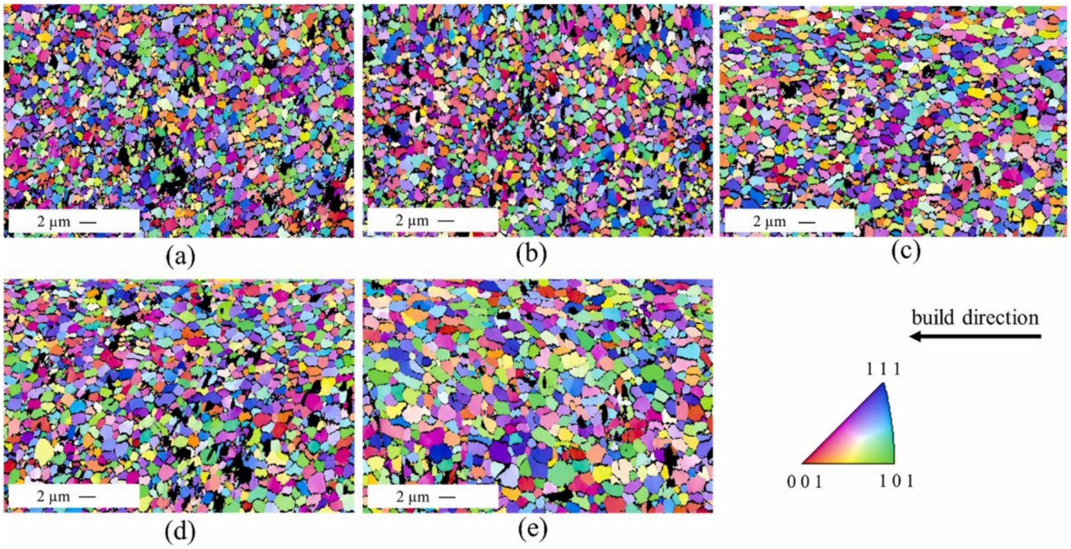

Figure 2-13 . EBSD-IPF maps of A20X printed using different laser energy densities; (a) 92.5 J/mm^3, (b) 52.9 J/mm^3 , (c) 82.9 J/mm^3, (d) 64.9 J/mm^3 , and (e) 41.4 J/mm^3 [36].

2.7 Strengthening mechanisms of A20X alloy

The A20X benefits from a complex precipitation system due to the coexistence of Cu, Mg and Ag. Primary precipitates such as Al_2Cu and Al_2CuMg significantly improve the alloy's mechanical properties. The addition of silver improves the precipitation behavior considerably by stimulating the precipitation of a specific intermetallic phase, Ω, on {111} planes [48]. Precipitation of intermetallic dispersoids within the aluminum matrix enhances the mechanical properties through precipitation hardening treatment and alloy aging. For optimal mechanical properties and stress corrosion cracking resistance, the alloy must be aged until θ' and θ'' precipitates coexist [52,53]. A20X benefits from multiple strengthening mechanisms, including solid solution hardening, precipitation hardening, and grain refinement, which produce high tensile (511 MPa) and yield (440 MPa) strengths in the heat-treated state [54].

2.8 Microstructure and mechanical properties of A20X alloy

Figure 2-14 compares the tensile curves of LPBF and cast A205 in the as-fabricated and heat-treated state. The as-printed A20X exhibits a higher yield and ultimate stress compared to the as-cast A205, which is attributed to the fine equiaxed structure of as-printed A20X that allows it to surpass cast A20X in strength and ductility. The equiaxed structure of A20X facilitates more homogenous distribution of deformation across the microstructure. This is one of the main advantages of A20X over other alloys like AlSi10Mg, which suffer from early crack initiation due to columnar grains and inhomogeneous distribution of plastic deformation [55]. Moreover, LPBF A20X possesses higher ductility compared to cast A20X in the heat-treated state due to the higher fraction of precipitate-free zone in the LPBF structure (finer grain size) compared to the cast structure, as shown in Figure 2-15. Dislocations and vacancies act as the nucleation site for precipitates. Precipitate-free zones are created around grain boundaries due to the low dislocation density in these areas. That results in the formation of a soft phase in the vicinity of grain boundaries, leading to slightly lower strength and higher ductility of the LPBF structure compared to the cast structure in the heat-treated state [56].

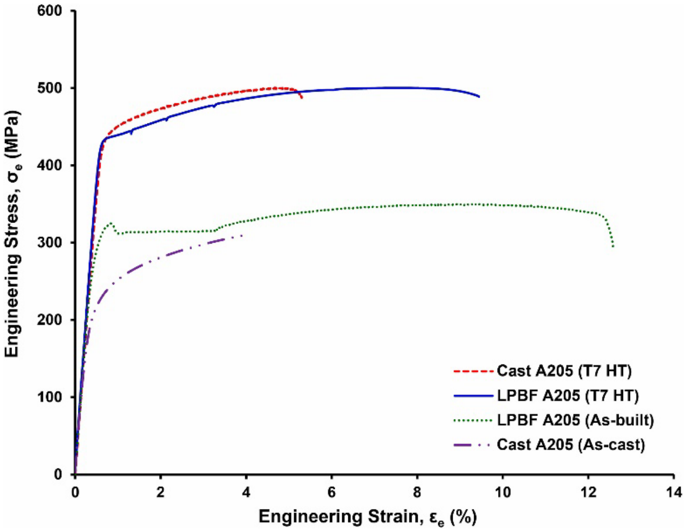

Figure 2-14 Engineering tensile flow curves of the studied cast and LPBF A205 in as-received and T7 conditions (Adapted from [56]).

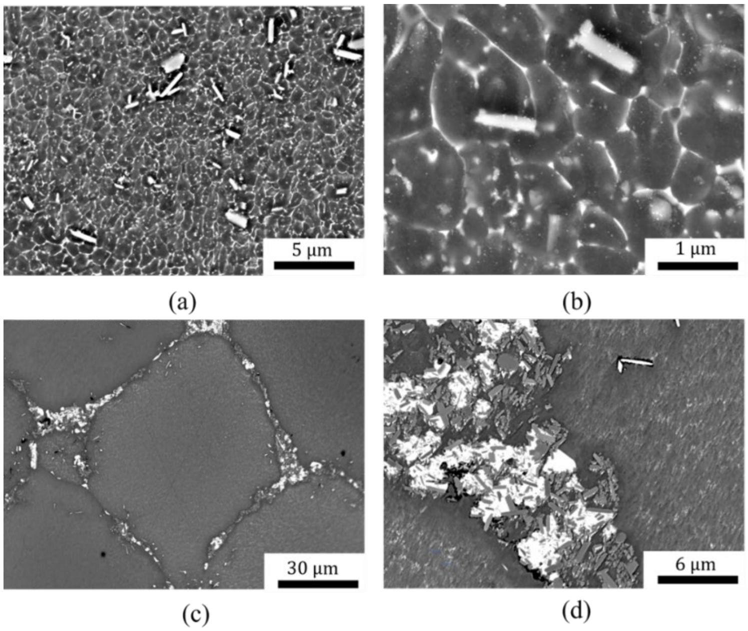

(a) (b) (c) (d)

Figure 2-15 SEM micrographs of the starting microstructures of the LPBF and cast materials; (a,b) LPBF A205 (c,d) cast A205 (Adapted from [57]).

The conventional heat treatment used for cast alloy are not necessarily optimized for LPBF alloys due to different microstructure caused by extreme cooling rates. Therefore, the heat treatment of these alloys needs to be reinvestigated in more detail, considering its significant effect on mechanical properties. Avateffazeli et al. [56] reported that due to the finer structure of LPBF alloys, shorter solution treatments are required [50]. However, most studies on A20X alloy have investigated T7 heat treatment, which involves a long double-step solution treatment that seems unnecessary due to the specific nature of LPBF alloys. Further research on the post-fabrication processing of the alloy is needed to understand its behavior to heat treatments. The importance of meta-stable phases reported in LPBF alloys is also yet to be investigated which could help to reduce the time and energy spent on hardening of A20X. Bridging the knowledge gap between the specific needs of LPBF aluminum alloys and precipitation hardening treatment is the aim of the current work, which can fortify the knowledge base for post-processing treatment of additively fabricated aluminum alloys, specifically A20X due to its significant mechanical properties as the strongest aluminum alloy.

Table 2.2 indicates the effect of heat treatment on tensile properties and grain size of the cast and LPBF A205 studied by Avateffazeli et al [56]. In this study, the authors investigated the effect of traditional T7 treatment on the mechanical properties of A205 fabricated using casting and LPBF. Heat treatment resulted in significant improvement of tensile properties in both cast and LPBF A205. The significant improvement was attributed to the precipitation of coherent and non-coherent precipitates. The LPBF alloy experienced a grain growth of almost 200% from 1.1 to 3.5 microns during T7 heat treatment, while the cast alloy maintained its grain size due to agglomeration of TiB_2 particles at grain boundaries. Considering the high tensile properties of LPBF A20X, it can potentially replace conventional alloys in LPBF applications to provide an improved performance and optimized processability.

Table 2.2 Measured grain size, yield stress (YS), ultimate tensile strength (UTS), and percentage of elongation (El%) of the studied materials [56].

Materials	Grain size (μm)	Yield strength (MPa)	Tensile strength (MPa)	Elongation (%)
Cast A205 (as-cast)	46.4±13.5	215±1.6	295±5.5	4.1±1.5
Cast A205 (T7)	48.5±10.7	441±1.4	501±6.7	5.3±1.6
LPBF A205 (as-printed)	1.1±0.4	309±1.5	350±1.7	12.5±1.1
LPBF A205 (T7)	3.5±1.6	440±1.7	483±2.4	9.5±1.3

Barode et al. [58] investigated the effect of aging treatment with a short solutionizing step (1 hr) on microstructure and mechanical properties of LPBF A20X. The authors also reported the aging curve at 190 °C. Shortening the heat treatment resulted in significant improvement of ductility (45%) and gradual improvement of tensile properties compared to heat treatment with a long solution treatment. The improvement was attributed to the finer grain size and elimination of grain boundary cracks. However, the authors did not report the aging curves at various temperatures or the high-temperature mechanical properties.

2.9 Heat treatment of aluminum alloys

Aluminum heat treatment involves controlled heating and cooling processes to modify its mechanical properties and microstructure. Through techniques like annealing, quenching, and precipitation hardening, the metal's strength, hardness, and other characteristics can be tailored for diverse applications, from aerospace to automotive manufacturing.

2.9.1 Solution treatment

Solution heat treatment is one of the most critical steps of the precipitation hardening process. Its primary objective is to create a homogenous single-phase solid solution (See Figure 2-5). After solution treatment, the alloy is quenched rapidly to freeze the microstructure and form a saturated solution. Having a super-saturated solid solution is imperative for the aging step. A proper solutioning heat treatment requires dwelling at sufficiently high temperatures for enough time to obtain a uniform solid solution. The adequate temperature and time are defined by the composition and initial microstructure of the alloy, and a margin of error should be considered to account for unintentional over-heating, which might lead to incipient melting of phases such as the initial eutectic. Incipient melting leads to the formation of non-ductile phases along the grain boundaries, which could negatively affect the mechanical properties in extreme cases. Figure 2-16 demonstrates the phase diagram of the Al-Cu binary system. For alloy (a), the minimum temperature of solution heat treatment must be above the solvus line in the single-phase region, while the maximum temperature should avoid incipient melting. Alloys with higher copper, like alloy (b) in Figure 2-16, cannot reach the fully solutionized state. The maximum temperature of solution heat treatment is limited by the incipient melting of the eutectic phase [59]. However, due to rapid solidification (10^3-10^7 K/s) in laser-printed alloys, the segregation of alloying elements is eliminated, resulting in a more homogenous structure compared to cast alloys [25,26]. Thus, LPBF alloys are less susceptible to incipient melting created by element segregation. These facts need to be considered in the heat treatment of LPBF aluminum alloys to maximize the effectiveness of heat treatment with any concern regarding incipient melting.

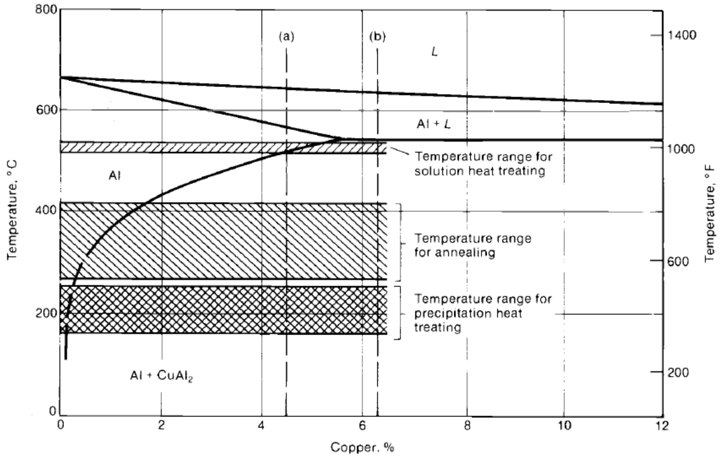

Figure 2-16 Phase diagram of the Al-Cu binary system showing the temperature range for different heat treatments for the alloys (a) with 4.5 wt.% Cu and (b) with 5.65 wt.% Cu [14].

The minimum temperature of solution heat treatment also significantly affects the material's mechanical properties. Figure 2-16 indicates the solvus line of the Al-Cu binary system. If the alloy is not adequately solution treated at a sufficiently high temperature, the solutionizing will not be complete; therefore, less solute will be available in the following steps. As illustrated in Figure 2-17, upon solutionizing at higher temperatures, further precipitates will dissolve in the matrix leading to a higher tensile strength. The higher solute content in the matrix is also beneficial for consequent aging step. Moreover, performing solution treatment at higher temperatures leads to the formation of excess vacancies, which act as nucleation sites for precipitates during the aging. However, excessive temperatures might result in formation of temperatures induced porosities that are known to degrade mechanical properties, the maximum temperature of solution heat treatment should be defined to ensure full dissolution of precipitates, prevent incipient melting and temperature-induced porosities [14].

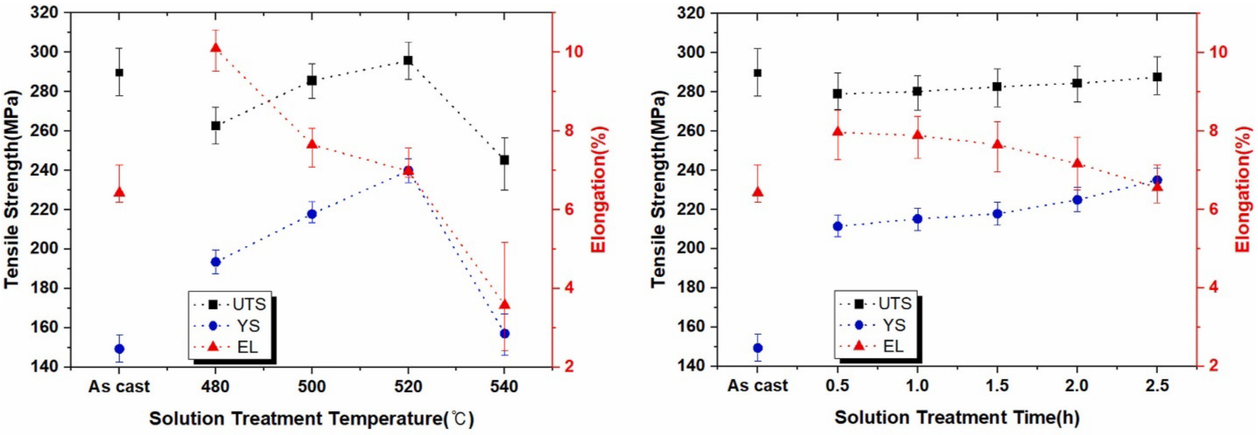

(a) (b)

Figure 2-17 Effect solution treatment temperature and duration on tensile strengths of Al-Si-Mg alloy [60].

Figure 2-18 illustrates the microstructure of LPBF AlSi10Mg solution-treated at different conditions. Increasing the solution treatment temperature from 450 to 550°C allowed the super-saturated Si trapped in the matrix to precipitate and join bigger particles. The increase in the size of Si particles was due to both the coalescence of smaller precipitates and Ostwald ripening [61].

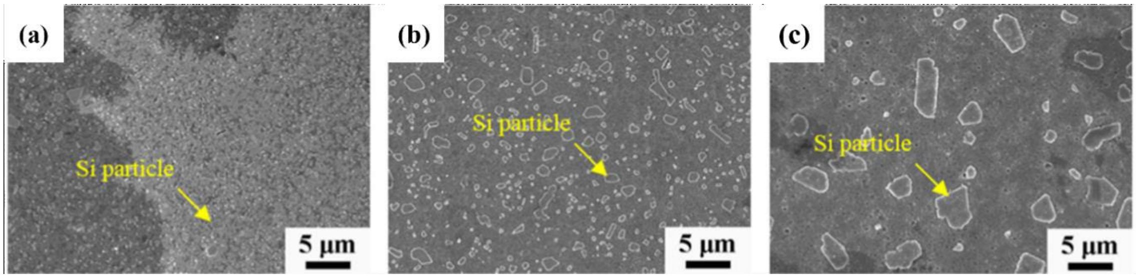

Figure 2-18 SEM microstructure of laser printed AlSi10Mg samples heat treated in different conditions: (a) 450 °C for 2h; (b) 500 °C for 2h; (c) 550 °C for 2h [61].

The quantitative analysis of Si particles in samples solution-treated at different temperatures is presented in Figure 2-19, as conducted by Li et al. [59]. In the as-received sample, the Si particles are very fine and evenly distributed across the microstructure, indicating its effect on mechanical properties, as shown in Figure 2-20. On the other hand, in the solution-treated samples, the average size of Si particles is larger than the as-printed sample (See Figure 2-19). As the solution treatment temperature increased from 450 °C to 550 °C, the average size of Si particles increased from 3 μm to 4.5 μm, leading to a reduction in tensile properties [59].

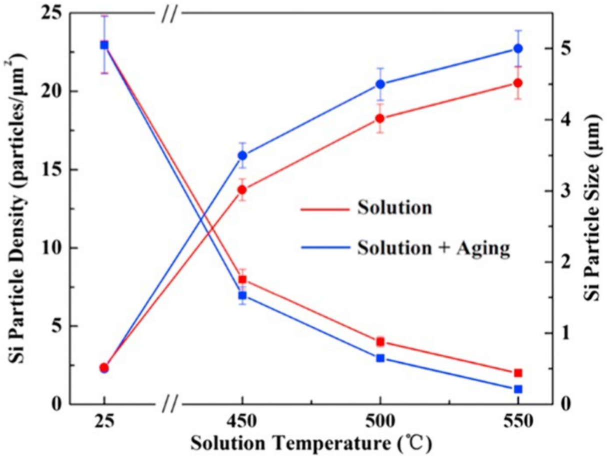

Figure 2-19 Si particle size (right axis) and particle distribution (left axis) as a function of solution heat treatment in laser printed AlSi10Mg (Adapted from [59]).

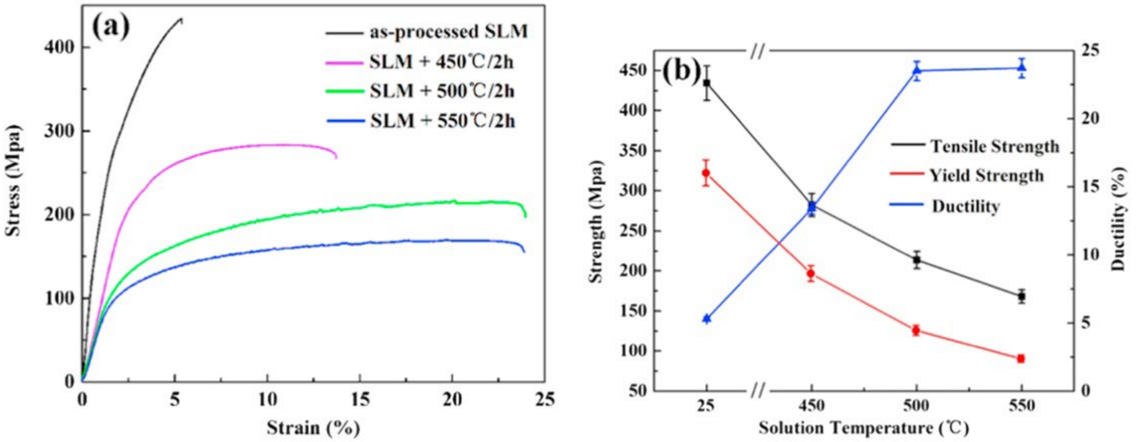

Figure 2-20. Effect of solution treatment temperature on (a) tensile flow behavior, (b) tensile properties [59].

Figure 2-21 (a) shows the microstructure of as-cast Aluminum A205 prior to solution heat treatment, showing the precipitation of Al_2Cu at grain boundaries due to segregation of alloying elements during solidification. Upon solution treatment, most of the grain boundary precipitates dissolved into the matrix. Agglomeration of TiB_2 particles at grain boundaries limits the grain growth to a few microns, as shown in Figure 2-21 [15].

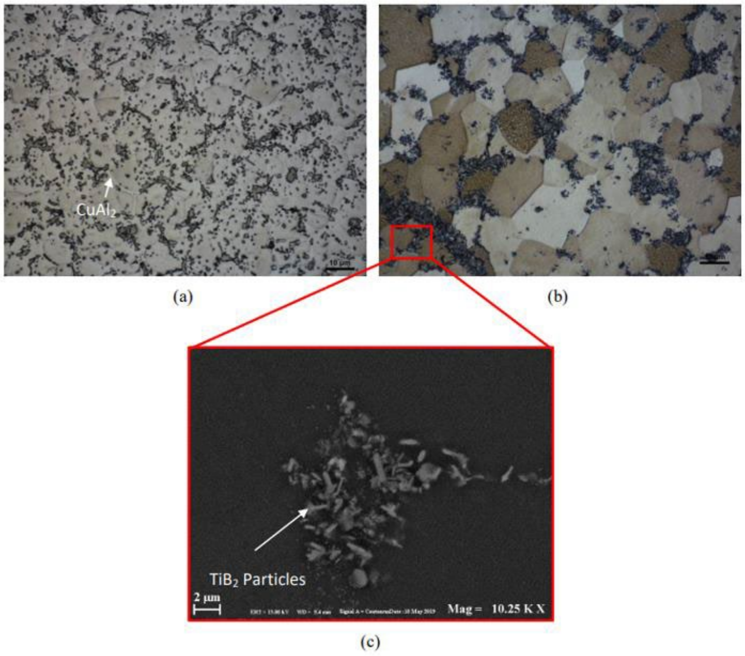

Figure 2-21 SEM microstructure of Aluminum A205: (a) as-cast microstructure showing Al_2Cu at grain boundaries(1000X); (b) Microstructure of solution treated A205 showing agglomeration of TiB_2 particles at grain boundaries (1000 X); (c) SEM micrograph showing the colonies of TiB_2 at grain boundaries [15].

2.9.2 Age hardening treatment

The aging treatment is the final step of the precipitation hardening process. Aging is performed after solutionizing the alloy at a sufficiently high temperature to achieve maximum solubility of the alloying elements. This is followed by rapid quenching to freeze the microstructure and achieve a super-saturated solid solution. The super-saturated state is highly unstable and wants to reach equilibrium. Alloys in this state contain numerous vacancies created during the solution treatment, which acts as nucleation points for precipitation. Heating the alloy to the aging temperature accelerates diffusion and precipitate formation in the matrix. The precipitation process continues until the system reaches an equilibrium state. During the process, the solid solution decomposes, and multiple intermediate phases form, enhancing the strength of the material. The transition between different intermediate phases can occur through the diffusion of atoms, dissolution of a phase, and formation of a more stable phase. The aging process can be stopped when the desired properties are achieved [59].

Formation of the θ phase from the super-saturated solid solution in Al-Cu alloys involves multiple reactions and intermediate phases. The overall sequence of precipitation in the binary Al-Cu system happens as shown in equation (2-1) [14]:

$$asss \rightarrow GPZ \rightarrow \theta'' \rightarrow \theta' \rightarrow \theta. \tag{2.1}$$

In the early stages of aging, disk-shaped clusters called Guinier Preston zones (GPZs) nucleate homogenously across the matrix due to the atomic size mismatch, which imposes strain in the matrix and induces alloy strength. The faces of the disk are totally coherent with the matrix without any strain, while the edges impose considerable strain to the matrix but remain coherent. GPZs are unstable and continue to grow, forming θ'' precipitates, which are similarly coherent with the matrix. θ' precipitates nucleate at dislocations and vacancies, growing at the expense θ'' phase. The faces of θ' are still coherent, but the edges are non-coherent. During the final stage of precipitation, the equilibrium θ (Al_2Cu) phase nucleates at the interface of θ' and the grain boundaries. This step of precipitation involves the loss of coherency between the precipitates and the matrix, leading to the formation of rounded θ particles. Aging at higher temperatures accelerates the achievement of peak hardness by increasing the growth rate of the precipitates. However, the maximum strength achieved is lower compared to the low temperature aging treatments due to lower density of precipitates. To distribute fine precipitates across the microstructure, a double aging treatment can be used. This process includes a low temperature aging treatment for nucleation and growth of fine precipitates up to a critical size, followed by a higher temperature aging treatment to accelerate precipitate growth [14].

Figure 2-22 illustrates the evolution of Al - 4% Cu strength during aging treatment. In the early stages of aging, the primary strengthening mechanism is solid solution strengthening. The formation of GPZs increases the hardness of the alloy through the coherency stress mechanism, creating a stress field in the lattice that acts as barriers against the movement of dislocations, thereby enhancing the strength of the alloy. Peak hardness during aging treatment is obtained when θ'' and θ' precipitates coexist, providing strengthening through both cutting and looping mechanisms. θ'precipitates improve yield strength via the shearing mechanism, while the θ'' precipitates improve strength through Orowan looping, inducing strain hardening and promoting uniform plastic deformation [39].

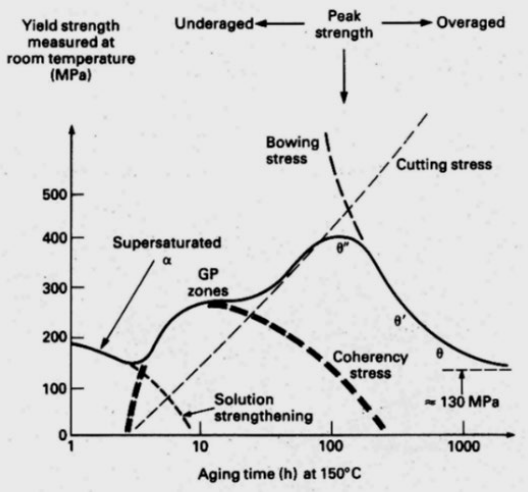

Figure 2-22:Evolution of Al-4%Cu strength during aging at 150 °C [14].

In Al-Cu alloys, the addition of Mg leads to the formation of new intermetallic phases, such as $CuMgAl_2$, as described in Equation (2.2) [39]:

$$\alpha_{SSS} \longrightarrow GPBZ \longrightarrow S' \longrightarrow S(Al_2CuMg). \tag{2.2}$$

Formation of the S phase (Al_2CuMg) in Al-Cu-Mg alloys is similar to the θ phase in the Al-Cu binary system. The process includes the formation of finely distributed coherent GPZs and Guinier-Preston-Bagariatskij zones (GPBZs), and the evolution of meta-stable phases like θ, θ' and S', resulting in the precipitation of non-coherent equilibrium phases such as θ and S [39]. The presence and morphology of the S phase highly dependon the Cu toMg ratio [40]. In Al-Cu-Mg alloys that also contai silver (Ag), an intermetallic phase called Ω is found. The composition of Ω is similar to Al_2Cu and it formshexagonal microstructure precipitates that are found on the {111} planes. The formation of Ω on {111} hinders the movement of dislocations, thereby enhancing the material strength. The addition of silver to the ternary alloy in small quantities promotes the agglomerates of Cu and Mg on {111}, significantly stimulating the formation of Ω. Table 2.3 indicates the various types and crystal structures of precipitates formed in the Al-Cu-Mg-Ag system.

Table 2.3 Crystal structures of different intermetallics observed in the Al-Cu-Mg-Ag system.

Phase	**Crystal structure**	**Reference**
θ	Body-centered tetragonal	[62]
θ'	Body-centered tetragonal	[63]
Ω	Monoclinic	[64–66]
	Hexagonal	
	Orthorhombic	
S	Body-centered orthorhombic	[67]

Figure 2-23 illustrates the typical aging curve of LPBF Al-Zn-Si-Mg-Cu alloy aged at different temperatures. The hardness curve indicates gradual hardening of the alloy with hardening rate proportional to aging temperature. This difference is due to higher diffusion rates at higher temperatures, allowing precipitates to grow faster to their optimum size. It should be noted that maximum hardness is achieved upon coexistence of coherent and incoherent precipitates. As the precipitates grow, the increased spacing between them allow dislocation bypass lowering the hardness of the material [68].

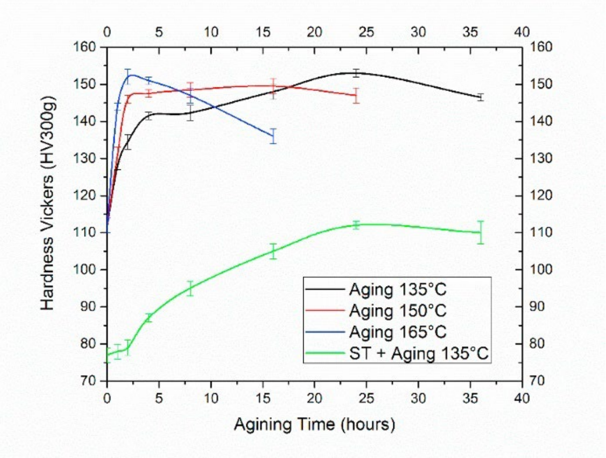

Figure 2-23 Hardness evolution of LPBF-A7068 alloy as function of aging temperature (135, 150,165, and 180°C) [68].

The refined structure of LPBF aluminum alloys facilitates the diffusion of alloying elements in the alloy matrix. Grain boundaries are known to be heterogeneous nucleation sites due to their high diffusion rate [69,70]. During the precipitation hardening process, grain boundaries act as a sink for precipitate-forming elements like Cu, Mg, and Ag [14]. Furthermore, due to the finer grain structure in laser-printed structures, there is a higher possibility of heterogeneous nucleation at grain boundaries compared to cast and wrought alloys. Thus, the kinetics of precipitation in LPBF aluminum alloys is highly influenced by grain size. Therefore, it seems to be necessary to investigate the response of LPBF alloys like A20X to various aging treatments and redefine the aging curves accordingly.

2.10 Laser contour scanning of LPBF alloys

LPBF-built components generally suffer from a poor surface condition due to partial adhesion of non-melted particles, spattering, and staircase effect [71,72]. Thus, the fatigue properties of LPBF-built components are assumed to be lower compared to cast and machined components. Among all the surface treatment procedures, such as shot peening, laser shock peening, and vibratory finishing, the addition of a contour scan around the bulk region has been reported to be the most effective. This is because not all areas of components with complex geometries are easily accessible. Several studies have indicated the effect of contour scan parameters on surface roughness and fatigue performance of LPBF alloys. Reiber et al [73] reported average surface roughness (R_a) of less than 7 µm in Scalmalloy upon application of high energy contour scan. In another study by Buchenau et al. [74], a 60% improvement of surface roughness resulted in a significant enhancement in fatigue performance.

Figure 2-24, acquired by Gockel et al. [71] shows the effect of laser contour scan power and speed on the surface roughness of Inconel 718. Higher contour scan speed and lower laser power resulted in a higher maximum surface valley (Sv) with minimal effect on arithmetic surface roughness (Sa). However, the mechanism of surface roughness evolutions as a function of contour scan parameters was not investigated. The effect of contour scan parameters on fatigue life, as shown in Figure 2-25, exhibited a similar trend to surface roughness, confirming that surface conditions are the main driving factor in the fatigue performance of LPBF alloys.

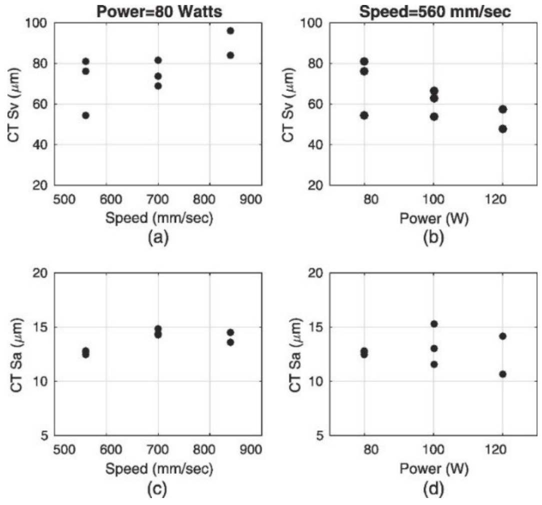

Figure 2-24 Effect of laser contour scan parameters on surface deep valley and average roughness of LPBF Inconel 718 [71].

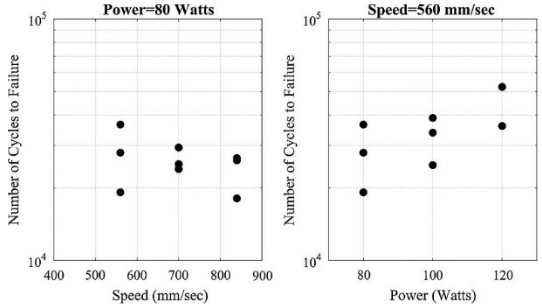

Figure 2-25 Effect of laser contour power and speed on fatigue performance of Inconel 718 [71].

CHAPTER 3 SCIENTIFIC APPROACH

Limited research has been published on the processability and post-fabrication treatment of LPBF A20X. To the best of the author's knowledge, the effects of laser contour scanning on the fatigue performance of LPBF A20X have not been investigated. Moreover, the impact of aging at different temperatures on both mechanical and corrosion properties remains unexplored. The summary of the investigated literature is as follows:

3.1 Critical evaluation of literature review

The knowledge gap between existing literature and the current study arises from the specific characteristics of additively manufactured alloys. In the LPBF process, due to extremely high (10^3-10^7 K/s) cooling rates, there is a significant difference between the microstructure of LPBF alloys and conventionally fabricated metals. This rapid solidification results in highly refined microstructure without any element segregation but can also result in the formation of gas-filled porosities that grow and create larger porosities upon exposure to elevated temperatures. These porosities are called temperature-induced porosities, detrimental to the mechanical properties. Furthermore, rapid solidification might lead to the formation of meta-stable phases and saturated structures that can potentially improve mechanical properties by a post-processing heat treatment [78]. Having an extremely refined microstructure affects the diffusion kinetics of alloying elements and secondary-phase formation significantly, which makes the behavior of LPBF alloys considerably different from conventionally manufactured alloys. Most of the published research on the heat treatment of aluminum alloys is performed on cast or wrought alloys, necessitating re-evaluation of traditional heat treatments for LPBF alloys.

There are very few studies available in the literature on heat treatment of additively manufactured A20X. Avateffazeli et al. [56] have mainly investigated the impact of conventional T7 heat treatment on the mechanical properties of this alloy. However, they did not examine the influence of heat treatment parameters such as temperature and time on microstructure-property relationships in the additively manufactured A20X. Barode et al. [58] investigated the feasibility of a single-step solution treatment and aging at a single temperature.

This study aims to investigate the effect of various heat treatments performed at different temperatures and times on microstructural evolution and mechanical properties of A20X., The goal is to establish an optimized heat treatment that allows fine-tuning of mechanical properties depending on specific application requirements.

1- Direct aging of as-printed A20X:

Due to the high cooling rates (10^3-10^7 K/s) during the LPBF process, there is a strong possibility the alloying elements such as copper, magnesium and silver might not have enough time to diffuse and form equilibrium intermetallics such as θ, S, and Ω precipitates. This rapid cooling can result in the formation of a super-saturated solution microstructure after laser printing. Direct aging treatment aims to either grow previously existing precipitates to optimum size or create new precipitates from a saturated solution. Thus, there is a need to determine whether as-printed A20X responds favorably to direct-aging treatment. The efficiency of natural aging treatment on mechanical properties of A20X alloy has not been studied experimentally in the literature. Direct aging eliminates the need for solution treatment that saves time and energy and benefits from the possible super-saturated structure left from laser printing. Moreover, due to lower temperatures used for direct aging, the refined structure of the as-printed state will be preserved, which is beneficial to maintain higher levels of mechanical properties.

2- Solution and aging treatment of A20X alloy:

In the literature, only T7 heat treatment, which includes a long double-step solution treatment followed by a water quench and aging, has been studied. A20X alloy benefits from high diffusion rates induced by its highly refined microstructure, which facilitates the dissolution of precipitates and eliminates the need for long solution treatments. Furthermore, considering the refined structure and low segregation of LPBF alloys, it seems unnecessary to perform a multi-step solution treatment, as precipitates can rapidly dissolve by reaching a sufficiently high enough temperature. Performing a double-stage treatment appears to have an adverse effect on mechanical properties by promoting grain growth during exposure to high temperatures for a long time (around 500°C). Moreover, the impact of TiB_2 particles on the precipitation behavior of aluminum A20X has never been investigated. In this study, the time and temperature of heat treatment are optimized to adapt a specific precipitation hardening treatment and identify new aging curves for A20X alloy that can be utilized for similar LPBF alloys.

3- Effect of laser contour scanning on fatigue properties of LPBF A20X

Limited research has been conducted on the effect of contour scan parameters on surface roughness, fatigue performance, and the formation of subsurface pores in LPBF alloys. This gap is crucial to address as it directly impacts the reliability and fatigue performance of components manufactured via LPBF. Modification of contour scan speed and offset distance can be used to lower the surface roughness and consequently improve fatigue performance.

3.2 Research objectives

Aluminum alloys are widely used in many industries such as aerospace and automotive. Thanks to their high strength/weight ratio, aluminum alloys can replace conventional alloys. With the rapid advancement of metal AM over the past decade, the need for alloys adapted to additive manufacturing has risen significantly, resulting in a new family of alloys. AM allows engineers to design parts with complex geometries, enabling optimized performance with minimal material. The combination of optimized design and mechanical properties is beneficial both economically and environmentally. Aluminum A20X is a heat-treatable alloy specifically designed for LPBF due to its special properties, such as high strength at room and elevated temperatures and improved fatigue properties.

This research aims to investigate the response of A20X to different precipitation hardening treatments and study the impact of different treatments on the microstructure and mechanical properties of the alloy. At the end, an optimized heat treatment for aluminum A20X fabricated with LPBF is introduced.

1- Investigate the effect of direct aging on LPBF A20X alloy to reduce costs associated with conventional T7 Al alloy heat treatment.
    - Evaluate the effect of direct aging on LPBF A20X microstructure.
    - Evaluate the effect of direct aging on mechanical properties of LPBF A20X

2- Define the optimum solution and age heat treatment for LPBF A20X
    - Evaluate the possibility of short single-step solution treatment to reduce costs associated with conventional double-step solution treatment.
    - Evaluate the effect of solution and aging heat treatment on LPBF A20X microstructure.

- Evaluate the effect of solution treatment and aging on corrosion properties of LPBF A20X
- Evaluate the effect of solution and aging treatment on mechanical properties of LPBF A20X

3- Determine the optimum laser contour scan parameters for fatigue properties of LPBF A20X.

- Evaluate the effect of laser contour scan speed and offset distance on sub-surface defects.
- Evaluate the effect of laser contour scan speed and offset distance on surface topology and roughness.
- Determine the mechanism causing surface roughness variation with contour scan parameters.
- Evaluate the effect of laser contour scan speed and offset distance on low cycle fatigue performance of LPBF A20X

CHAPTER 4 ARTICLE 1: DIRECT AGING OF ADDITIVELY MANUFACTURED A20X ALUMINUM ALLOY

H. Karimialavijeh, M. Ghasri-Khouzani, A. Chakraborty, M. Pröbstle, and É. Martin

Published in Journal of Alloys and Compounds on September 7th 2023

(https://doi.org/10.1016/j.jallcom.2023.172071)

4.1 Abstract

This study investigates the effect of direct aging on a newly developed high-performance aluminum alloy A20X for laser powder bed fusion. Three different temperatures (180 °C, 200 °C, and 220 °C) and nine different heat treatment durations (5 min to 30 h) were considered. The material exhibited significant softening (up to 23.7% hardness drop) after direct aging. The extent of softening was proportional to the temperature and duration of heat treatment. During direct aging, incoherent Al_2Cu (θ) precipitates ($\{110\}_{\theta} \parallel \{220\}_{Al}$) coarsened and the volume fraction remained constant (4.52-4.63%). The average precipitate size grew by up to ~100% through direct aging and no metastable precipitates (such as θ' or Ω) formed, suggesting the absence of supersaturated matrix in as-printed A20X. Accordingly, the yield and tensile strengths of the alloy dropped by up to 27% and 19.4%, respectively. The continuous Mg/Ag solute wall observed at grain boundaries in the as-printed state caused serrated plastic flow due to the locking/unlocking of dislocations. Longer aging treatments generated discrete solute co-clusters along the grain boundaries and TiB_2/Al interface promoting smoother plastic flow.

Keywords: Additive Manufacturing; direct aging; aluminum alloy; metal matrix composite; microstructure; mechanical properties

4.2 Introduction

Laser powder bed fusion (LPBF) technology has garnered widespread interest owing to its capability in fabricating complex geometries with fine surface finish (4 µm) and small feature sizes (50 µm) [75]. The process is adaptable to various metallic alloys, including nickel alloys [76–81], steels [82–84], titanium alloys [85,86], magnesium alloys [87–89] and aluminum alloys [90–93]. Cast aluminum alloys, such as A356, A357, Al-Si10Mg, and Al-12Si exhibit excellent LPBF processability due to their high fluidity and low thermal shrinkage [94]. In contrast, wrought aluminum alloys, including Al-Cu, Al-Mg, and Al-Zn series, demonstrate poor printability and high solidification cracking susceptibility owing to their large solidification range and shrinkage [94]. Prior works have assessed the effects of adding Si, Zn, and Mg to alloy chemical composition [95], preheating the powder bed or build plate [96], replacing continuous wave laser mode with a pulsed wave laser mode [97], and using an inoculation treatment [98] on LPBF printability. The inoculation treatment includes in-situ or ex-situ inclusion of heterogenous nucleating agents such as TiB_2, LaB_6, TiH_2, ScH_3, Al_3Ti, ZrH_2, TiC, CaB_6, and TiN [93,98,99]. For example, the ex-situ addition of TiB_2 nanoparticles to an Al-Cu-Ag-Mg alloy (producing A20X) improves the mechanical properties through grain refinement [100].

Heat-treatable aluminum alloys fabricated by conventional techniques (such as casting and forming) require a two-stage solution and aging heat treatment to enhance mechanical properties [101]. However, the LPBF-built aluminum alloys exhibit fine supersaturated microstructure owing to extremely high cooling rates (10^4-10^6 °C/s) inherent to the LPBF process [36]. Accordingly, the first stage of precipitation hardening treatment (solution treatment) can be bypassed and succeeded by direct aging to preserve fine grain size and maximize post-processing cost-efficiency. Direct aging heat treatment has been previously used for LPBF-fabricated AlSi10Mg [102,103], Al-Zn-Mg-Cu-Ta [104], AlSi7Mg0.6 [105], Zr-added 2024 [106], AlSi8.1Mg1.4 [107], and AlSi3.5Mg2.5 [108]. For example, direct aging of as-printed AlSi10Mg at 130 °C promoted the formation of Si-rich precipitates and enhanced the tensile strength by 12% without reducing the ductility [102]. In another study [106], direct aging of a Zr-added 2024 alloy at 370 °C promoted the precipitation of nano-size L12-Al_3Zr dispersoids in the microstructure without grain coarsening. Subsequently, the yield strength increased by 16 %, elongation dropped by 47 %, and the tensile strength remained unchanged [106]. Zhang et al. [108] reported that the yield stress and tensile strength of LPBF-built AlSi3.5Mg2.5 did not improve noticeably (<3 %) upon direct aging at 170 °C. In the comprehensive reviews performed by Laleh et al. 2023 [109] and Fiocchi et al. 2021 [110], the authors reported coarsening of Si particles and softening of LPBF Al-Si alloys upon annealing at temperatures above the precipitate growth threshold. Overall, the presented literature has several discrepancies and the reported heat treatments are not optimized for new generations of aluminum alloys made for LPBF and the response of the alloy to heat treatment is highly affected by manufacturing parameters [110].

The A20X alloy is a recently developed high-performance metal matrix composite (MMC) consisting of TiB_2 ceramic particles and Al-Cu-Ag-Mg aluminum matrix. The alloy is known for its high strength at elevated temperatures making it a great candidate for aerospace applications such as heat exchangers. A20X benefits from multiple strengthening mechanisms, including grain refinement by TiB_2 particles, precipitation, and solid solution hardening by Cu, Mg, and Ag alloying elements [100]. A post-fabrication hardening treatment is required to achieve optimum mechanical properties. However, all studies on heat treatment of as-printed A20X have focused on conventional T7 heat treatment [58,111,112]. To the authors' knowledge, the direct aging possibility of A20X has not been investigated yet.

This study investigates the effect of direct aging heat treatment on the microstructure and mechanical behavior of A20X alloy. Advanced microscopic characterization was carried out to study the microstructural evolutions and phase transformations during the direct aging of the alloy. Mechanical testing was also performed to study the effect of microstructural evolutions on the mechanical properties.

4.3 Experimental procedure

4.3.1 Powder and LPBF process

Pre-alloyed gas-atomized A20X aluminum powder particles with spherical shape and 15-53 μm (D_{10}-D_{90}) particle size range were used to fabricate the parts in this study. The nominal chemical composition of the powder provided by the supplier is listed in Table 4.1. Cylindrical bars with 100 mm height and 8 mm diameter were fabricated using a Concept Laser M2 Series 5 LPBF machine. The orientation of the cylindrical bars with respect to the build plate is schematically illustrated in Figure 4-1(a). In all cases, the LPBF process parameters were set as follows: laser power 370 W, beam diameter 175 μm, scan speed 1250 mm/s, hatch spacing 140 μm, and powder layer thickness 40 μm. Nitrogen gas was purged into the printing chamber during the fabrication to keep the oxygen level below 0.1 %.

Table 4.1 Nominal chemical composition of the A20X powder (wt. %)

Cu	**Ti**	**B**	**Ag**	**Mg**	**Si**	**Fe**	**Al**
4.55	3.61	1.36	0.83	0.29	0.07	0.06	Balance

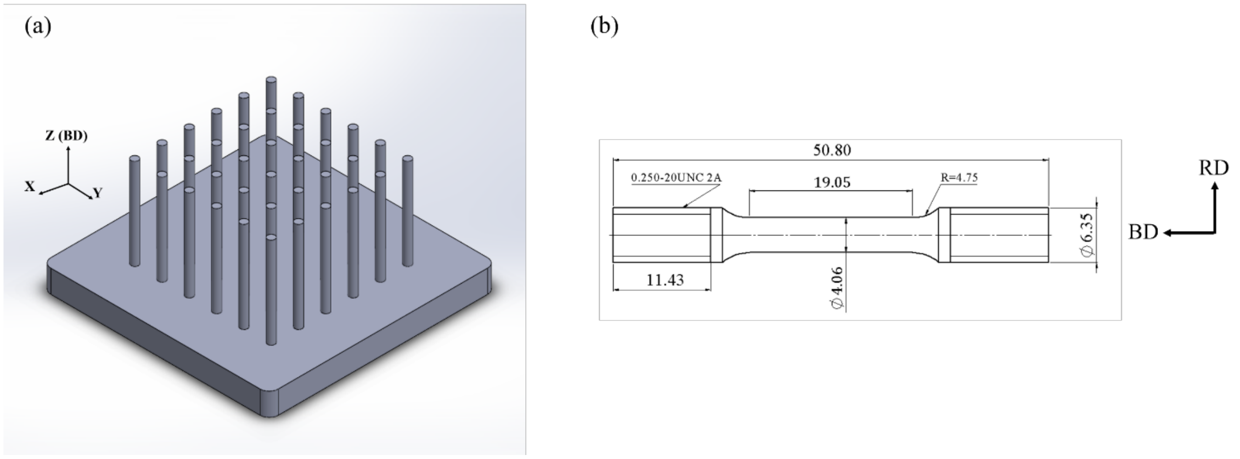

Figure 4-1 Schematic illustration of the LPBF-built parts. (b) Geometry and dimensions of the tensile specimens used in this study. All dimensions are in mm. The build direction (BD) and radial direction (RD) of tensile bars are presented here.

4.3.2 Post-process heat treatment

Upon fabrication, direct aging heat treatments were conducted using a Thermo Scientific Heratherm oven. The as-built bars were heated to three different aging temperatures (180, 200, and 220 °C) at a heating rate of 5 °C/min. The samples were held at these temperatures for various aging times (5 min to 30 h) and air cooled to room temperature.

4.3.3 Microstructural characterization

As-built and aged specimen were ground with grinding paper and polished with diamond suspensions and colloidal silica to a 0.04 µm finish. Microstructure characterization was performed using a JEOL JSM-7600F field emission gun scanning electron microscope (FEG-SEM) at an accelerating voltage of 5 kV and a working distance of 8 mm. The fracture surfaces of tensile specimens were inspected to determine the failure modes before and after aging. The line intercept method per ASTM E112-13 standard was used to determine the average grain size using the SEM micrographs [113]. The equivalent area method was used to quantify the size of the precipitates [114]. The area of the precipitates was first obtained from the SEM images using ImageJ software [115], then the equivalent diameter was obtained algebraically.

A JEOL JEM-2100F transmission electron microscope (TEM) equipped with an energy dispersive spectrometer (EDS) was used to study nano-precipitates in both as-built and heat-treated specimens. Both TEM and STEM investigations were carried out at a 190 kV accelerating voltage. Vertical sections (XZ surfaces) of the samples were ground and polished using a Gatan disc grinder. The sample thickness was further reduced by focused ion beam (FIB) thinning using a HITACHI FB-2000A FIB.

X-ray diffraction (XRD) was conducted using a Bruker D8 Advance diffractometer with Cu Kα radiation to identify and quantify the volume fraction evolution of secondary phases with aging. The diffraction instrument was operated at 40 kV and 40 mA with an 18-100° 2θ range and 0.02° step size. X'pert High Score Plus software, coupled with the ICDD-PDF4+ database, was used to quantify different phases. Dislocation density was measured using the Williamson-Hall method [116].

4.3.4 Mechanical testing

Cylinders (10-mm length) were cut from as-fabricated and heat-treated bars for hardness testing. Horizontal sections (XY surfaces) of the specimen were ground and polished. Vickers micro-hardness testing was carried out using an Akashi Mitutoyo MVK-HO tester with a load of 1.96 N and a hold time of 15 s. Average micro-hardness values were determined from 10 indentations for each condition.

Round tensile specimens with 19.05 mm gauge length and 4.06 mm diameter were machined from both as-built and heat-treated bars, as shown in Figure 4-1 (b). Room temperature tensile tests were carried out using an MTS 810 machine at an initial strain rate of 10^{-3} s^{-1}. An MTS 632.13F-20 extensometer was used to measure the elongation during the tensile tests. All tensile tests were run up to specimen failure. Three tests were conducted for each condition to ensure result repeatability.

4.4 Results and discussion

4.4.1 Microstructure of as-printed A20X

The microstructure of the as-printed A20X was studied in planes parallel and perpendicular to the build direction. Grains showing fully equiaxed morphology and no signs of epitaxial growth in the build direction (heat flow direction) were observed. The representative SEM micrograph is shown in Figure 4-2 (a). As-printed A20X consists of small equiaxed grains (average grain size = 1.02 µm ±0.16) with fine Al_2Cu (θ) precipitates (< 200 nm) observed in intragranular regions and at grain boundaries. The volume fraction of Al_2Cu precipitates was 4.52-4.63 %, according to the X-ray diffraction analysis (not shown here). Titanium diboride (TiB_2) particles with sizes below 1 µm were also homogenously dispersed in the microstructure. These particles are added to A20X to create a fully equiaxed microstructure and random texture. To prevent epitaxial grain growth in aluminum alloys, a minimum of 2 wt.% of TiB_2 particles are required [117]. A20X alloy contains 4.5-5 wt.% of TiB_2 particles based on the X-ray diffraction analysis. The IPF map in Figure 4-2 (b) shows random grain orientation in the as-printed state.

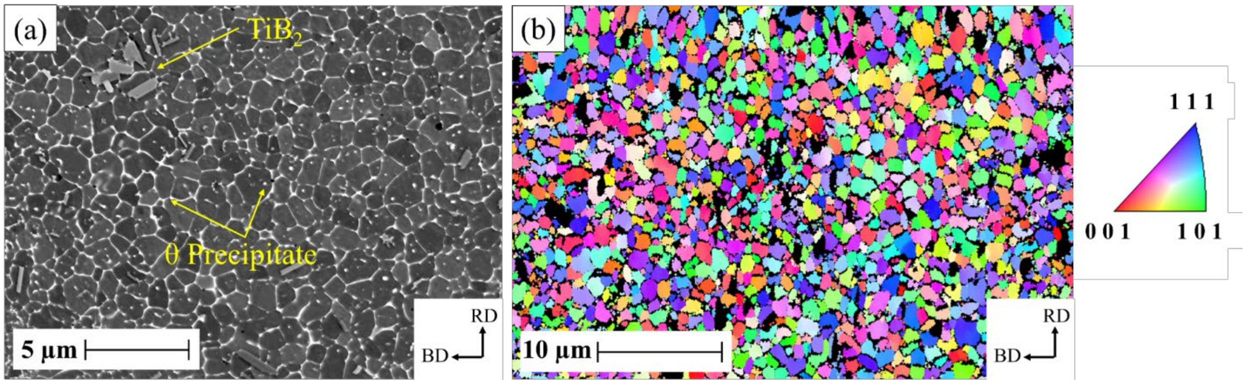

Figure 4-2 Microscopic characterization carried out on as-printed A20X in the plane parallel to the build direction. (a) Fine cellular structure, precipitates (θ), and TiB_2 particles observed in SEM micrograph, (b) EBSD IPF map depicting grain orientations with respect to the build direction. The build direction (BD) and radial direction (RD) correspond to the specimen axis in Figure 4-1.

4.4.2 Effect of direct aging on the A20X LPBF microstructure

The effect of direct aging on the A205 LPBF hardness is shown in Figure 4-3. In the as-printed condition (see annotation in Figure 4-3), the hardness was 118±2 HV. Following direct aging, the hardness decreased continuously with aging time and temperature and no peak hardness was observed. For example, at 180 °C, the hardness decreased to 107± 1 HV, ~10% lower than the as-printed condition (~118 HV) after 12 hrs of aging (point A in Figure 4-3). The microstructure of the alloy did not show significant change compared to the as-printed condition (micrograph A in Figure 4-3). Increasing the aging time to 30 hrs further reduced the hardness by 14.5% to 101± 1 HV and resulted in precipitate coarsening (see micrograph B in Figure 4-3). Higher aging temperatures also caused further softening of the alloy. For instance, after aging at 200 °C for 12 hrs (point F in Figure 4-3), the hardness drops by 19.5% to 95± 1 HV. The lowest hardness observed in this study was 90±2 HV (~23.7 % hardness reduction), corresponding to the sample aged at 220 °C for 30 hrs. By increasing the duration and temperature of treatment, the continuous Al_2Cu grain boundary network broke into particles then coarsened. This is evident when comparing micrographs B, D, E-G in Figure 4-3. However, the grain size of LPBF A20X (see top right corners of SEM images in Figure 4-3) did not change significantly with the direct aging conditions evaluated here. In all the cases, grain sizes remain within the standard deviation of the measured initial grain size (1.02 ± 0.16 µm). Precipitates observed along the grain boundaries prevent grain growth through the Zenner pinning mechanism [118].

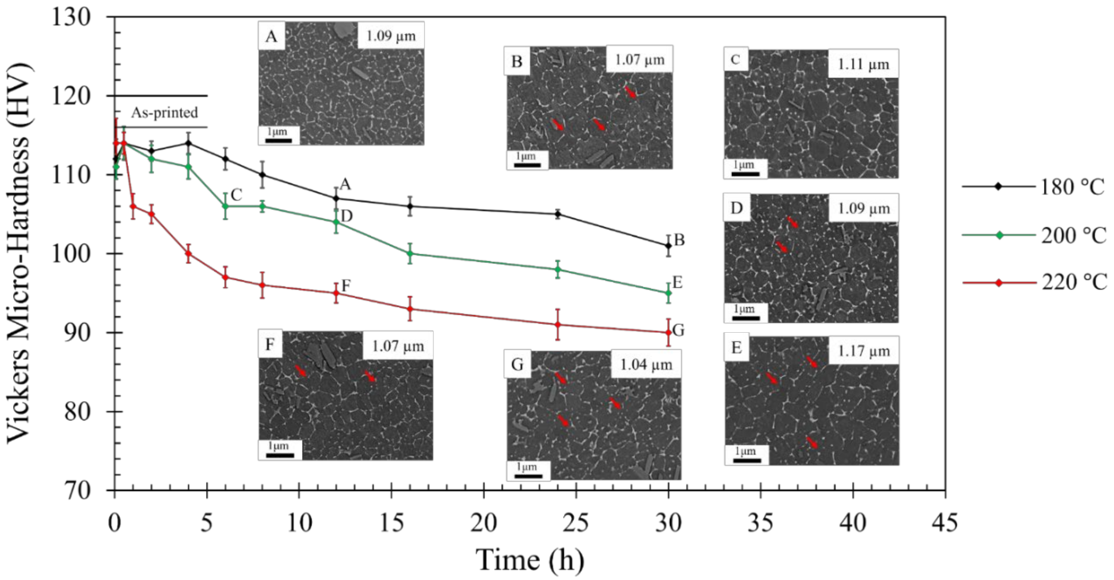

Figure 4-3 Micro-hardness variations with aging temperature and time for the LPBF fabricated A20X alloy. The hardness range of as-printed A20X is distinguished using two black lines (considering the standard deviation). SEM micrographs of direct-aged A20X after 12 and 30 hours of heat treatment for different temperatures are shown. The grain sizes are shown in the top-right corners of the SEM micrographs. Red arrows highlight disruption of grain boundary precipitates during direct aging.

The average size of Al_2Cu precipitates is shown in Figure 4-4 for the different heat treatments investigated in this study. The average precipitate size increased proportionally with aging temperature. In the as-printed condition, the precipitate size was 78 ± 33 nm. Following direct aging at 180 °C for 30 hours, the precipitates grew by 29% to 101± 25 nm. Accordingly, for the same aging time, the average precipitate size increased to 111± 21 nm and 156.7± 39.6 nm as aging temperature increased to 200 °C and 220 °C, respectively.

To better understand precipitate evolution with aging, it is necessary to consider the critical precipitate radius (R*) given by Eq. (1) taken from [119].

$$R^* = \frac{2\gamma V_{at}}{kT\ln\left(\frac{C}{C_{eq}}\right)} \tag{4.1}$$

where γ is the interfacial energy between the matrix and precipitate, V_{at} atomic volume of the precipitate, k Boltzmann's constant, T aging temperature, C current solute concentration, and C_{eq} equilibrium solute concentration in the matrix. The precipitate dissolves within the matrix when its radius is below R* and grows when its radius exceeds R*. It is evident from Eq. (1) that the critical precipitate radius decreases by raising the aging temperature. Higher aging temperatures promote further precipitate coarsening and growth.

The formation and growth of new precipitates are highly favored in the presence of a supersaturated solid solution [58]. In the present work, the Al_2Cu (θ) volume fraction measured by XRD remained relatively constant (4.52-4.63 %) after direct aging treatment, as shown in Figure 4-4. This is dissimilar to usual observations in other LPBF aluminum alloys where the precipitation volume fraction increased significantly upon direct aging [102,107,108,120,121]. The findings here suggest as-built A20X is not in supersaturated solid solution. The Al_2Cu (θ) volume fractions observed in Figure 4-4 are lower than the equilibrium value predicted by Ghasri-Khouzani et al. 2023 [36]. This is because the solubility of elements in the matrix increases at high cooling rates as in the LPBF process [39–44]. This lowers the contribution of solute atoms on precipitate formation, resulting in lower precipitate volume fraction compared to equilibrium solidification.

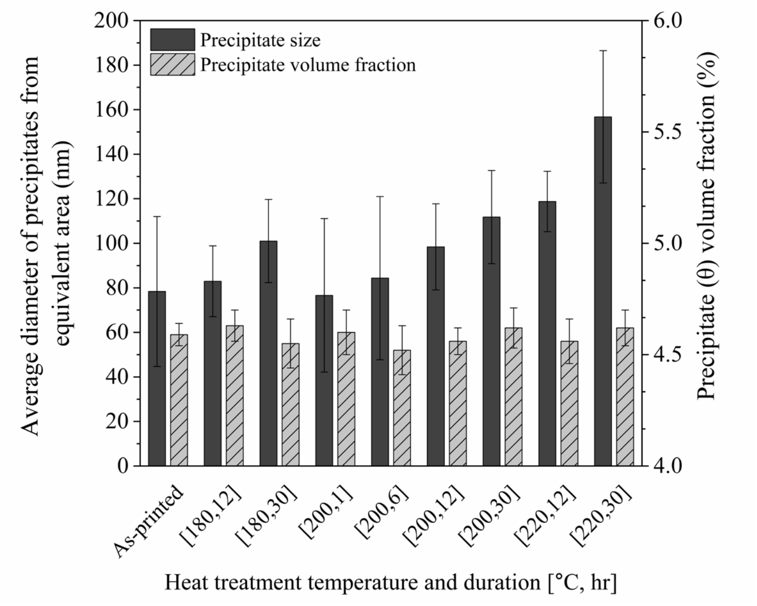

Figure 4-4 Average precipitate (θ) size and volume fraction as functions of temperature and duration of aging treatment in LPBF-A20X.

Solute partitioning characteristics in the as-printed and aged state (220 °C for 30 hrs) were compared using TEM-EDS in Figure 4-5. In the as-printed condition (Figure 4-5 (a)), continuous films rich in Cu, Mg, and Ag decorated grain boundaries. Copper is found in the form of θ precipitates (Al_2Cu) in combination with aluminum. In comparison, magnesium and silver are primarily found in the form of solute co-clusters due to their strong bonding [122–124]. Direct aging at 220 °C for 30 hrs facilitated the diffusion of elements, disrupting the continuous precipitate (θ) film and forming globular precipitates at grain boundaries, as shown in Figure 4-5 (b). These observations agree with the results acquired from SEM analysis (Figure 4-3). Furthermore, the solute co-clusters rich in Ag and Mg covering grain boundaries grew exponentially after direct aging and agglomerated independently from Al_2Cu (θ) phase. It should be noted that the contributing elements in the precipitates and solute co-clusters (shown in Figure 4-5) remained the same.

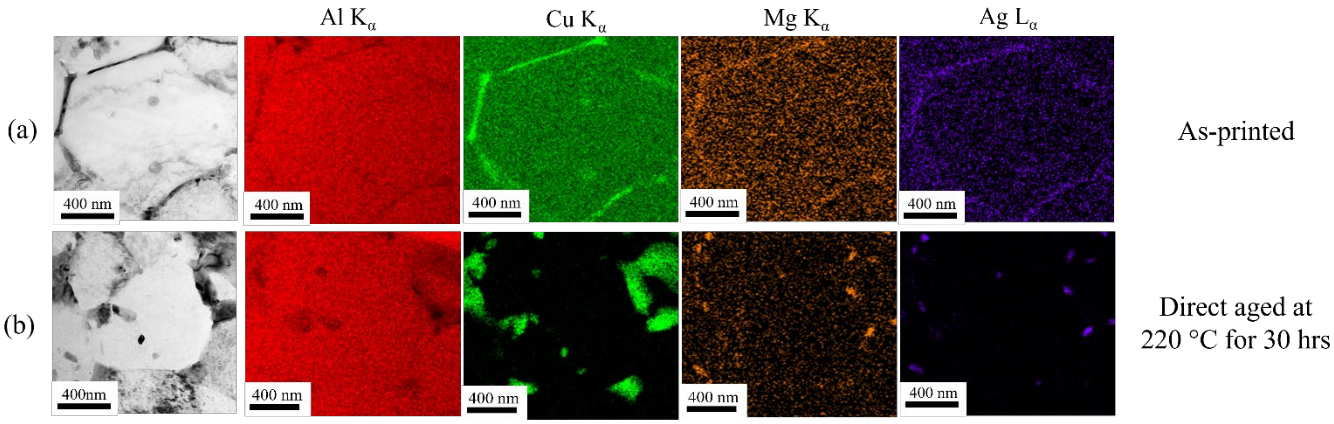

Figure 4-5. TEM-EDS map showing the distribution of precipitate forming elements in (a) as-printed, and (b) direct aged at 220 °C for 30 hrs A20X.

Characteristics, such as size, habitat plane, and coherency of the Al_2Cu precipitates were investigated using TEM bright field images and selected area electron diffraction (SAED) patterns, as shown in Figure 4-6. Comparison between the as-printed (Figure 4-6 (a)) and direct-aged conditions Figure 4-6 (c) shows no evident growth of the intragranular nano-precipitates. These precipitates were observed along [001] FCC Al zone axis in both as-printed (Figure 4-6 (b)) and direct-aged (Figure 4-6 (d)) conditions. In both cases, the stronger and weaker diffraction spots were indexed to be α-Al matrix and θ-Al_2Cu precipitates ($\{110\}_\theta \parallel \{220\}_{Al}$), respectively. This implies that incoherent Al_2Cu (θ) precipitates underwent no phase transformation during the direct aging heat treatment. Moreover, the formation of new precipitates (θ′ and Ω) was not observed after direct aging. All Al_2Cu precipitates in Figure 4-6 were likely present in the overaged condition because the morphology (faceted) and phase type (BCT-θ) were identical in the as-printed and direct-aged A20X. The absence of meta-stable precipitates in the direct-aged alloy confirms that the only active mechanism during direct aging is the growth of already existing incoherent Al_2Cu (θ) precipitates.

Two possible mechanisms could explain the over-aged state of the as-printed A20X. First, re-heating from the subsequent build layers provides enough thermal energy for the diffusion of supersaturated elements. This favors transformation of metastable structures into in-coherent globular Al_2Cu (θ) precipitates. However, Ghasri-Khouzani et al. 2023 [92] showed recently that the Al_2Cu (θ) are already in over-aged state after single track deposition. The precipitates observed in the single tracks of A20X were mainly intragranular and grain boundary Al_2Cu (θ), similar to those observed in the present study. Thus, the over-aged structure cannot be caused by re-heating during the fusion of subsequent layers of powder.

Despite the high cooling rates associated with the LPBF process, Tan et al. 2022 [125] showed that the rejection of alloying elements such as Cu, Mg, and Ag into liquid still occurs. However, the grains need to grow large enough to contain sufficient solute atoms (Cu, Mg, and Ag) forming a supersaturated solid solution after cooling to room temperature. For A20X, Ti and TiB_2 promote heterogeneous nucleation and sub-micron grain structure. The solute atoms mostly remain within the last liquid to solidify, forming a continuous film of intermetallic particles along the grain boundaries, as shown in Figure 4-5. The high grain boundary volume fraction (fine grain size) is likely to facilitate solute element diffusion and the formation of stable Al_2Cu (θ) and Mg-Ag clusters.

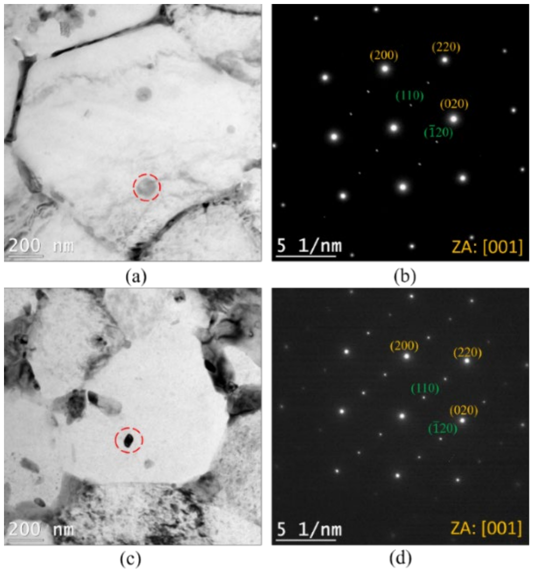

Figure 4-6 TEM bright field images and corresponding SAED patterns: (a,b) as-built and (c,d) aged at 220 °C for 30h. Reflections from the Al matrix and Al_2Cu precipitate are indexed in yellow and green, respectively. ZA denotes the zone axis. SAED patterns were acquired from regions highlighted by red dashed circles.

4.4.3 Effect of direct aging on plastic flow in LPBF A20X

Representative true stress-strain plots for tensile behavior of both as-built and heat-treated A20X specimens are shown in Figure 4-7. All samples exhibited discontinuous yielding (yield point phenomenon) indicating heterogenous deformation. The yield point phenomenon comprises a sudden drop from upper to lower yield stress and a plateau region over which true stress does not change significantly. The phenomenon is commonly explained by the locking of dislocations by clustering of highly mobile solute atoms at dislocations [126]. Mg and Cu atoms exhibit fast diffusion rates in aluminum, particularly in the presence of each other [127]. The diffusion rate is further accelerated by the higher volume fraction of grain boundaries, as shown previously in [128]. This is typical of the refined microstructure inherent in LPBF-processed materials [92].

As-printed A20X has a steeper slope compared to the direct-aged specimen, as shown in Figure 4-7. This suggests higher strain hardening capacity of as-printed A20X, which is attributed to the presence of solute atoms (Cu, Mg, and Ag), fine intra-cellular precipitates (θ), and continuous network of precipitates at the grain boundaries [129]. Upon direct aging, the post-yield work hardening parameter of A20X decreased with the temperature and duration of heat treatment. This coincides with the formation of larger precipitates and reduced solute concentration in the matrix, as shown in Figure 4-5.

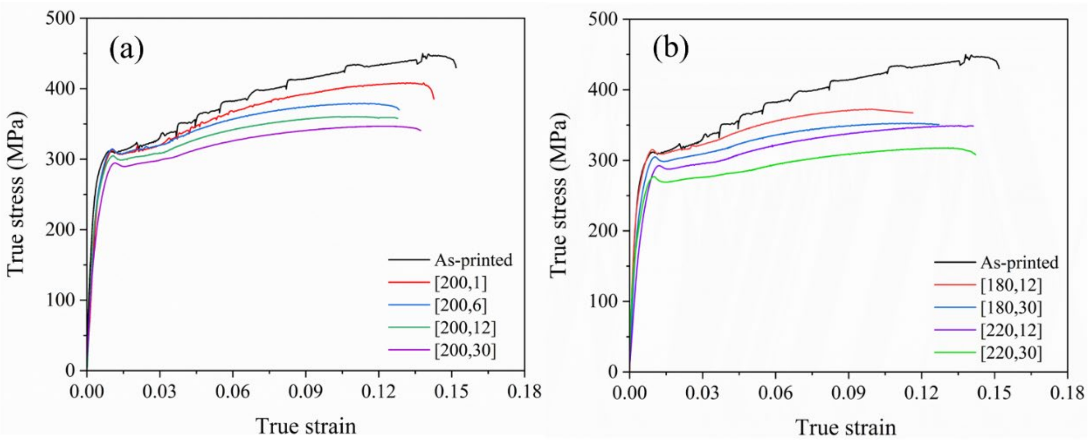

Figure 4-7 Comparison between tensile properties of A20X in (a) as-printed and direct aged at 200 °C, (b) 180 °C and 220 °C (as-printed tensile graph is shown in both graphs for comparison purposes).

The as-printed material in Figure 4-7 also exhibited step-like serrations during plastic deformation. These are characteristic of type D serrations [130,131]. The serrated flow, also known as Portevin-Le Chatelier (PLC) effect, is attributed to the locking and unlocking of dislocations by solute atoms and/or precipitates [130–133]. The PLC effect has been previously observed during tensile deformation of LPBF-fabricated A20X [36,100]. However, no signs of serrated plastic flow were observed in the as-cast A20X, according to Avateffazeli et al. 2022 [134]. This difference is attributed to the significantly finer grain size in the LPBF A20X (~1 μm) compared to cast A20X (~50 μm) [135–138]. Coarse grain size facilitates cross-slipping and formation of multiple slip systems producing smoother plastic deformation [139,140].

Direct aging of the A20X alloy decreased the intensity of serrations in Figure 4-7. The effect of direct aging time at 200°C on the type D serrations can be observed in Figure 4-7 (a). Increasing the heat treatment time decreases the serrations up to 6 hrs, beyond which serrations are only observed close to the yield point and cease to occur after 12 hrs. The same behavior was observed at 180°C and 220°C, where the serrations were not observed when heat treatment duration exceeded 12 hrs. Figure 4-7 (b) shows four examples of heat treatment at 180°C and 220°C for 12 hrs and 30 hrs. Plastic flow serration is highly affected by grain size and solute elements (Mg and Ag in A20X)/dislocation interaction [131,141,142]. However, in the present work, the grain size remained relatively constant, as shown in Figure 4-3.

The serrations can be further analyzed using stress decrements that represent the amount of stress drop for each serration, as done in [143,144]. In Figure 4-8, stress decrements for the as-printed and aged specimens decreased with accumulated strain. At the early stages of plastic deformation, the gliding dislocations pile up around precipitates and grain boundaries [145]. This gives enough time (called waiting time) to solute atoms like Mg and Cu to diffuse towards the grain boundaries and pin the dislocations effectively. According to Kubin et al. 1990 [146] and Hu et al. 2021 [147], the dislocation waiting time decreases gradually with accumulated strain. This explains the gradual decrease in stress decrement in both as-printed and direct-aged specimens shown in Fig. 8. For the direct-aged specimen, the stress decrements were slightly lower compared to the as-printed condition. This is attributed to the lower amount of solute (Cu, Mg) atoms remaining in the matrix (see Figure 4-5) to effectively pin the dislocations.

The strain interval between subsequent serrations increased with accumulated strain in the as-printed specimen, as shown in Figure 4-8. This is likely due to reduced dislocation mobility resulting in prolonged pinning of dislocations [129,146]. However, the strain interval is significantly lower and relatively constant in direct-aged specimen.

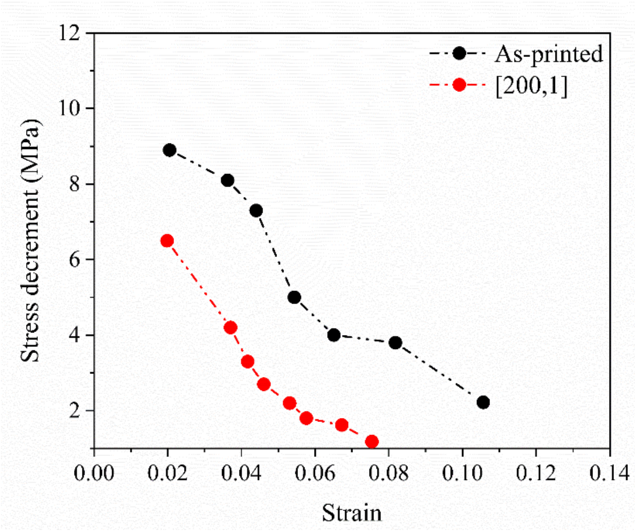

Figure 4-8 Stress decrements as a function of onset strain for each serration during plastic deformation in specimens with highest degree of dynamic strain aging (DSA) observed in this study. As-printed and aged at 200 C for 1 hr ([200,1]) specimens are shown using black and red curves, respectively.

Considering the interaction between dislocations and solute elements, the effect of direct aging temperature and duration on dislocation density is studied in Figure 4-9. The initial dislocation density of the as-printed A20X was around 9.72×10^{14} m^{-2}, inherent to laser-processed aluminum alloys [1]. This is 5-10 times larger compared to conventionally fabricated aluminum alloys subjected to slower cooling rates [148–150]. After 1 hr of direct aging at 200°C, the dislocation density decreased slightly to 8.81×10^{14} m^{-2}. This reduction is attributed to the relaxation of residual stresses and annihilation of dislocations following exposure to elevated temperatures [1]. When the aging time increased to 6 hrs, the dislocation density decreased to 5.05×10^{14} m^{-2} and remained relatively constant thereafter. Similar unvarying dislocation densities were observed at other aging temperatures for long durations (see Figure 4-9). Despite the low dislocation density after direct aging at 200°C for 6 hrs, flow curves in Figure 4-7 (a) still exhibit some evidence of serration. This implies the initial dislocation density does not affect the serrated plastic flow.

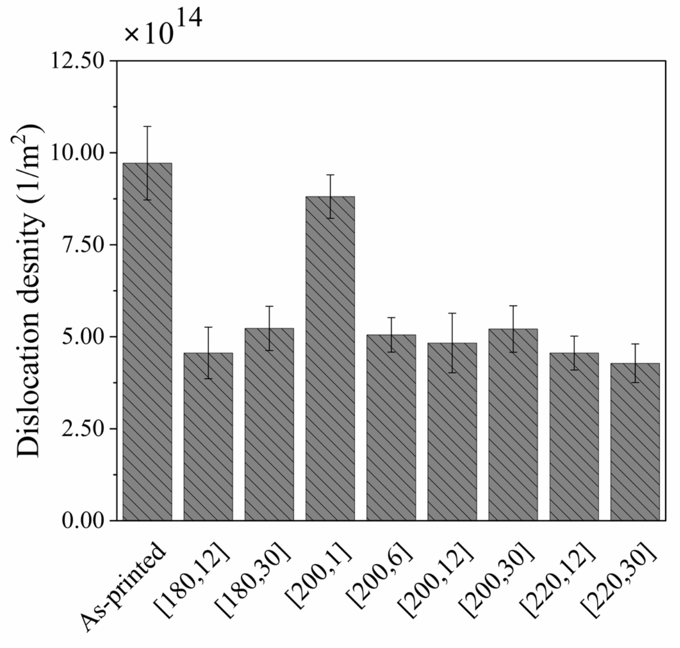

Figure 4-9 Dislocation density measured by X-ray diffraction for LPBF-printed A20X direct-aged at various temperatures and durations.

During direct aging, the continuous solute-rich Mg/Ag layer gradually breaks into smaller particles, as shown in Figure 4-5. Disintegration of the Mg/Ag layer along the grain boundaries reduces the probability of dislocation pileup at grain boundaries, gradually eliminating the unstable plastic flow observed in Figure 4-7. He et al. 2021 [131] reported similar behavior, where the disappearance of solute-rich diffuse wall led to the elimination of serrated plastic flow in LPBF-printed A5024. Precipitate network discontinuities along the grain boundaries are demonstrated in Figure 4-3. The connectivity remains strong after 1 hr and 6 hrs at 200 °C and dissipates after 12 hrs (see red arrows in Figure 4-3). This coincides with the disappearance of the serration in the flow curves in Figure 4-7.

Mg-Ag clusters can be observed around TiB_2 particles after direct aging at 200 °C for 30 hrs in Figure 4-10. This is attributed to the large thermal expansion mismatch between the aluminum matrix (26.5×10^{-6} K^{-1}) and titanium di-boride particles (7.7×10^{-6} K^{-1} - C axis) [151,152], which creates a strain field facilitating diffusion of the solute elements. Increased solute diffusion promotes absorption of solute atoms to preferential regions (TiB_2/Al interface) within the grain. This removes the elements contributing to the PLC mechanism from the matrix and reduces the serrated plastic flow.

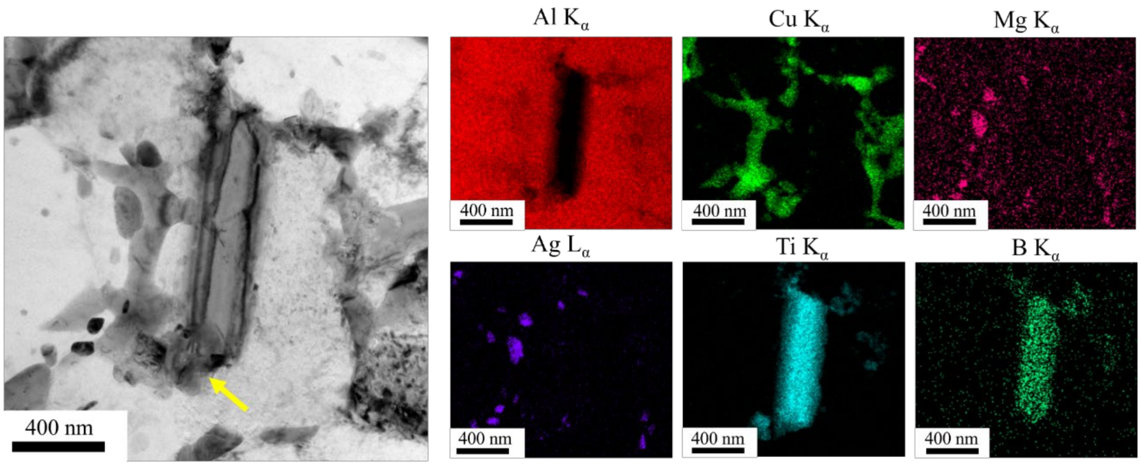

Figure 4-10 TEM-EDS map showing agglomeration of alloying elements around TiB_2 particles in specimen direct aged at 220 °C for 30 hrs. The yellow arrow indicates a solute (Cu, Mg, and Ag) cluster.

4.4.4 Effect of direct aging on Tensile properties

The tensile characteristics (Yield stress (YS), ultimate tensile strength (UTS), and elongation at failure obtained from the tensile plots are shown in Figure 4-11. The direct-aged samples exhibited lower yield stress and tensile strength compared to the as-built alloy. The yield and tensile strength of the A20X in the as-printed condition were 289.7± 1.5 MPa and 390.3± 2.5 MPa, respectively. For instance, the yield and tensile strengths dropped to 210.6 ± 2 (~27%) and 314± 2.1 (~20%), respectively, after direct aging at 220°C for 30 hrs. The deterioration of the mechanical properties coincides with the coarsening of the Al_2Cu precipitates observed in Figure 4-3 and Figure 4-6. For age-hardenable Al-Cu alloys, stable θ-Al_2Cu precipitates with globular morphology or grain boundary precipitates are not considered effective strengthening mechanisms. Precipitate hardening is primarily achieved by semi-coherent metastable θ′-Al_2Cu precipitates [153], not observed here. Moreover, agglomeration of alloying elements like Cu/Mg/Ag co-clusters (shown in Figure 4-5) is expected to reduce their contribution to the precipitate and solid solution strengthening, resulting in significant softening of the alloy, as shown in Figure 4-3.

Material ductility decreased after direct aging, as shown in Figure 4-11 (c). This contradicts typical observations where the ductility is expected to increase upon softening. According to De et al. 2011 [154], the ductility of ultra-fine grain aluminum alloys depends on the size and distribution of secondary phases. The authors attributed the high ductility before annealing to the higher fraction of low misorientation low angle grain boundaries (LMLAGBs) formed near secondary phases. After annealing, the precipitates coarsened and LMLAGB fraction reduced resulting in lower material ductility. This could explain the lower ductility after direct aging caused by precipitate coarsening observed in this study (Figure 4-11(c)).

Moreover, precipitates (θ) and clusters (Cu/Mg/Ag) could act as preferential sites for void formation under uniaxial loading, which could affect the material ductility [155]. In this case, precipitate/cluster growth only became increasingly noticeable after 12 hrs (Figure 4-3), corresponding to the slight increase in ductility observed between 12 hrs and 30 hrs (Figure 4-11 (c)).

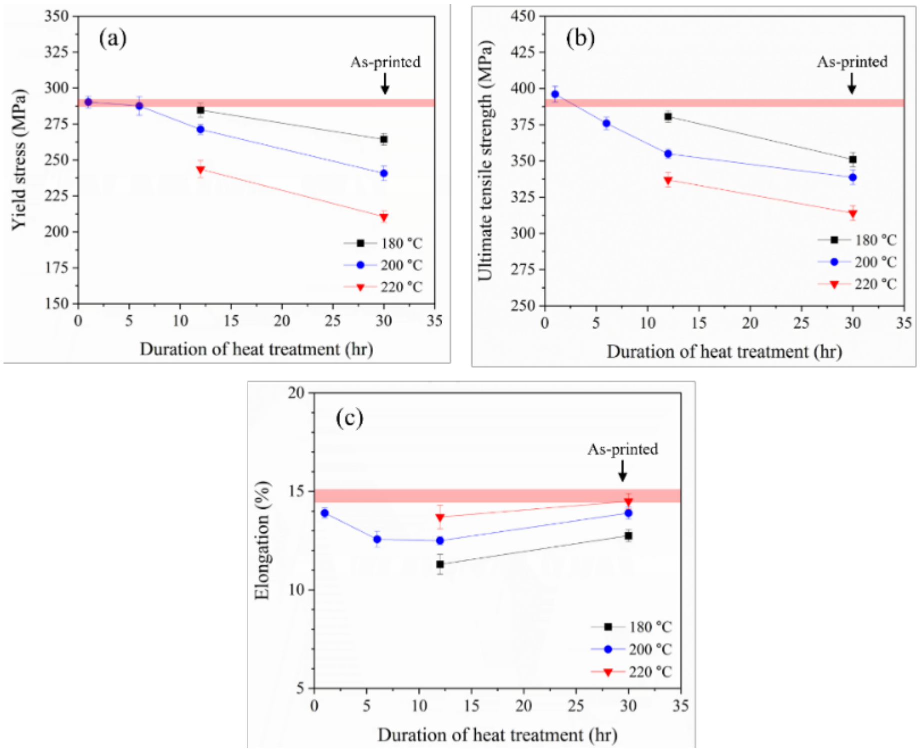

Figure 4-11 Effect of direct aging on mechanical properties of LPBF A20X including : (a) yield stress, (b) ultimate tensile strength (UTS), and (c) elongation at failure.

SEM micrographs from the fracture surfaces of as-built and heat-treated A20X alloy are demonstrated in Figure 4-12. All fracture surfaces in as-printed and direct-aged samples exhibited fine dimples, micro-voids and no cleavage facets, characteristic of the ductile failure mode. Further examination reveals that the dimple size did not change as a consequence of the direct aging (0.9-

1.2 μm). The micrometric size of the dimples corresponds to the micrometric size of the grains in both as-printed and aged alloy (see Figure 4-3). This supports the tensile results in Figure 4-7 and Figure 4-11, where the relatively high material elongation remained unchanged after exposure to direct aging.

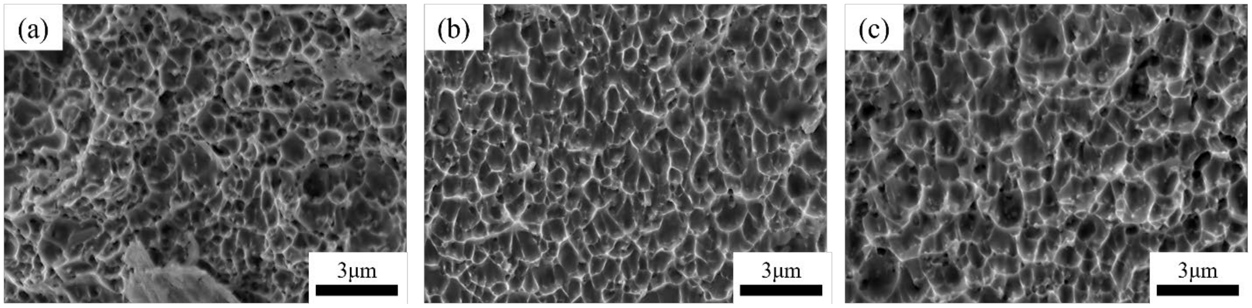

Figure 4-12 SEM images from fracture surface of A20X alloy upon tensile testing: (a) as-built; (b) direct-aged at 200 °C for 1 hr; (c) direct-aged at 200 °C for 30 hrs.

4.5 Conclusions

The influence of temperature and duration of direct aging treatment on mechanical properties and microstructure of LPBF A20X was studied through mechanical testing and electron microscopy. The following conclusions were drawn based on the experimental investigations:

1- The initial grain size (1.02 μm ±0.16) remained constant during direct aging. This observation is attributed to the Zenner pinning mechanism and the high density of precipitates accumulated along the grain boundaries during LPBF.

2- The initial microstructure exhibited incoherent Al_2Cu (θ) ($\{110\}_\theta \parallel \{220\}_{Al}$) dispersed in FCC aluminum matrix. During direct aging, θ precipitates coarsened and the volume fraction remained constant. The average precipitate size during direct aging increased by up to ~ 100%. No other metastable precipitate such as θ′ or Ω formed during direct aging, suggesting the absence of supersaturated matrix in as-printed A20X.

3- Direct aging of A20X LPBF caused material softening. Hardness decreased with temperature and time up to 23.7% of the initial material hardness. The yield strength and ultimate strength of the alloy experienced a maximum drop of 27% and 19.4%, respectively, after 220 °C for 30 hrs. This is due to precipitate coarsening during aging and the absence of metastable precipitates (θ′ and Ω).

4- Mg/Ag solute atom wall was observed at grain boundaries after LPBF processing. These atoms cause serrated plastic flow due to the locking of dislocations. Direct aging for longer durations promoted disintegration of the Mg/Ag wall into discrete clusters along the grain boundaries corresponding to reduction in serrated flow. For all aging temperatures used in this study, the serration disappeared after 12 hrs of heat treatment.

5- The as-printed material exhibited ductile fracture caused by the formation of small voids matching the average grain size. The first 12 hours of direct aging led to a decrease in ductility reaching 11.3%. After 12 hours, the ductility increased slightly. In all cases, the fracture mode remained ductile with dimples' size corresponding to the grain size.

CHAPTER 5 ARTICLE 2: EFFECT OF PRECIPITATION HARDENING ON THE MICROSTRUCTURE, MECHANICAL, AND CORROSION PROPERTIES OF ADDITIVELY MANUFACTURED A20X ALUMINUM ALLOY

H. Karimialavijeh, A. Chakraborty, M. Azzi, M. Proebstle, and E. Martin

Published in the journal of Materials science and engineering A on July 30th 2024

(https://doi.org/10.1016/j.msea.2024.147033)

5.1 Abstract

The effect of age hardening treatment on microstructure, tensile properties, and corrosion behavior of additively manufactured A20X alloy was investigated. Three single-step aging temperatures (150 °C, 175 °C, and 200 °C) and one double-step aging temperature (pre-aging at 165 °C followed by aging at 185 °C) along with varying heat treatment durations ranging from 30 minutes to 144 hours, were studied systematically. Microstructural characterizations revealed that the co-existence of coherent/semi-coherent (Ω, θ′) and incoherent precipitates (θ) resulted in the maximum hardening effect (up to 30% higher microhardness). This improved the yield strength at room and 150 °C by 33.4% and 22.6%, respectively. Double aging delivered the best combination of microstructure with fine grains and optimal precipitate assembly in a short duration (12-16 hrs). The heat-treated LPBF A20X showed higher ductility and similar mechanical properties compared to the cast A20X. However, optimal precipitate characteristics reduced the corrosion potential by 13-16% due to a higher galvanic reaction. The highest corrosion potential (-0.622 V) was achieved in the solutionized state.

Keywords: Laser powder bed fusion; aluminum alloy; A20X; Precipitation hardening; mechanical properties; corrosion properties

5.2 Introduction

Additive manufacturing (AM) enables the direct layer-by-layer construction of intricate geometries from computer-aided design (CAD) models. Laser powder bed fusion (LPBF) stands out as the predominant metal AM technology, proficient in processing a wide range of metallic alloys, including steels [156], magnesium [157,158], titanium alloys [159,160], nickel-based superalloys [161–166], and aluminum alloys [8,36,92,167,168]. However, LPBF process involve melting and rapid solidification, which can cause high residual stresses [169,170], and solidification cracking [171,172].

High-strength aluminum alloys with wide solidification ranges such as A6061 (70 °C [173,174]) and A7075 (97 °C [175]) are generally more susceptible to solidification cracking compared to alloys with narrow solidification ranges like AlSi10Mg (40 °C [176]) [177]. The mushy zones formed during solidification are torn apart by high thermal stresses caused by extreme cooling rates. As solidification progresses, these initial micro-cracks can expand into larger defects, compromising the structural integrity of the final component. Alloy modification through addition of elements like Zr, Ti and secondary particles such as TiC, ZrH_2, TiB_2, and LaB_6, promotes heterogeneous nucleation, reducing solidification cracking and ultimately enhancing laser processability [33,34,93,178,179].

The A20X alloy is a high-performance aluminum matrix composite (AMC) recently developed for LPBF. It incorporates TiB2 ceramic particles into an Al-Cu-Ag-Mg matrix to promote heterogeneous nucleation and reduce solidification cracking. Recently, Ghasri-Khouzani et al. [36] showed the LPBF processing window of A20X is wider by 650% and 275% compared to Al-Si-Mg alloys and 6061 alloys, respectively. The microstructure of LPBF A20X differs from typical LPBF aluminum alloys, as it is comprised of very fine grains (< 1µm) with random texture. A20X benefits from various strengthening mechanisms, including grain refinement through TiB2 particles, complex precipitation assembly, and solid solution hardening through alloying elements such as Cu, Mg, and Ag [123].

Solution heat treatment is not always required for LPBF aluminum alloys due to the super-saturated state caused by high cooling rates, as reported by Fiocchi et al. [20]. Direct aging has proven effective in strengthening some LPBF aluminum alloys such as AlSi10Mg [180] and A2024 [181]. However, Karimialavijeh et al. [182] recently investigated the direct aging possibility of LPBF A20X showing significant softening due to the highly over-aged state of the as-printed A20X.

Very few studies have investigated the effect of solutioning and aging treatments on the microstructure and mechanical properties of LPBF A20X. Avateffazeli et al. [56,112,183] investigated the effect of conventional age-hardening treatment on microstructure, tensile behavior, and fatigue properties of LPBF A20X, showing noticeable improvement in mechanical properties. Barode et al. [58] investigated the effect of solution treatment duration on mechanical properties of LPBF A20X. According to the authors, shorter solution treatment before aging eliminated the grain boundary cracks and improved the yield and tensile strengths by 30% and 22%, respectively, and retained ductility (10.6%). Jiang et al. [184] reported high ductility (11.6%) following T6 treatment.

All previous research reported a clear benefit of using a solution and aging treatment to improve the mechanical performance of LPBF A20X. However, previous investigations focused on the conventional heat treatment developed for cast A205. There is currently no comprehensive study in open literature evaluating the aging behavior, including aging curves at different temperatures, double-step aging, microstructural, and mechanical characterization of LPBF A20X. Given the significant difference between the microstructure of cast and LPBF A205, it is necessary to re-evaluate the heat treatment protocols to optimize the final mechanical properties. This new heat treatment requires to be optimized to deliver optimized high-temperature mechanical properties and corrosion resistance.

This study presents a systematic investigation of solution and aging treatment conditions on LPBF A20X microstructure, high-temperature tensile properties, and corrosion resistance. A comprehensive test matrix covering three different temperatures, a wide range of aging durations, and double-aging treatments was conducted. Advanced microscopic characterizations were performed to study precipitate evolutions at various stages of aging. The effect of precipitation on the corrosion properties of A20X was investigated using the potentiodynamic polarization test. Tensile testing was carried out at room (25 °C) and elevated temperature (150 °C) to examine the effect of precipitate and microstructure evolutions on mechanical properties.

5.3 Experimental procedure

5.3.1 Powder and LPBF process

Pre-alloyed A20X aluminum powder produced by gas atomization with spherical particles and a particle size range (D10-D90) of 15-53 µm was used. The chemical composition of LPBF-built A20X was measured using inductively coupled plasma optical emission spectroscopy (ICP-OES) and presented in Table 5.1. The trace gas (oxygen, nitrogen, and hydrogen) content of the printed components measured using LECO analysis is also given in Table 5.1. A Concept Laser M2 Series 5 LPBF printer was used to construct 100 mm tall cylindrical bars with 8 mm diameter, arranged on the steel build plate (without pre-heating) as illustrated in Figure 5-1 (a). All specimens were printed using the following laser scanning parameters: power 370 W, scan speed 1250 mm/s, hatch spacing 140 µm, beam diameter 175 µm, and powder layer thickness 40 µm. These values were previously optimized by Ghasri-Khouzani et al. [36] to ensure >99.5% final density . Nitrogen gas (≥99.9%) was continuously supplied into the build chamber during printing to maintain <0.1 % oxygen level.

Table 5.1. LPBF A20X chemical composition measured with ICP-OES and LECO analysis (wt. %).

Element (wt. %)	**Cu**	**Ti**	**B**	**Ag**	**Mg**	**Si**	**Fe**	**O**	**N**	**H**	**Al**
LPBF printed A20X	4.67	3.46	1.49	0.71	0.22	0.04	0.05	0.022	<0.001	<0.001	Bal.

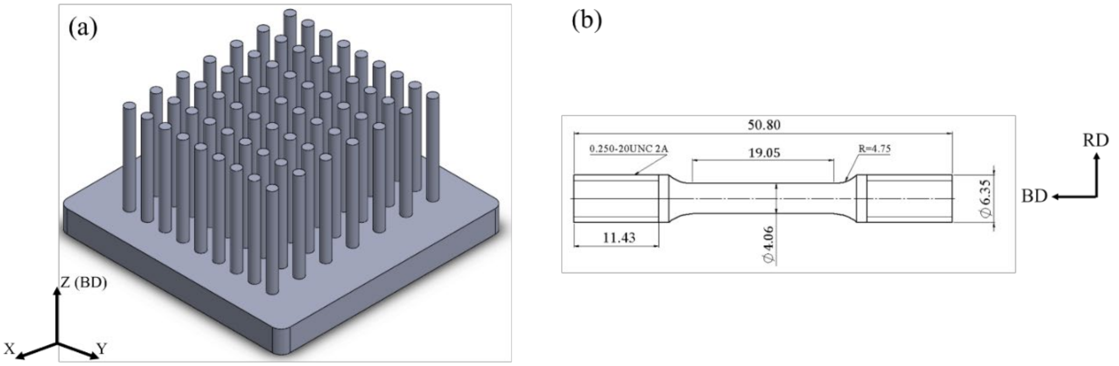

Figure 5-1 (a) Schematic illustration of the LPBF-built parts. (b) Geometry and dimensions of the tensile specimens used in this study. All dimensions are in mm. The build direction (BD) and radial direction (RD) of tensile bars are presented here.

5.3.2 Post-process heat treatment

Solution treatment of LPBF bars was conducted using a KSL-1200X furnace under an Argon atmosphere. The as-printed bars were heated to 520 °C at a heating rate of 5 °C/min. The samples were held at 520 °C for 2 hours to ensure a homogenous temperature suitable for both lab-scale and large-scale components. Specimens were immediately water-quenched after solution treatment. It was previously shown that full precipitate dissolution is achievable within 1 hr dwell time at temperatures above 505 °C [185].

Solutionized bars were subjected to two different types of aging treatments namely single- and double-aging. The specimens were immediately aged after solution treatment to avoid natural aging at room temperature. The aging temperatures were determined based on DSC analysis (not shown here) and the typical aging temperature used for LPBF Al-Cu alloys [20]. Single-aging treatments were performed at three temperature levels including 150 °C, 175°C, and 200 °C for various durations to create full aging curves. Double aging comprises two distinct stages: pre-aging and aging. Pre-aging allows homogenous nucleation of fine precipitates in the microstructure while subsequent aging at a higher temperature accelerates growth and minimizes heat treatment duration. The three single-step aging curves were leveraged to define the double aging temperatures. The pre-aging step was performed at 165 °C for 4 hrs. This temperature and time were selected to minimize the duration of treatment and create a microstructure containing fine coherent precipitates and intermediary phases including the Guinier–Preston zone and θ'' precipitates. The final aging temperature was set to 185 °C for different durations ranging between 2-16 hrs. This temperature offered a good combination of faster precipitation while maintaining the narrow precipitate spacing. All specimens were air-cooled after aging treatment.

5.3.3 Microstructural characterization

As-printed and heat-treated specimens were ground with SiC papers and polishing with diamond suspensions, followed by a 0.04 μm colloidal silica finish. A JEOL JSM-7600F field emission gun scanning electron microscope (FEG-SEM) was operated at an accelerating voltage of 5 kV and a working distance of 8 mm for microstructure characterization. The fractured and corroded surfaces were analyzed to identify failure and corrosion mechanisms after heat treatments.

A Thermo Scientific Quattro environmental SEM equipped with a Thermo Scientific Lumis electron back-scattered diffraction (EBSD) detector was used to investigate the effect of heat treatment on the grain size and crystallographic orientation distribution of LPBF A20X. An accelerating voltage of 20 kV was used for the EBSD analysis. Each EBSD scan covered an area of 2800 μm^2 to ensure at least 300 grains were included for each specimen, and a step size ranging between 90 and 200 nm was selected to ensure a ratio of 1/10 between the step size and the grain size. The data was further processed using TSL OIM™ software and a MATLAB script to generate inverse pole figure (IPF) maps. The kernel average misorientation (KAM) map was acquired from a region 300 μm below the fracture surface using a step size of 50 nm.

A JEOL JEM-2100F transmission electron microscope (TEM) equipped with an Oxford energy dispersive spectrometer (EDS) was utilized to study the evolution of nano-precipitates during aging. TEM and scanning TEM (STEM) analyses were conducted at an accelerating voltage of 190 kV. Cross-sectional slices (XZ surfaces) were prepared using standard metallographic grinding and polishing procedures on a Gatan disc grinder. Subsequently, a HITACHI FIB-2000A focused ion beam (FIB) was employed for the final thinning of the samples. The interparticle spacing was measured, as explained in [186,187].

5.3.4 Mechanical testing

Cylindrical specimens, 10 mm in length, were extracted from both as-built and heat-treated bars for hardness evaluation. Vickers micro-hardness testing was performed on polished specimens using an Akashi Mitutoyo MVK-HO tester, using a load of 1.96 N with a dwell time of 15 s. The average micro-hardness was calculated according to ASTM E92-17 [188] based on 10 indentations acquired within a 4 mm×4 mm square located at the center of each specimen.

Round tensile specimens, with 4.06 mm diameter and 19.05 mm gauge length, were machined from both as-printed and heat-treated cylindrical bars, as shown in Figure 5-1(b). Tensile testing at both room and elevated temperatures was performed using an MTS 810 machine at a crosshead speed of 19×10^{-4} mm.s^{-1}. MTS 632.13F-20 and MTS 632.53E-14 extensometers were used to measure elongation at room and elevated temperatures, respectively. For elevated temperature tensile tests, the samples were heated to 150 °C at 5 °C/min heating rate in a MTS 653.04 furnace. Specimens were held at the testing temperature for 30 minutes prior to test start. Three bars were tested for each condition to account for experimental variability.

5.3.5 Corrosion experiments

The corrosion testing was carried out at room temperature in an aerated 3.5% (0.61 mol/L) NaCl solution. A three-electrode type electrochemical cell was set up for the corrosion experiments where the tested specimen acted as the working electrode, a graphite rod served as the counter electrode (CE), and a Standard Calomel Electrode (SCE) was used as a reference electrode. A 1 cm diameter rubber O-ring was used to seal the specimen's exposed area of 0.79 cm^2. An Autolab potentiostat equipped with a frequency response analyzer was used to perform the electrochemical measurements. More details about the experimental setup can be found in another publication [189]. Initially, the specimen was immersed in the solution for 1 hour to achieve a stable open circuit potential (OCP). Subsequently, a potentiodynamic polarization experiment was conducted with a scanning rate of 10^{-3} V/s from a potential of -0.3 V up to 2 V relative to the OCP. The direction of the scan was reversed when either a current of 1 mA/cm^2 or potential of 2 V was achieved. The corrosion current density, I_{Cor}, was found using the Tafel interpolation technique, and the corroded area was analyzed using SEM to determine the corrosion mechanisms.

5.4 Results and discussion

5.4.1 As-printed microstructure

The as-printed A20X microstructure was characterized in planes perpendicular (XY) and parallel (XZ) to the build direction. In both cases, fully equiaxed grains with no indication of epitaxial grain growth were observed, as shown in Figure 5-2. The microstructure consisted of fine equiaxed grains with an average size of 1.09±0.16 μm and fine precipitates (< 200 nm) within intragranular regions and along the grain boundaries.

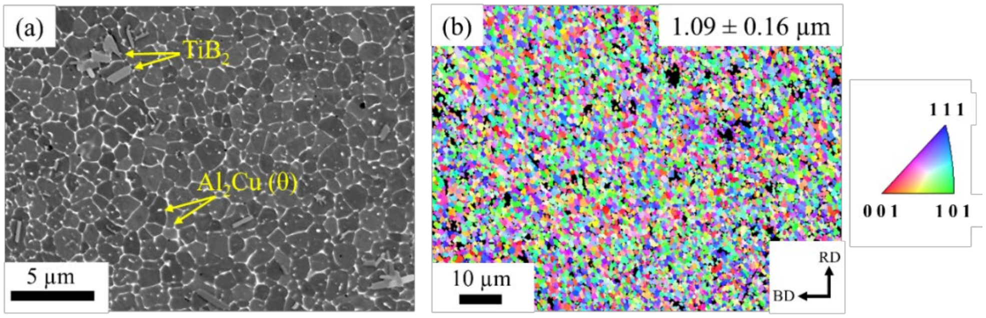

Figure 5-2. Microscopic characterization depicting the microstructure of as-printed A20X in a plane parallel to build direction: (a) SEM micrograph showing the equiaxed microstructure with Al_2Cu precipitates and TiB_2 particles, (b) EBSD-IPF map showing the random orientation of the grains with respect to build direction.

Sub-micron titanium diboride (TiB_2) particles were also evenly distributed in the microstructure in Figure 5-2 (a). These ceramic particles are incorporated into A20X to create a fully equiaxed grain structure and random texture, as shown in Figure 5-2 (b). The A20X alloy contains 4.5-5 wt.% of TiB_2 particles in its composition according to the X-ray diffraction analysis performed in a previous study [182]. This is 1.5X larger than the minimum weight fraction of TiB_2 required to prevent epitaxial growth in aluminum alloys [117].

Segregation of the alloying elements within the as-printed A20X was investigated using TEM-EDS analysis as shown in Figure 5-3. A solute-rich network containing Cu, Mg, and Ag was observed along the grain boundaries. The Mg/Ag-rich regions are solute clusters forming along grain boundaries due to solute rejection during solidification [182]. Copper is mostly found in the form of precipitates in combination with aluminum at inter- and intra-granular regions.

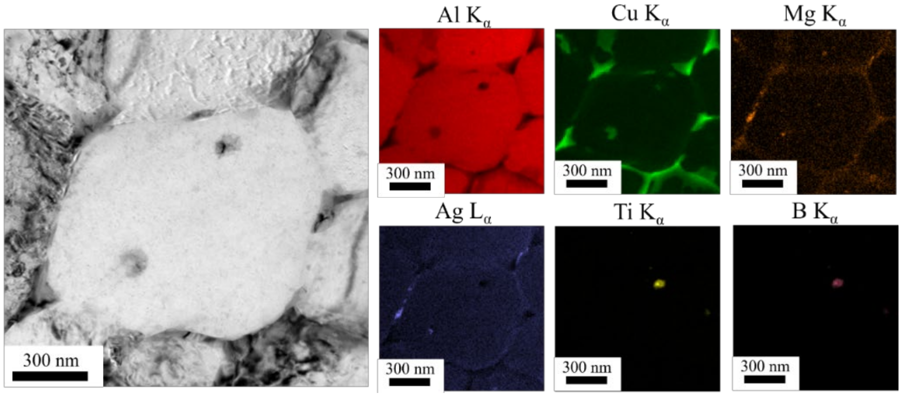

Figure 5-3. TEM-EDS map of the as-printed A20X showing a Cu-rich precipitate network along grain boundaries and segregation of Ag and Mg.

The precipitates within the as-printed A20X were studied using TEM, as shown in Figure 5-4. These precipitates were identified as incoherent Al_2Cu (θ) precipitates with an interplanar spacing of 4.29 A° forming along {220} FCC-α planes. Meta-stable inter-metallics such as θ′ and Ω precipitates were not observed confirming the over-aged state of as-printed A20X.

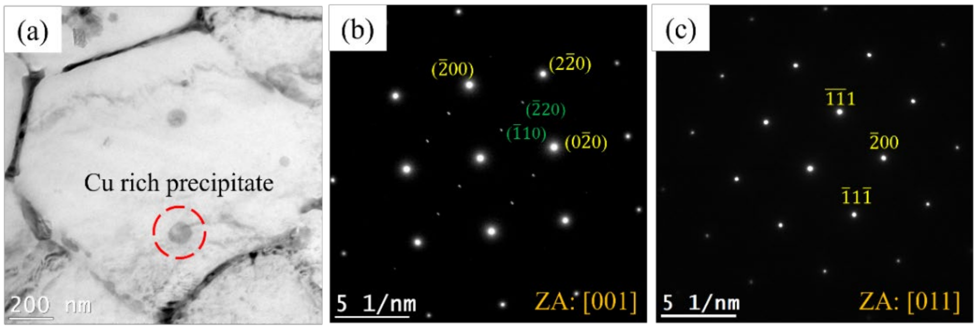

Figure 5-4. TEM analysis showing the precipitate type and habitat planes in as-printed A20X. (a) TEM bright field image showing intra-cellular and grain boundary precipitates, (b) selected area electron diffraction pattern from [001] and [011] zone axes showing the presence of stable θ and absence of meta-stable precipitates such as θ'.

5.4.2 Effect of heat treatment on the micro-hardness of LPBF A20X

The micro-hardness of LPBF A20X heat-treated at various temperatures for different durations is presented in Figure 5-5. In the as-printed condition, the material hardness was around 115-120 HV (Figure 5-5 (a)). After solution treatment, the hardness of the alloy increased to 130-132 HV. The increased hardness is attributed to the formation of a super-saturated solid solution and the promotion of solid solution hardening by solute atoms such as Cu and Mg, as explained by Liang et al. [190]. Upon aging, the hardness of the solutionized A20X initially increased up to a peak value followed by a gradual decrease over time. The peak hardness value for specimens aged at 150 °C was 155 ±1 HV. As the aging temperature increased, the peak hardness decreased slightly. For example, the peak hardness of the aging curve acquired at 200 °C was around 151±1 HV. Increasing the temperature also shortened the duration to reach peak hardness (increased hardening rate). For example, in the aging curve obtained at 150 °C, the peak hardness was achieved after ~60 hr. By increasing the aging temperature to 200 °C, this time reduced to 4 hr. (93% reduction) as shown in Figure 5-5 (a). The increased hardening rate is attributed to faster diffusion at higher temperatures resulting in faster precipitation of inter-metallic phases [191]. The behavior of the alloy in response to double aging was highly similar to single-step aging, as shown in Figure 5-5 (b). Due to the higher aging temperature used in double aging, the peak hardness (154±1 HV) was achieved after 8 hr.

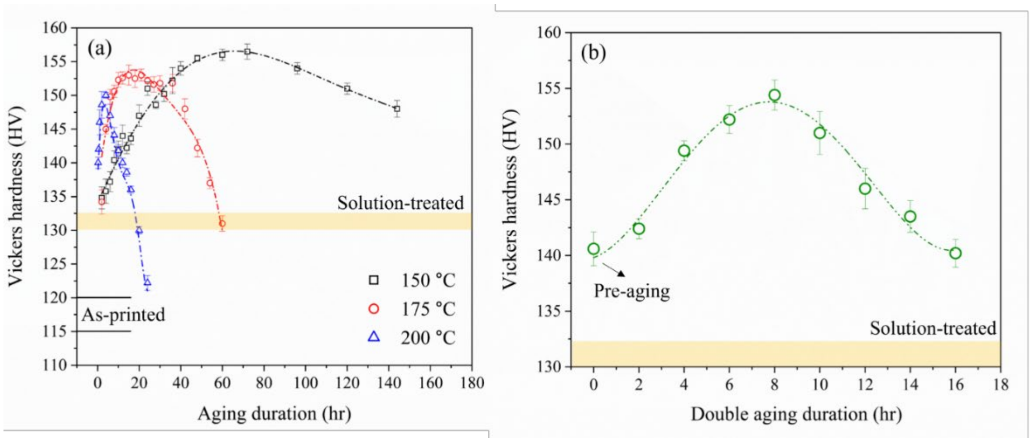

Figure 5-5. Aging curves show microhardness evolutions during the aging treatment as a function of temperature and duration of LPBF A20X. (a) Aging curves of single-aging treatment performed at three different temperatures including 150 °C,175 °C, and 200 °C, (b) Aging curve of double aging treatment including a pre-aging step (4 hr at 165 °C) followed by aging treatment at 185 °C for different durations.

5.4.3 Effect of heat treatment on the microstructure of LPBF A20X

To study the effect of aging on the A20X microstructure, one solutionized state at 520 °C for 2 hours followed by water quench (SHT) and three single-step aging conditions (A175-4, A175-24, and A175-48) corresponding to aging treatment at 175 °C for 4, 24, and 48 hr, respectively, were selected. The aging conditions correspond to the under-aged state (A175-4), peak hardness (A175-24), and over-aged state (A175-48) of the A20X alloy. One double aging condition (DA185-12) corresponding to a double aging at 165 °C for 4 hr. + at 185 °C for 12 hr was also selected for this analysis. The DA185-12 produced an overaged structure with a micro-hardness (142-145 HV) like the A175-48 condition. The two conditions correspond to the T7 temper of the alloy.

IPF maps of the representative heat-treated specimen are shown in Figure 5-6 (a-e). In all conditions, the alloy retained its equiaxed microstructure similar to the as-printed condition (Figure 5-2 (b)) and no sign of epitaxial grain growth was observed. However, all heat-treated specimens (Figure 5-6 (a-e)) exhibited grain growth compared to the as-printed condition. For example, the grain size of the solution-treated sample was ~3X times larger (2.92 ± 0.61 µm) than the as-printed grain size (1.09 ± 0.16 µm). Upon age hardening at 175 °C, the grain size remained relatively constant (~3 µm) up to 24 hours of heat treatment. However, after 48 hr. (A175-48), the grain size of the alloy grew by approximately 60% to 5.07 ± 0.47 µm. In this study, the maximum grain size of 6.07 ± 0.63 μm was obtained following aging at 150°C for 144 hours. The grain sizes in the near-peak-hardness state for the three aging temperatures were slightly higher than 3μm. The double-aging treatment (DA185-12) caused marginal grain coarsening compared to the as-solutionized microstructure (see Figure 5-6) and resulted in a much finer grain size than the single-step aging treatment (A175-48) even though both conditions show similar hardness (Figure 5-5).

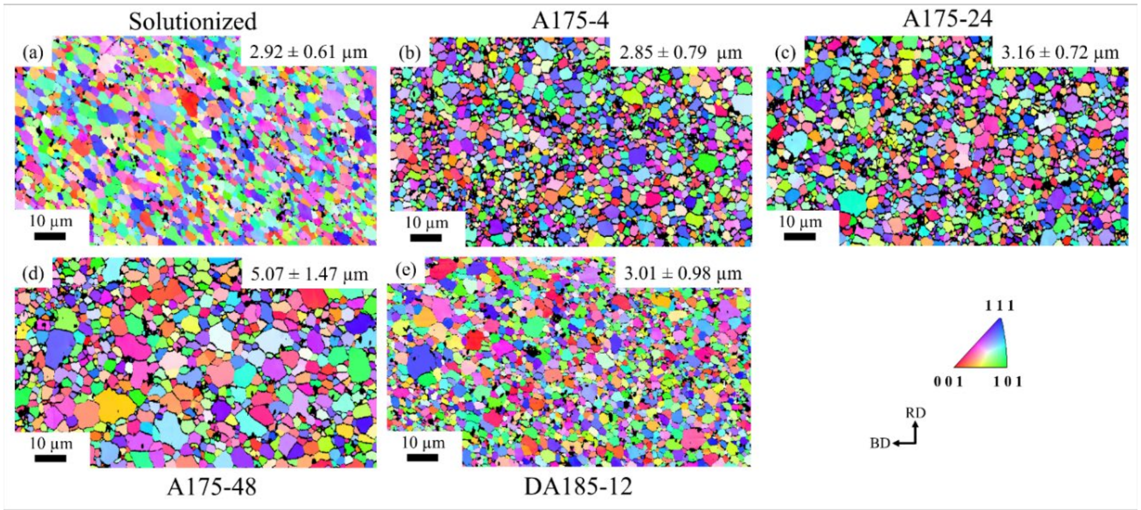

Figure 5-6. EBSD-IPF maps show the grain orientation (with respect to build direction) and size in different heat treatment states. (a) solution-treated (2 hr at 520 °C + water quench), (b) under-aged condition (aged at 175 °C for 4 hr), (c) peak-aged condition (aged at 175 °C for 24 hr), (d) over-aged condition (aged at 175 °C for 48 hr), (e) double-aged condition (165 °C for 4 hr + 185 °C for 12 hr).

The formation of precipitates during the heat treatments is shown in Figure 5-7. The continuous precipitate network observed along grain boundaries in the as-printed state (Figure 5-2) disappeared following solution treatment in Figure 5-7 (a). This proves the dissolution of precipitates within the matrix (super-saturated solution), as previously shown by Karimialavijeh et al. [185]. Small precipitates (~100-200 nm) can still be observed in Figure 5-7 (a). These precipitates remain undissolved during solution treatment or are formed during quenching, as discussed in [192].

Upon aging at 175 °C, fine discrete inter-metallics began to form in intra-and inter-granular regions, as shown in Figure 5-7 (b-e). As the aging treatment duration increased in Figure 5-7, the grain boundary precipitates became coarser. The microstructures of T7-A20X (stabilized) resulting from A175-48 and DA185-12 are presented in Figure 5-7 (d,e). In both cases, similar volume fraction of precipitates and TiB_2 particles are observed. These particles act as pinning agents limiting grain growth through the Zenner pinning mechanism [193]. This indicates that A20X grain size is mainly governed by heat treatment duration as previously shown by Rhines et al. [194].

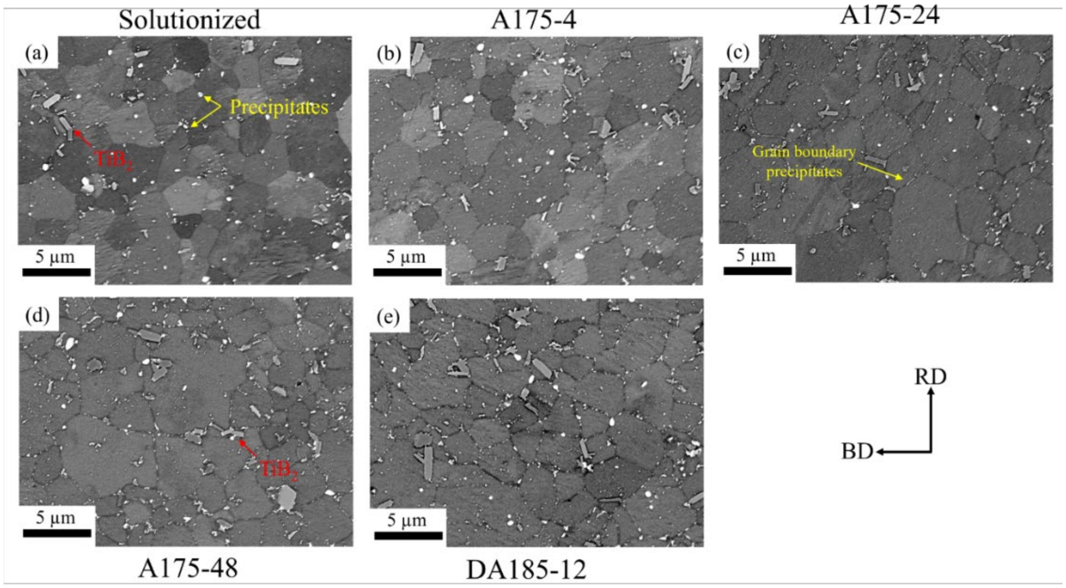

Figure 5-7. SEM back-scattered electron (BSE) micrographs showing the microstructure of LPBF A20X in different heat treatment states. (a) solution-treated (2 hr at 520 °C + water quench), (b) under-aged condition (aged at 175 °C for 4 hr), (c) peak-aged condition (aged at 175 °C for 24 hr), (d) single-aged condition (aged at 175 °C for 48 hr), (e) double-aged condition (165 °C for 4 hr + 185 °C for 12 hr).

Further precipitate characteristics at various stages of heat treatment were investigated using TEM analysis. Selected area electron diffraction (SAED) patterns and bright-field images showing representative specimens in [001] and [011] zone axis are presented in Figure 5-8 (a-p). The microstructure of LPBF A20X in the early stages of aging (A175-4) is presented in Figure 5-8 (a-d). Fine disk-shaped intermetallics with a dense distribution were observed along the $\{200\}_\alpha$ planes (indexed in yellow). This coherent metastable precipitate known as θ''/θ' forms upon the transformation of the Guinier–Preston zone during age hardening treatment, as explained by Takeda et al. [195].

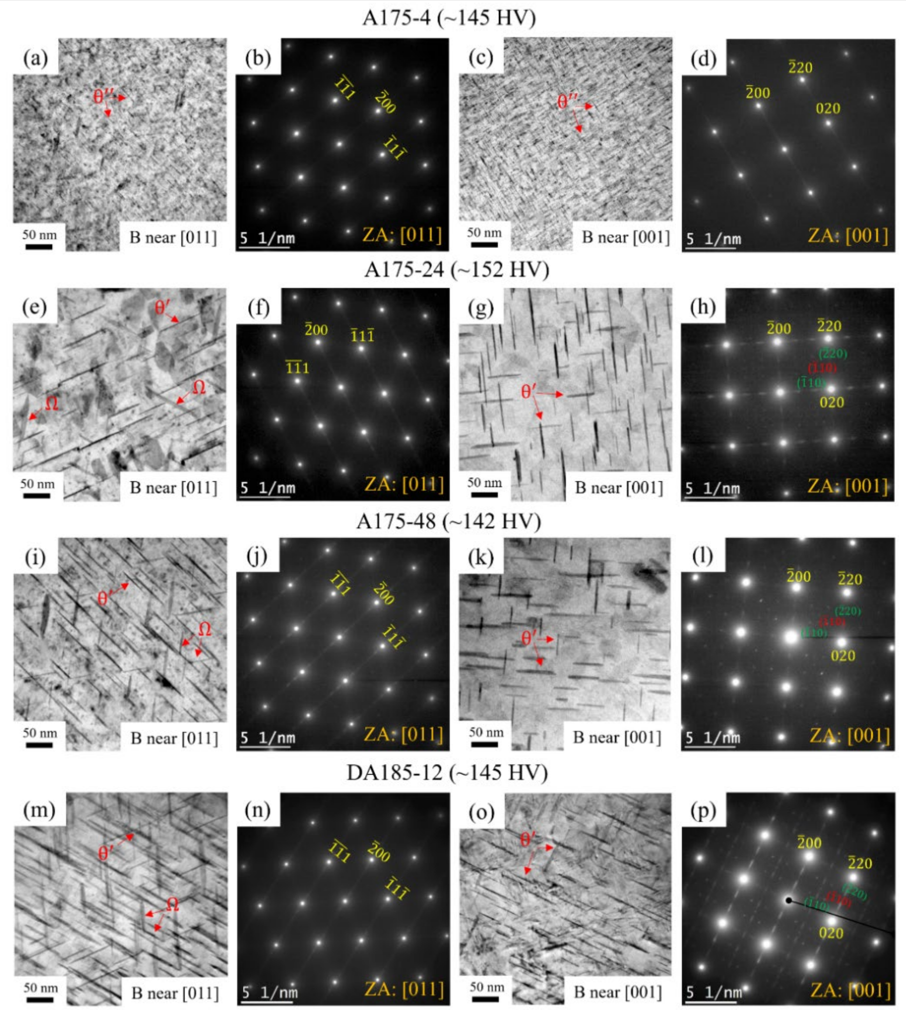

Figure 5-8. Bright-field TEM images along with their respective SAED patterns for LPBF A20X at different stages of age hardening treatment. (a) under-aged condition (aged at 175 °C for 4 hr), (c) peak-aged condition (aged at 175 °C for 24 hr), (d) single-aged condition (aged at 175 °C for 48 hr), (e) double-aged condition (165 °C for 4 hr + 185 °C for 12 hr). Yellow, red, and green indexes show the aluminum matrix, θ', and θ precipitates.

The microstructure of the A20X after 24 hr. of heat treatment at 175 °C (peak hardness) is shown in Figure 5-8 (e-h). The precipitates were coarser and sparsely distributed in comparison to the early stages of the heat treatment (Figure 5-8 (a-d)). Semi-coherent θ' precipitates were observed along $\{200\}_{\alpha}$ and $\{220\}_{\alpha}$ planes (indexed in red), as shown in Figure 5-8 (e-h). The inter-planar spacing of θ′ along {110} plane was around 0.286 nm, similar to values reported in the literature [196,197]. The diffraction spots indexed in green in Figure 5-8 (h) correspond to the non-coherent θ precipitates ($\{110\}_{\theta} \parallel \{220\}_{\alpha}$). Furthermore, coherent orthorhombic Ω precipitates

($\{001\}_{\Omega} \parallel \{111\}_{\alpha}$) were visible after 24 hr aging in Figure 5-8 (e,f). The formation of Ω on the FCC principal gliding plane ($\{111\}_{\alpha}$) is attributed to the presence of silver in Al-Cu-Mg-Ag alloys with high Cu: Mg ratio [198]. This is known to improve mechanical properties at elevated temperatures due to their coarsening resistance [39,66,198]. The co-existence of coherent Ω and non-coherent θ'/θ precipitates is known to maximize the hardness of the alloy through coherency strain hardening and Orowan hardening, as explained by Gladman [199].

As the aging duration increased to 48 hr., the precipitates began to transform from coherent into incoherent, as shown in Figure 5-8 (i-l). The relative fraction of Ω precipitates (Figure 5-8 (i)) increased compared to the peak hardness condition (A175-24). Moreover, the brighter green-indexed diffraction spots in Figure 5-8 (l) show higher fraction of incoherent θ precipitates resulting from over-aging. The increased fraction of coarse non-shearable particles facilitates dislocation motion resulting in lower hardness after 48 hr. in Figure 5-5 (a).

The bright-field TEM images and SAEDs corresponding to the double-aged specimen are presented in Figure 5-8 (m-p). Upon double-aging, the distance between the observed precipitates (Ω, θ′) becomes smaller compared to the single-aged specimen (A175-48), as shown in Figure 5-8 (mm). According to Werenskiold et al. [200], increasing the aging temperature reduces the threshold for precipitate dissolution. This means that precipitates exceeding the threshold size can grow at the expense of fine precipitates nucleated at the beginning of aging. In this case, pre-aging carried out at a lower temperature (165 °C) stabilizes fine precipitates that can be rapidly grown upon subsequent aging at a higher temperature. The combination of tighter precipitate spacing and finer grain size (due to shorter heat treatment) in double-aged A20X is expected to improve the mechanical properties compared to single-aging.

Figure 5-9 shows the elemental distribution in the two main precipitates (Ω,θ′) observed in age-hardened A20X. Both precipitates are rich in copper, as shown in Figure 5-9 (c,h). This aligns with previous reports on similar nominal composition (Al_2Cu) of these precipitates [201,202]. At the Ω-α interface, a thin layer enriched with silver (Ag) and magnesium (Mg) was observed (Figure 5-9 (d, e)). This was not observed in the θ' precipitate shown in Figure 5-9 (f-j). The Ag-Mg rich layer could be the remains of a precursor phase (Ag-Mg cluster) formed within minutes of aging start [202]. Upon further aging, the Cu atoms migrate towards Ag-Mg clusters resulting in the formation of Ω precipitates [201].

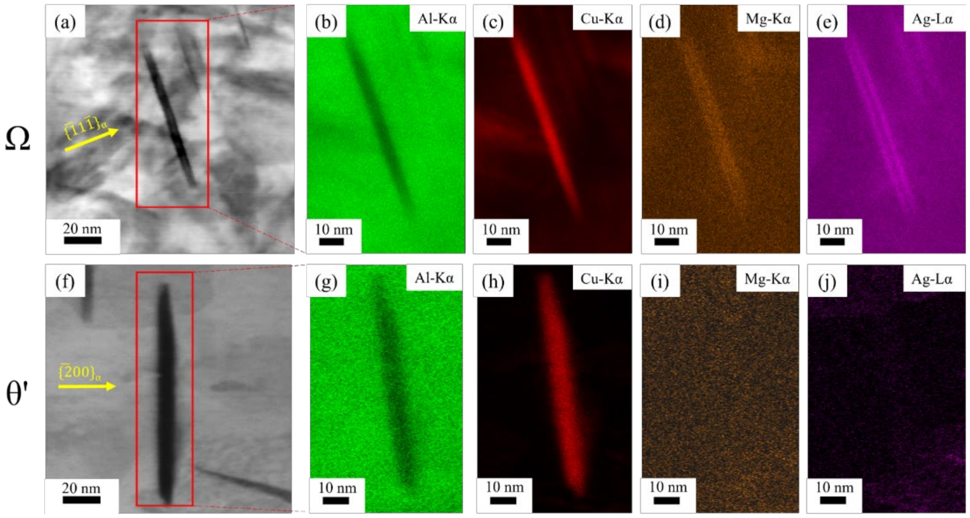

Figure 5-9. TEM-EDS map showing elemental distribution in different precipitates observed in age-hardened A20X. (a) Ω precipitates along the $\{111\}_\alpha$ planes, (b) θ' precipitates along the $\{200\}_\alpha$ planes.

5.4.4 Effect of heat treatment on stress-strain curves of LPBF A20X

The effect of heat treatment on the stress-strain curves of LPBF A20X at room temperature is shown in Figure 5-10 (a). The as-printed state exhibited the lowest flow stress followed by the solutionized state. In both cases, the yield point phenomenon (or discontinuous yielding) was observed. This phenomenon is characterized by a drop in the stress-strain curve at the onset of plastic deformation followed by a stress plateau [58,203]. The yield point phenomenon is commonly attributed to the locking of dislocations by Cottrell atmospheres formed around solute atoms such as Mg at the onset of plastic deformation [204,205]. Upon reaching the transition point, uniform plastic deformation begins, and stress gradually increases due to strain hardening. The critical strain associated with the transition point was 3% for the as-printed material and 1% for the as-solution-treated material. This reduction in critical strain coincides with the dissolution of the Mg solute wall observed in the as-printed material (see Figure 5-3) during solution heat treatment.

The serrated plastic flow was also observed in the as-printed A20X, as shown in Figure 5-10 (a). Serrated plastic flow, also known as the Portevin-Le Chatelier (PLC) effect, has been associated with the continuous locking and unlocking of dislocations by Mg solute atoms [182]. Interestingly, this behavior was not observed in the solutionized A20X where the matrix was enriched with Mg atoms. This is likely due to significantly lower dislocation density (≤50%) compared to the as-printed state recently reported by Barode et al. [58]. According to He et al. [131], the absence of the Mg solute wall along grain boundaries following heat treatment combined with lower dislocation density reduces the possibility of solute/dislocation interaction, limiting the PLC effect.

Upon aging, the flow stress of the alloy increased at the expense of ductility. Moreover, yield point phenomenon and serration were not observed in the aged specimen due to the absorption of solute atoms by precipitates. This is shown in Figure 9, where the presence of Mg at the **Ω**-α interface is apparent in the aged conditions. The disappearance of the discontinuous flow behavior following the disappearance of the Mg-rich solute wall in LPBF A20X has also been reported in [182].

The effect of heat treatment on the stress-strain curves of LPBF A20X at 150 °C is shown in Figure 5-10 (b). At 150 °C, all heat treatment states exhibited lower tensile flow stress compared to 25 °C. At elevated temperatures, the thermal energy provides an extra driving force for dislocations to overcome the Peierls-Nabarro stress, lowering the yield strength [206,207]. Thermal healing of dislocations limits the material's ability to generate and sustain dislocations, lowering the UTS of the material and increasing the ductility [208] . Increasing the testing temperature from 25 °C to 150 °C resulted in the disappearance of serrations. In this case, the high dislocation annihilation rate dominates over the increased dislocation pinning effect (due to higher diffusion rate), resulting in the elimination of serrated plastic fellow, as shown in Figure 5-10 (b). Aging affected the tensile flow similarly at both 150°C and room temperature. The tensile properties including yield strength, tensile strength, and elongation will be further discussed in section 5.6.

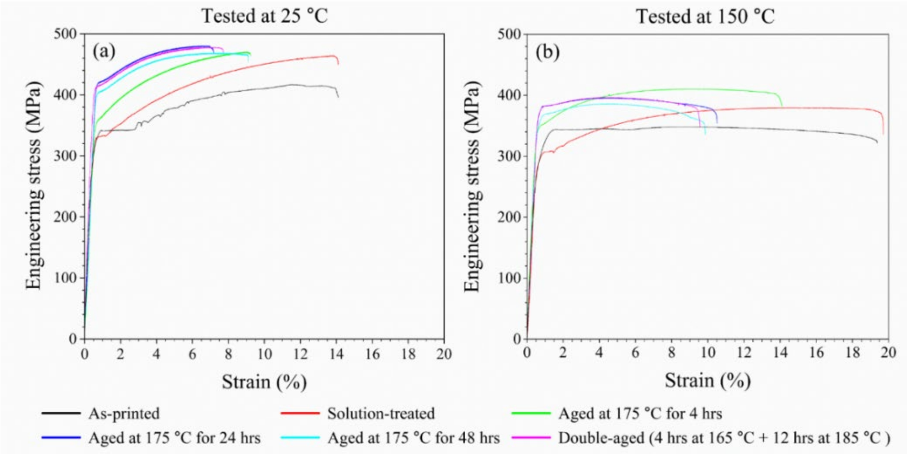

Figure 5-10. Effect of heat treatment on tensile flow of A20X at: (a) room temperature (25 °C), (b) high temperature (150 °C).

5.4.4.1 Effect of heat treatment on strain hardening rate

Two different strain hardening behaviors are observed in Figure 5-10. This is illustrated in Figure 5-11, where the work hardening rate (within the plastic region) is plotted as a function of the true strain. The as-printed and solutionized conditions exhibit a low work hardening rate at lower strains corresponding to the yield point plateau. This is followed by a sudden increase in the work hardening rate (first peak) as the material transitions into a more uniform plastic deformation regime. Serrations in the as-printed material result in large local variations in the work hardening rate in Figure 5-11. Despite these fluctuations, both, the as-printed and solutionized materials, show similar work hardening rates decreasing with true strain. On the one hand, the high strain hardening rate of the as-printed material can be explained by the combination of small grain size (~1 μm) and serrated plastic flow. On the other hand, the solutionized and, to some extent, under-aged (like A175-4) conditions are in a super-saturated state. The combination of plastic deformation and the presence of pre-existing GPZs and θ'' shown in Figure 5-8 (a-d) can facilitate the heterogeneous precipitation and growth of secondary phases, as explained in [209]. This increases the material's capacity to hinder dislocation mobility promoting higher work hardening [209–212].

Increasing the aging time and temperature reduces the strain-hardening rate in Figure 5-10. This is illustrated for the DA185-12 condition in Figure 5-11. In this case, the strain hardening rate follows a more conventional behavior where strain hardening decreases progressively between the yield and UTS points. This can be attributed to the high precipitate volume fraction observed in Figure 5-8 (e-p). The abundance of precipitates depletes the matrix of precipitate-forming elements, such as Cu, Mg, and Ag. This restricts precipitation during plastic deformation, reducing the strain hardening, as explained in [213].

All presented conditions exhibited lower work hardening rates with less instabilities at 150 °C compared to those tested at room temperature (Figure 5-11). Plastic deformation at elevated temperatures coincides with increased dislocation annihilation (recovery rate), which reduces the dislocation/dislocation and dislocation/precipitate interaction [214]. This lowers the strain-hardening capacity of the LPBF A20X at elevated temperatures.

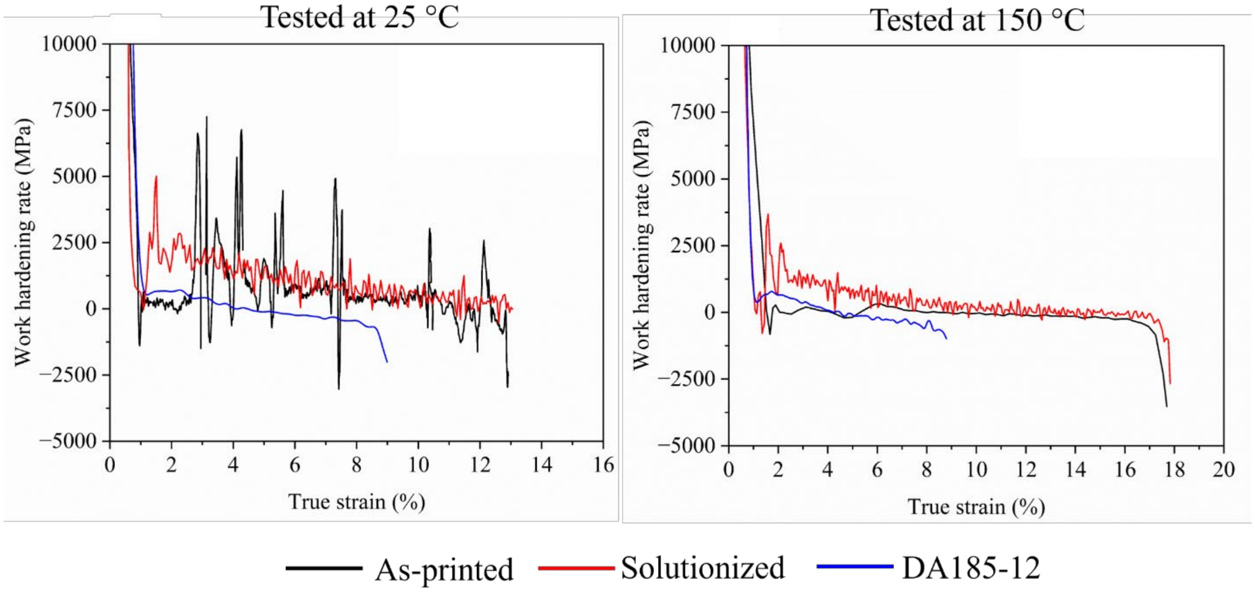

Figure 5-11. Work hardening rate as a function of true strain for as-printed, solutionized, and DA185-12 conditions tested at : (a) 25 °C, (b) 150°C.

5.4.5 Effect of heat treatment on the tensile properties of LPBF A20X

The effect of heat treatment on the yield strength of A20X is presented in Figure 5-12 (a). The yield strength follows a similar trend for the two testing temperatures with lower values observed at 150 °C. The yield strength of solutionized A20X increases slightly relative to its as-printed counterpart (from 315±2.6 to 325.5 ± 3.8 MPa at room temperature) despite ~3X larger grain size (see Figure 5-6). This is because the dissolution of precipitates promotes solid solution strengthening, consequently pinning dislocations and delaying the onset of plastic deformation.

Upon aging, yield strength gradually increases and peaks at 420.36 ± 3.4 MPa (A175-24). This is in agreement with the TEM micrographs shown in Figure 5-8, where the fine coherent intermetallics observed at the beginning of aging evolve into semi-coherent (θ') and incoherent (θ) particles. These precipitates maximize the dislocation pinning effect in the A175-24 (maximum hardness) condition. Upon over-aging, the yield strength decreases to 404.6 ± 4.7 and 414.5 ± 2.9 MPa for A175-48 and DA185-12 conditions in Figure 5-12 (a), respectively. This is attributed to the transition from semi- to non-coherent ($\theta' \rightarrow \theta$) precipitates, as shown in Figure 5-8. Moreover, the wider spacing of θ particles facilitates easier dislocation movement resulting in lower yield strength, as explained in [199]. The higher yield strength of double-aged A20X in Figure 5-12 (a) is due to finer precipitate spacing and grain size observed in Figure 5-6 and Figure 5-8.

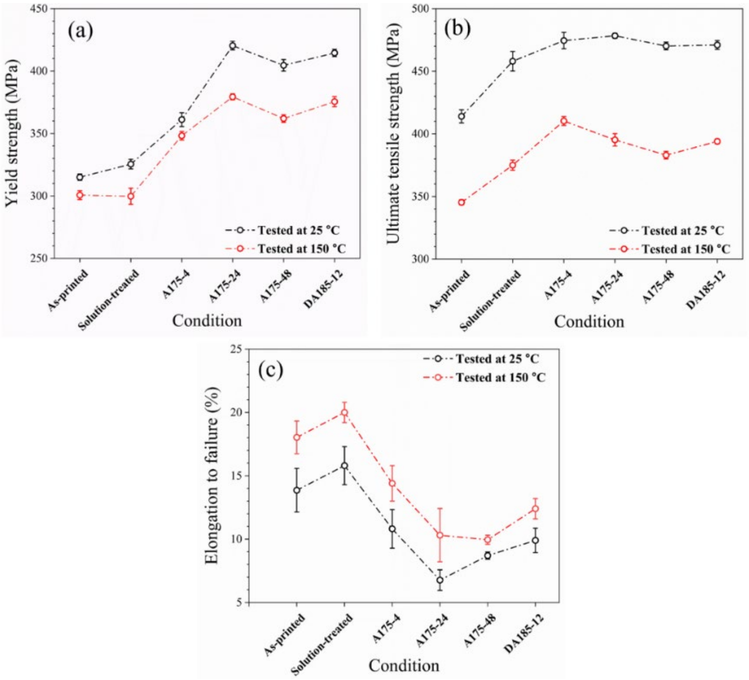

Figure 5-12. Effect of heat treatment on room and high-temperature tensile properties of LPBF A20X. (a) yield strength (YS), (b) ultimate tensile strength (UTS), (c) elongation at failure.

To better understand the strengthening mechanisms during aging, the yield strengths of LPBF A20X aged at 175 °C (4, 24, and 48 hr) and DA185-12 are plotted as functions of precipitate spacing (blue curve) and grain size (red curve) in Figure 5-13. As the aging time increases from 4 to 24 hours, the yield strength increases by 59 MPa, while the grain size increases by 0.31 μm. This minor change in grain size cannot account for the significant increase in yield strength. Furthermore, this relationship between grain size and yield strength contradicts the Hall-Petch law

[215]. The precipitate size and spacing of heat-treatable aluminum alloys usually have a stronger effect on the mechanical properties when compared with the grain size [216–218]. The A175-4 condition in Figure 5-13 has the lowest yield strength and smallest precipitate spacing among all the aged conditions. This can be due to the small size and volume fraction of precipitates shown in Figure 5-8 (a,c). The maximum yield strength is achieved when the precipitate spacing is approximately 39 nm. This corresponds to the best combination of shearable and non-shearable particles shown in Figure 5-8 (e,g). Increasing the particle spacing (and thus particle size) above a critical value always leads to a reduction of the mechanical properties in precipitate-hardened metals [219], as observed for the A175-48 condition in Figure 13.

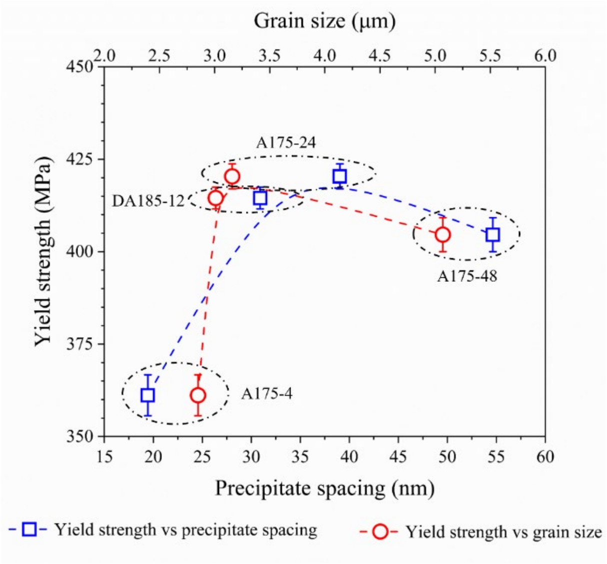

Figure 5-13. Room temperature yield strength of specimens aged at 175°C and double-aged specimens as a function of interparticle spacing (blue curve) and grain size (red curve).

The UTS at room temperature increases by approximately 11% from 414 ± 5.3 MPa to 458 ± 7.8 MPa after solution treatment, as presented in Figure 5-12 (b). After aging for 4 hr, the UTS increases to 474.5 ± 6.5 MPa and remains relatively unchanged thereafter. Lower tensile strength at 150°C is attributed to the lower strain hardening due to thermal recovery shown in Figure 5-11. The UTS reaches a peak value of 410.3 ± 3.5 MPa in the under-aged state (A175-4) in Figure 5-12 (b) and decreases gradually with longer aging durations. This behavior can be due to deformation-assisted precipitation more prevalent in the under-aged condition (A175-4) tested at high temperature [210]. The DA185-12 condition produced higher UTS (391 MPa at 150°C) compared to the A175-48 condition (384 MPa at 150°C), as shown in Figure 5-12 (b). This is due to a combination of finer grain size and lower inter-particle spacing as shown in Figure 5-6 and Figure 5-8.

The uniform elongation in Figure 5-12 (c) is slightly higher at room temperature when compared to the material tested at 150 °C. This can be attributed to the higher strain hardening rate at room temperature, delaying the plastic instability and increasing the uniform elongation of the material. Solution-treated A20X exhibited the highest ductility (14.71 ± 0.91% and 13.38 ± 0.79% at RT and 150 °C). The absence of precipitates along with high strain hardening rate defers the plastic instability increasing the material ductility [213]. After aging treatment, the uniform elongation gradually decreases to the minimum value of 6.44 ± 0.82% in the peak-aged condition (A175-24). This can be explained by the reduction of the strain-hardening rate shown in Figure 5-11 and the formation of secondary phases as shown in Figure 5-8, as previously shown in [220,221].

Fracture surfaces of single-aged (A175-48) and double-aged (DA185-12) specimens tested at room temperature (25 °C) and 150 °C are presented in Figure 5-14. Typical ductile fracture features including shallow dimples with sizes comparable to the grains are observed in all conditions. However, the dimple size is larger for specimens tested at 150 °C, as shown in Figure 5-14. This is attributed to the higher post-uniform elongation at elevated temperatures (see in Figure 5-10) delaying the void coalescence and final rupture. Moreover, secondary particles such as precipitates and TiB_2 particles were observed at the bottom of the dimples in all conditions (yellow arrows in Figure 5-14). Significant strength mismatch between the aluminum matrix and secondary particles results in plastic instability at the matrix/secondary particle interface followed by localized plastic deformation [213,222]. Strain localization results in void formation around these particles leading to failure. This is observed in Figure 5-15 where a kernel average misorientation (KAM) map of the DA185-12 specimen tested at room temperature is presented. Higher average misorientation values near grain boundaries and TiB_2 particles suggest dislocation accumulation, which leads to void initiation and eventual fracture during later stages of deformation.

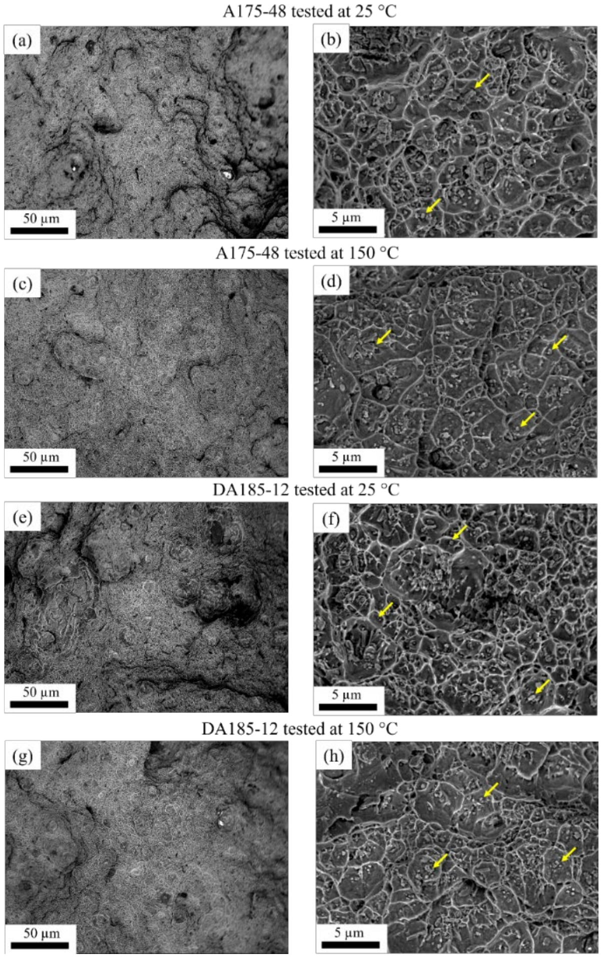

Figure 5-14. SEM micrographs showing fracture morphology in tested specimens: (a) Single-aged (A175-48) tested at 25 °C, (b) Single-aged (A175-48) tested at 150 °C, (c) double-aged tested at 25 °C, (d) double-aged tested at 150 °C.

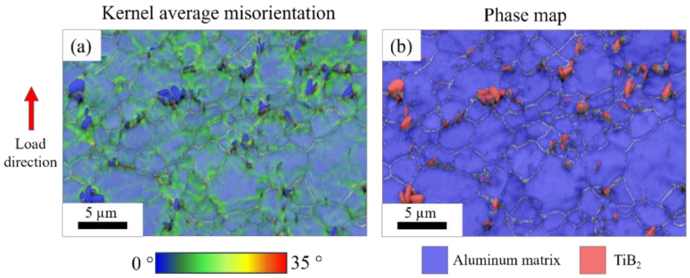

Figure 5-15. EBSD micrographs acquired from a region beneath the fracture surface of DA185-12 tested at room temperature, (a) kernel average misorientation (KAM) map, (b) phase map showing Al matrix and TiB_2 particles.

The yield strength and elongation of T7-A20X in comparison to common LPBF aluminum alloys are presented in Figure 5-16. In general, the enhancement in strength inevitably comes at the expense of ductility and vice versa. For example, Al-Zn-Mg alloys have good strength and poor ductility while Al-Si-Mg alloys have poor strength and good ductility. Recently developed LPBF aluminum alloys such as A20X and Scalmalloy offer superior strength and ductility compared to conventional aluminum alloys. Furthermore, A20X benefits from a processing window allowing ≥ 99% relative density at lower energy densities (40-120 J/mm^3) compared to Scalmalloy (175-300 J/mm^3) [36,223]. This allows for a higher production rate reducing the operation costs and energy consumption.

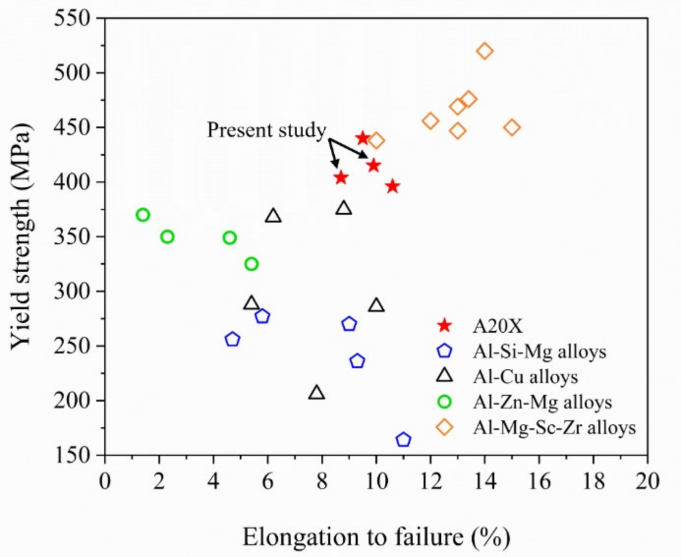

Figure 5-16. Yield and tensile strength of various aluminum alloys fabricated using LPBF acquired from the literature [20,56,58,178,224,225]. All the presented data are from alloys in the T6 and T7 states.

A20X alloy can also be fabricated by casting. For example, Avateffazeli et al. [56] reported yield and tensile strengths of 440 MPa and 500 MPa, respectively, for T7-cast A20X. In this study, the yield and tensile strengths of 415 MPa and 475 MPa, respectively, were achieved after the double-aging treatment (DA185-12). This similarity is because the tensile properties of these alloys are mainly influenced by the size and volume fraction of Cu-rich precipitates controlled by the chemical composition and post-heat treatment [216–218]. However, the LPBF A20X exhibits a significantly higher elongation to failure (~8-10%) compared to cast A20X (~ 4%) [56]. This can be attributed to the finer grain size and random crystallographic orientation in LPBF A20X (1-5 µm) compared to the textured and coarse grain structure (48 µm in [56]) of cast A20X.

5.4.6 Effect of heat treatment on the corrosion properties of LPBF A20X

The corrosion properties in different states were evaluated to determine the effect of microstructural evolutions resulting from heat treatment on the electrochemical behavior of LPBF A20X. Polarization curves for various heat-treatment states and their corresponding corrosion parameters are shown in Figure 5-17 and Table 5.2, respectively. The observed corrosion potential (-0.710 V_{SCE}) and current density (1.05×10^{-8} A·cm^{-2}) for the as-printed condition in Table 5.2 are similar to values reported in the literature [226]. After solution treatment (green curve in Figure 5-17), the corrosion potential increases to -0.622 V_{SCE} suggesting transition to a more noble state compared to the as-printed condition. This is attributed to the higher amount of copper in the matrix, known to ennoble aluminum alloys [227–231]. The higher current density of the solutionized state (4.14×10^{-7} A.cm^{-2}) indicates a higher corrosion rate.

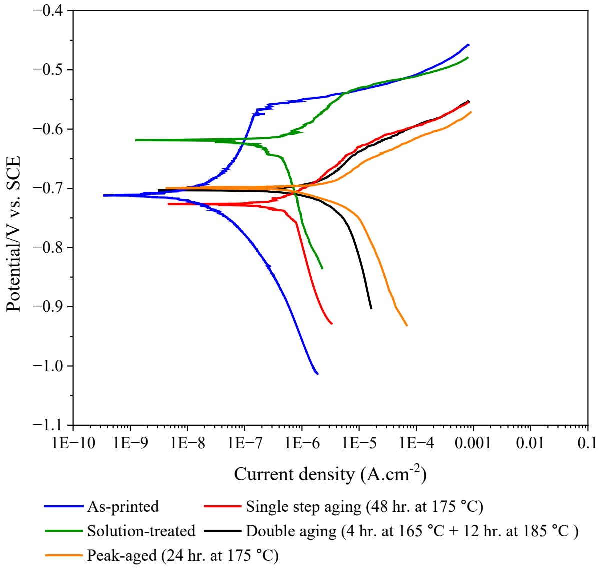

Figure 5-17. Polarization curves showing the effect of heat treatment on corrosion behavior of LPBF-A20X.

The corroded surface morphology was investigated to assess the role of solute redistribution on the corrosion properties of A20X. Figure 5-18 (a, b) shows the corroded surface morphology of as-printed A20X where the continuous network of solute-rich precipitates remains intact in the as-printed A20X, while the matrix is preferentially corroded. As-printed A20X is already in the over-aged state (Figure 5-18 (a, b)) meaning that the matrix is depleted of solute atoms such as copper, as shown previously in [36,92,182]. Accordingly, the higher electrochemical potential of Al_2Cu precipitates (-0.695 V_{SCE}) compared to the aluminum matrix (-0.744 to -0.8548 V_{SCE}) measured in Table 5.2 leads to a galvanic reaction followed by accelerated corrosion of the matrix, as explained in [232–234].

Table 5.2. Corrosion parameters acquired from polarization curves.

Specimens	I_{Cor} (A.cm^{-2})	E_{Cor} (V)	E_{Pitt} (V)
As-printed	1.05×10^{-8}	-0.710	-0.563
Solution-treated	4.14×10^{-7}	-0.622	-0.537
A175-24	1.07×10^{-6}	-0.699	-0.653
A175-48	6.11×10^{-7}	-0.723	-0.622
D185-12	1.18×10^{-6}	-0.704	-0.626

The corrosion morphology of solution-treated A20X is presented in Figure 5-18 (c, d). Unlike the as-printed condition, intergranular corrosion is evident and few signs of intragranular corrosion are observed. The formation of intermetallics (θ' and θ'') along grain boundaries during quenching (Figure 5-7 (b)) promotes the absorption of solute atoms dissolved in the matrix. This results in the appearance of narrow solute-depleted zones near the grain boundaries. Solute-depleted zones have lower corrosion potential (anodic region) compared to the internal body of α-grains (with higher copper content) and grain boundary precipitates [235]. Accordingly, the lower corrosion potential (-0.622 V) measured in the solutionized state in Table 5.2 results in an anodic reaction promoting corrosion of the solute-depleted zone.

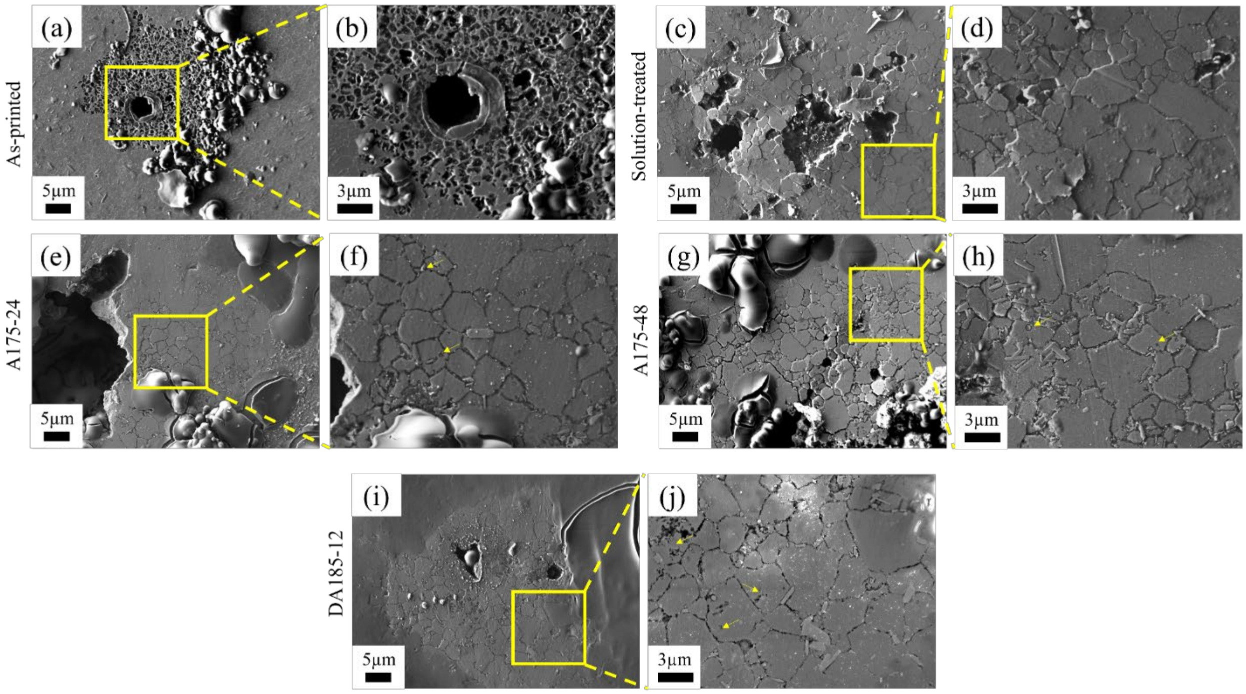

Figure 5-18. Corrosion morphology of LPBF A20X after polarization test in 3.5% NaCl solution. (a,b) as-printed, (c,d) solution-treated condition, (e,f) A175-24- peak-aged condition, (g,h) A175-48- over-aged condition, and (i,j) DA185-12- over-aged condition. Intra-granular corroded regions are highlighted with yellow arrows.

Increasing the volume fraction and size of the precipitates during aging depletes the matrix of ennobling elements like Cu creating micro galvanic cells across the microstructure and lowering the corrosion resistance of the material [236,237]. This is observed in Figure 5-17 and Table 5.2 where the peak-aged (A175-24) and over-aged (A175-48, DA185-12) conditions show a similar decrease in corrosion resistance. The high precipitate fraction and their homogenous distribution observed in all three conditions in Figure 5-8 leads to inter- and intra-granular galvanic corrosion shown in Figure 5-18 (e-j). However, due to other contributing factors such as grain size and precipitate-free zone (PFZ), further investigations are required to correlate the precipitate size and fraction with corrosion behavior.

5.5 Conclusions

The influence of precipitate hardening treatment on the microstructure, mechanical, and corrosion properties of LPBF A20X was studied. Two types of aging treatments were conducted: single-step aging at temperatures of 150,175,200 °C, and double-aging involving pre-aging at 165

°C followed by aging at 185 °C. The tensile properties of the alloy were evaluated at 25 and 150 °C. The key findings of this study are as follows:

1- The as-printed microstructure contained fine equiaxed grain structure (1.09 ± 0.16 µm) with inter-metallics decorating the grain boundaries. The precipitates were identified as incoherent Al_2Cu (θ) ($\{110\}_\theta \parallel \{220\}_{Al}$) present both in intra- and inter-granular regions. Metastable Cu-rich phases such as θ′ or Ω were not observed in the initial microstructure.

2- Peak hardness (155 ±1 HV) at all aging temperatures was achieved with the coexistence of coherent (Ω) and non-coherent (θ) precipitates. A silver-rich layer was only observed at the Ω-α interface. The double-aging treatment combines the advantages of fine-spaced nucleation at a lower temperature (165°C) with rapid precipitate growth at higher temperatures (185°C). This approach optimizes strengthening processes, resulting in enhanced mechanical properties within a short heat treatment duration.

3- The grain size of LPBF A20X grew by 200% after solution treatment and remained relatively constant (3-3.5 µm) for all aging temperatures up to near-peak-hardness conditions. However, longer heat treatments produced larger grain sizes up to 6 µm.

4- Heterogeneous plastic flow in the form of yield point phenomenon and serrations was exclusively observed in as-printed A20X tested at room temperature. However, solution and aging treatments eradicated this behavior by reducing the dislocation density and consuming solute atoms during precipitation.

5- Age hardening improved the room temperature yield and tensile strengths of A20X by up to 33.4% and 15.5%, respectively. The developed heat treatment (double-aging) resulted in better mechanical properties compared to single-aged (A175-48) owing to its finer grain (3.01 ± 0.98 µm) size and tighter precipitate spacing (30.8 ± 3.9 nm).

6- In as-printed A20X, the intragranular regions were selectively corroded due to low solute content. Dissolution of precipitates transformed corrosion behavior from intra- to inter-granular. In single- and double-aged conditions, zones along grain boundaries and secondary particle/matrix interface were preferentially corroded due to galvanic reaction between matrix and secondary phases.

CHAPTER 6 ARTICLE 3: EFFECT OF LASER CONTOUR SCAN PARAMETERS ON FATIGUE PERFORMANCE OF A20X FABRICATED BY LASER POWDER BED FUSION

H. Karimialavijeh[1], M. Ghasri-Khouzani[2], A. Das[1], M. Pröebstle[3], and É. Martin[1,2*]

Published in International Journal of Fatigue on June 17th, 2023

(https://doi.org/10.1016/j.ijfatigue.2023.107775)

6.1 Abstract

Laser contour scanning was used to improve the surface finish and fatigue properties of A20X components produced by laser powder bed fusion. The effects of four different contour laser scan speeds and three different offset distances were evaluated using mechanical testing and advanced characterization. The maximum profile valley depth (R_v) improves by 50.5 % when laser scan speed decreases from 850 mm/s to 350 mm/s, resulting in fatigue life improvement by 200%. The laser contour parameters affect the type and number of pores created close to the surface of the specimens. However, subsurface pores do not affect fatigue life since a fully surface-driven failure mechanism was observed in this study.

Keywords: Laser powder bed fusion; contour scanning; aluminum alloy; surface roughness; fatigue life

6.2 Introduction

Additive manufacturing (AM), also known as 3D printing, allows complex geometries to be directly constructed from their computer aided design (CAD) models in a layer-by-layer manner. Laser powder bed fusion (LPBF) is the most widely used metal AM technology capable of processing various metallic alloys, including titanium alloys [238,239], steels [84,240,241], nickel-based superalloys [76–80], and aluminum alloys [100,242]. Compared to other metal AM techniques, LPBF provides higher geometrical and dimensional accuracy, lower material waste, and finer spatial resolution [243–245]. Despite these advantages, LPBF-built components commonly suffer from poor surface integrity compared to their machined counterparts due to processing challenges such as balling, adhesion of partially melted powder particles, lack of fusion defects, and staircase (stepping) effect [246]. These defects deteriorate the fatigue performance of LPBF parts by acting as crack initiation sites [247]. Muhammad et al. 2021 [248] identified surface condition as the sole cause for failure of several LPBF aluminum alloys. To solve this challenge, many post-processing surface treatments have been employed to improve the surface integrity of the LPBF-built components. Common examples include mechanical, chemical, laser and electrochemical polishing, cavitation, laser shock and shot peening, vibro-finishing, mechanical, chemical and electrochemical machining, sand-blasting, and chemical etching [249]. However, all these surface treatments are costly and time-consuming. Moreover, some treatments, such as mechanical polishing and machining, are not applicable to structures with complex geometries.

To avoid the need for post-fabrication surface treatments, LPBF process parameter optimization has been proposed as an alternative [167,250–253]. Surface quality can also be enhanced by adding a contour scan along the free surface of the component [254]. The contour scan is applied to each layer upon completion of the bulk section. The effects of contour scan parameters on the surface roughness of LPBF have been evaluated for different materials. For example, the surface roughnesses of Ti-6Al-4V alloy [255] and pure copper [256] were reported to decrease due to additional contour scans from 33.3 to 13.2 µm and from 12.0 to 2.9 µm, respectively. Reiber et al. 2021 [257] reported that surface roughness (R_a) less than 7 µm is achievable using high-energy contour scans in LPBF Scalmalloy. Surface roughness improvement has also been reported in the 718 nickel-based superalloys [258].

Very few studies have evaluated the impact of laser contour scan strategies on low cycle fatigue (LCF) life. Gockel et al. [71] reported the effect of surface roughness on the fatigue durability of IN718 following the modification of laser power and scan speed in the contour. Applying an additional contour scan during the LPBF fabrication of Scalmalloy (Al-Mg-Mn-Sc) was found to reduce the surface roughness (R_a) from 17 µm to 6 µm and increase the fatigue resistance by 20% [259]. Buchenau et al. [74] reported that the fatigue life of LPBF AlSi7Mg0.6 alloy improved significantly upon the reduction of surface roughness from 7.35 to 3.16 µm. Other studies focused on the effect of laser power and scan speed on AlSi10Mg [260–263]. However, to the author’s knowledge, the coupled effect of laser contour scan speed and offset distance on LCF properties of additively fabricated aluminum alloys has not yet been investigated. This is important since these two parameters strongly influence the manufacturing time and cost. Moreover, the presented studies did not evaluate the effect of laser contour scan parameters on the process-induced defects and how they affect the LCF properties.

Recently developed A20X is a composite of TiB_2 ceramic particles and Al-Cu-Ag-Mg aluminum matrix. The material exhibits high strength due to grain refinement strengthening by TiB_2 particles, precipitation strengthening by Al_2Cu precipitates, and solid solution strengthening by Cu and Mg alloying elements [100]. A20X components used in aerospace applications need to exhibit excellent fatigue performance to withstand cyclic loading during service. Although the hardness and tensile properties of LPBF-built A20X have been evaluated in several studies [100,264,265], there is no known investigation of the material's fatigue characteristics in literature. Only one study [36] evaluated the effect of laser parameters on A20X mechanical properties and microstructure, but no study has reported the effect of laser contour scanning parameters on the surface roughness and mechanical properties of A20X.

The present study aims to optimize the contour scan parameters to minimize surface roughness and improve the fatigue resistance of the LPBF A20X. Emphasis is placed on contour scan speed and offset distance since they affect the build rate and manufacturing costs. Advanced characterization was performed to better understand the formation of surface and subsurface defects and their relative contribution to crack initiation and propagation. Finally, LCF testing was performed to determine the best laser contour scan strategy to improve the fatigue life of LPBF A20X components.

6.3 Materials and methods

6.3.1 Feedstock material and sample fabrication

A pre-alloyed A20X aluminum powder was used as the feedstock material in this study, whose composition is summarized in Figure 6-1 (a). This alloy contains between 4.5-5 wt.% TiB_2 particles added to the feedstock alloy before the atomization process. The powder particles were mainly spherical with a particle size range (D_{10}-D_{90}) of 15-63 µm, as shown in Figure 6-1 (b). A GE Additive M2 Series 5 LPBF printer was used to fabricate round fatigue test specimens from the A20X powder. The printing process was conducted under N_2 gas to keep the O_2 level in the build chamber below 0.1 %. A total of 42 specimens were printed in seven different protective casings (13 cm in height and 6 cm in diameter). The casings protect the surface of the specimen during handling. Six fatigue bars with a height of 130 mm were printed within each casing. Note that there was no contact between the specimen gauge and the protective casing. The grip regions of the printed specimen were machined from the initial diameter (15 mm) to the final thread dimension (0.500-20-UNF-3A). The gauge section was left intact to evaluate the effect of surface roughness on LCF properties. An image of the printed parts with the build plate is illustrated in Figure 6-2 (a). The fatigue test specimens had a gauge length and diameter of 19.05 mm and 5.08 mm, respectively, as shown in Figure 6-2 (b). All specimens were printed vertically, where the specimen's central axis was parallel to the build direction (BD).

Element	**Content [wt.%]**
Cu	4.55
Mg	0.29
Ag	0.83
Ti	3.61
B	1.36
Fe	0.06
Si	0.07
Al	Bal.

(a)

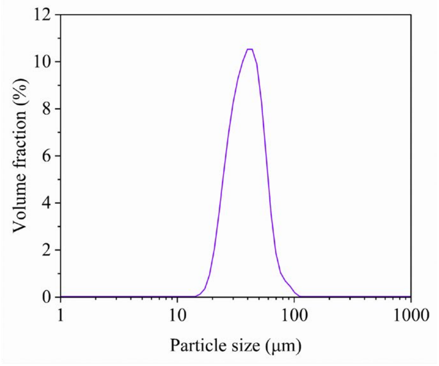

(b)

Figure 6-1. A20X powder (a) chemical composition in wt.%, and (b) particle size distribution used to fabricate fatigue specimens.

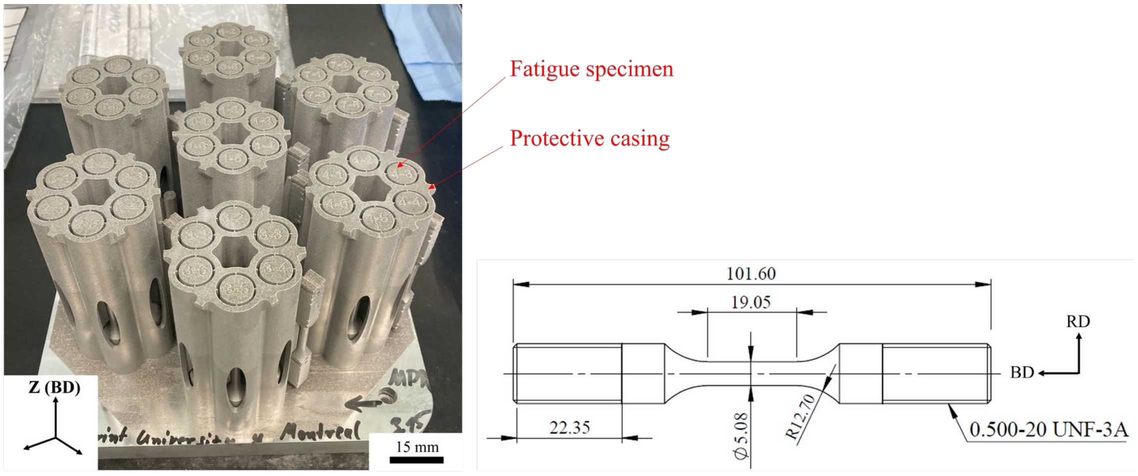

(a)

(b)

Figure 6-2. (a) A 3D view of the printed fatigue specimens attached to the build plate in a vertical (build direction) orientation. The specimens were surrounded by protective cases printed simultaneously. (b) The LCF specimen dimensions (mm) used in this study. The build direction (BD) and the LCF sample radial direction (RD) are shown here.

Optimized LPBF parameters for the A20X alloy originally presented in [36] were used to fabricate all fatigue test specimens. The parameters were 370 W laser power, 1250 mm/s scan speed, 175 µm beam diameter, 140 µm hatch spacing, and 40 µm powder layer thickness. For each layer, an additional contour scan was incorporated at the outer edge of the specimens. The laser power of 200 W and beam diameter of 85 µm were kept constant for all contour scans. Seven different contour parameters, including four different contour scan speeds (350 to 850 mm/s) and three different offset distances (50 to 100 µm), were employed, as enumerated in Table 6.1 The offset distance is the gap between the hatch scan zone and the contour scan zone. Note the laser parameters of the contour scan for conditions S1 and S5 are the same. However, two overlaid contour scans were applied at the end of each layer for condition S5, while only one pass was applied for the other conditions.

Table 6.1. Contour scanning parameters used in the fabrication of fatigue specimens. Two passes were applied to the S5 condition and only one for the other conditions.

Specimen ID	**Scan Speed (mm/s)**	**Offset Distance (µm)**
S1	850	50
S2	600	50
S3	475	50
S4	350	50
S5	850	50
S6	850	75
S7	850	100

6.3.2 Microstructure and surface characterization

The printed specimens were cross-sectioned, mounted in a copper-filled epoxy resin, ground with SiC papers, and polished with diamond suspensions. The polished samples were cleaned using ethanol and distilled water in an ultrasonic cleaner. A Keyence VHX7000 optical microscope was used to observe porosities in the as-built parts.

For high magnification observations, a JEOL JSM-7600F field emission gun scanning electron microscope (FEG-SEM) with an accelerating voltage of 5 kV and a working distance of 8 mm was used. Upon fatigue testing, the specimen fracture surfaces were observed using the aforementioned SEM to determine the failure mode. In all cases, an accelerating voltage of 10 kV and a working distance of 7 mm were employed.

To study the texture and grain size of printed bars, a Thermo Scientific Quattro electron microscopy coupled with an electron back-scattered diffraction (EBSD) detector was used. An accelerating voltage of 20 V and a step size of 0.2 μm was used. The TSL-OIM software, coupled with a MATLAB script, was utilized to acquire and process the data.

Surface roughness was measured using a Mitutoyo Formtracer Avant S3000 equipped with a stylus of 5 μm tip radius. For each specimen, seven profiles with an evaluation length (ln) of 12.5 mm and sampling length (l_r), cut-off value (λ_c) of 2.5 mm along the gauge section were obtained. Arithmetic mean roughness (R_a), the maximum height (R_z), root mean square average roughness (R_q), maximum valley depth (R_v), and total height (R_t) of the profile were determined according to ISO 4287 standard [266]. Optical 3D micrographs from the surface of the as-printed specimens were acquired. For each specimen, an area with the size of 1×1 mm on the gauge section was imaged and flattened using the VHX application.

6.3.3 Fatigue testing and fractography

Room temperature low cycle fatigue tests were conducted in accordance with ASTM E606 standard [267] using a MTS 810 mechanical testing machine equipped with a 25 KN load cell. For each specimen, constant amplitude fatigue tests were carried out using the total strain range of 0-0.495% and a strain ratio of R=0. Axial deformation was monitored using an MTS 632.13F-20 extensometer with a 10 mm gauge length. The straining cycle followed a linear ramp waveform at a constant frequency of 0.5 Hz. The fatigue cycling continued until the 75% force drop criterion was satisfied. Following the removal of the extensometer, the sample was pulled to final fracture.

Prior to LCF tests, tensile tests were conducted according to ASTM E8/E8M [268] with a strain rate of 10^{-3} s^{-1} (not shown here). Tensile test results for samples fabricated with different contour scan conditions revealed no difference in mechanical properties, such as Young's modulus, yield stress, and ultimate strength.Three fatigue tests were conducted for each printing condition to ensure that results were reproducible. A representative stress-strain curve taken from condition S1 is shown in Figure 6-3 (a). At the test onset, plastic deformation was introduced in the material opening the hysteresis loop. The hysteresis loops shrunk rapidly due to strain hardening and became stable after ~50 cycles, reaching a constant maximum stress value of 244 MPa, as shown in Figure 6-3 (b). The cracks usually initiate and begin to propagate at approximately 30-40% of the total test time (~2500 cycles in Figure 6-3 (b)). The load-bearing capability reduced gradually and the maximum stress required to reach the upper strain value dropped continuously till the failure criterion was satisfied. The minimum stress value remained constant (-110 MPa) for all the specimens tested due to the constant load-bearing capacity under compressive loads, as shown in Figure 6-3 (b).

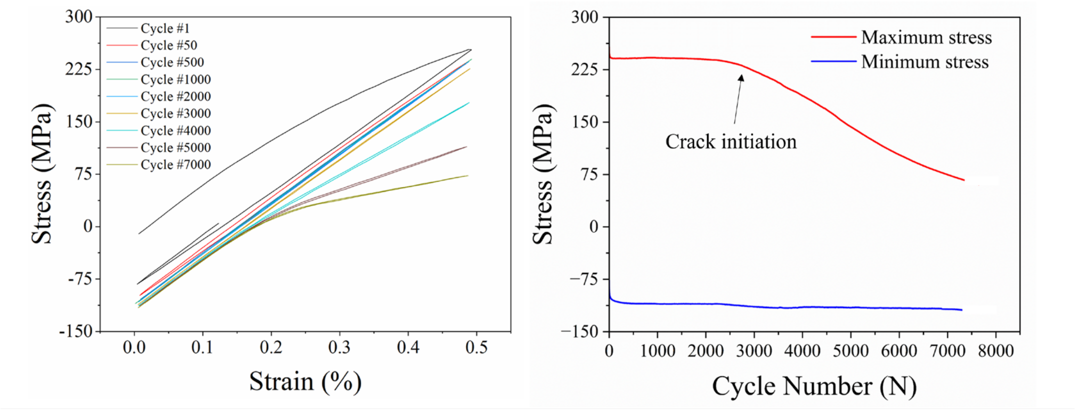

(a) (b)

Figure 6-3. Representative LCF (a) stress-strain curves at different cycles, and (b) maximum, minimum stress evolution during the test taken from condition S1 (850 mm/s, 50 μm).

6.4 Results and discussion

6.4.1 As-built microstructure analysis

6.4.1.1 Bulk region microstructure

The bulk microstructure of the as-printed A20X was analyzed in cross sections parallel and perpendicular to the build direction. The microstructure was entirely homogenous and no epitaxial grain growth was observed. The bulk microstructure (representative image shown in Figure 6-4 (a)) consists of small equiaxed grains (average GS = 1.09 µm ±0.11) with fine intercellular (< 200 nm) and trans-cellular Al_2Cu (θ) precipitates. The X-ray diffraction analysis (not shown here) revealed a 4-5% volume fraction for Al_2Cu (θ) in all specimens. Titanium diboride (TiB_2) particles with sizes below 1 µm were also observed. The Titanium diboride is added to the alloy to promote a fully equiaxed microstructure and random texture. Xi et al. 2020 [117] reported at least 2 wt.% of nucleation agents is required to avoid forming directional microstructure with preferential crystallographic orientation. The content of TiB_2 was between 4.5-5 wt.% based on the X-ray diffraction analysis. A complete analysis of the A20X LPBF microstructure is reported in [36].

The effectiveness of TiB_2 on random texture generation in as-printed A20X is evident in Figure 6-4 (b)-(c). Figure 6-4 (b) shows an inverse pole figure (IPF) map demonstrating a fully equiaxed structure with random orientations. Pole figures in Figure 6-4 (c) do not show typical LPBF texture ($\{001\} \parallel$ BD) of aluminum alloys. The intensity of poles {001}, {110}, and {111} was low (< 2 MROD) with a wide orientation spread. The observed equiaxed grain structure with random crystallographic orientations was consistent within the built material.The random equiaxed microstructure observed here is consistent with previous observations made on A20X alloys processed by LPBF [36,111,123,183,269,270].

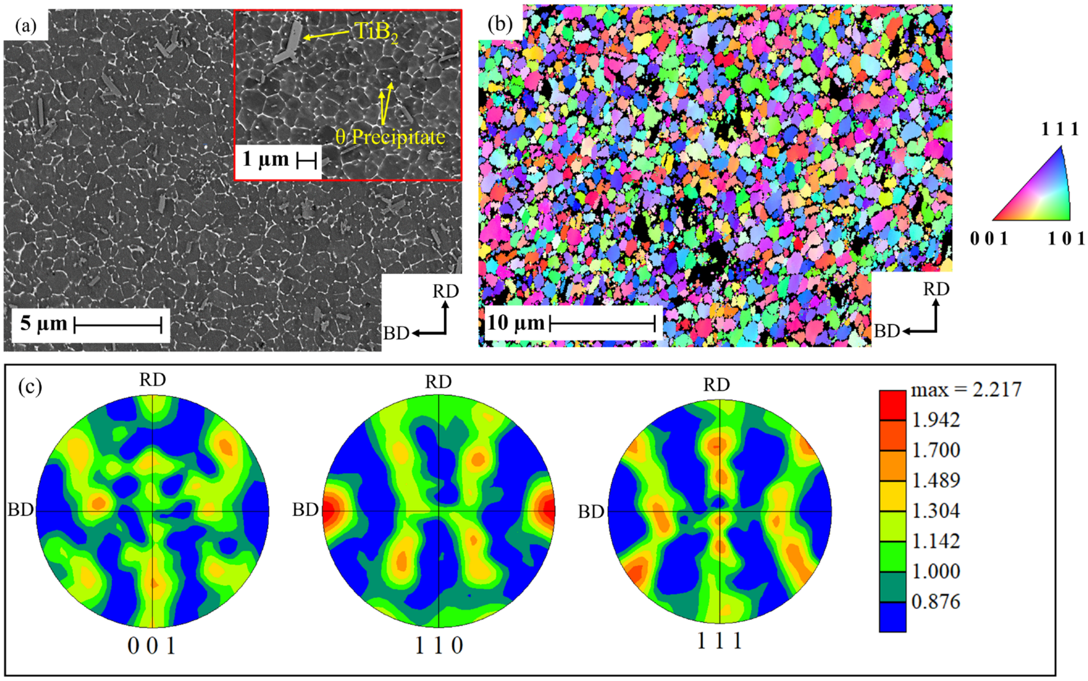

Figure 6-4. Microscopic characterization performed in the bulk region of as-printed A20X along the build direction taken from condition S1 (850 mm/s, 50 µm). (a) SEM micrograph showing fine cellular structure and the presence of intermetallic phases and TiB_2 particles, (b) IPF map showing grain orientations with respect to the build direction, and (c) EBSD {001}, {110}, and {111} pole figures of as-printed A20X. The build direction (BD) and radial direction (RD) correspond to the specimen axis shown in Fig. 2 (b).

6.4.1.2 Contour region microstructure

Laser contour parameters had very little effect on the microstructure of as-printed A20X in the contour region. This is illustrated in Figure 6-5, where the microstructure of specimens built with the most extreme contour laser parameters (S1 – highest contour scan speed, S4 – lowest contour scan speed, S7 – largest contour offset distance) are compared. In all cases, the microstructure of the contour region resembles the bulk region presented in Figure 6-4, consisting of small equiaxed grains without any epitaxial growth with respect to the build direction. Secondary phases, including Al_2Cu and TiB_2 particles, have identical size and distribution in Figure 6-5 compared to the bulk structure shown in Figure 6-4 (a). This is consistent with Ghasri-Khouzani et al. [36,92]

who reported overaged as-printed A20X microstructure and no influence of laser parameters, like scan speed and hatch spacing, on the size and volume fraction of the precipitates.

Contour grain size was the only aspect of the A20X microstructure affected by contour scan parameters. The grain sizes were measured according to the ASTM E112-13 standard and are shown in the top right corner of the SEM micrographs in Figure 6-5. The grain size was found to change slightly with laser speed but remained constant when changing the contour offset distance. In Figure 6-5, the grain size of the S1 condition (850 mm/s) was around 1.08 µm. After reducing the contour scan speed in condition S4 (350 mm/s), the grain size increased to 1.48 µm. The large contour offset distance (100 µm) in condition S7 (Figure 6-5 (c)) did not change the grain size (1.04 µm) compared to condition S1 (1.08 µm) since they had the same scan speed (850 mm/s). These observations are consistent with Ghasri-Khouzani et al. [36] who reported very small increase in the A20X grain size with the laser scan speed and no change with the laser hatch spacing. Here, the contour grain size varied between 1.04 - 1.48 µm for different contour scan parameters. These values are similar to the grain size observed in the bulk region (1.09 µm) shown in Figure 6-4.

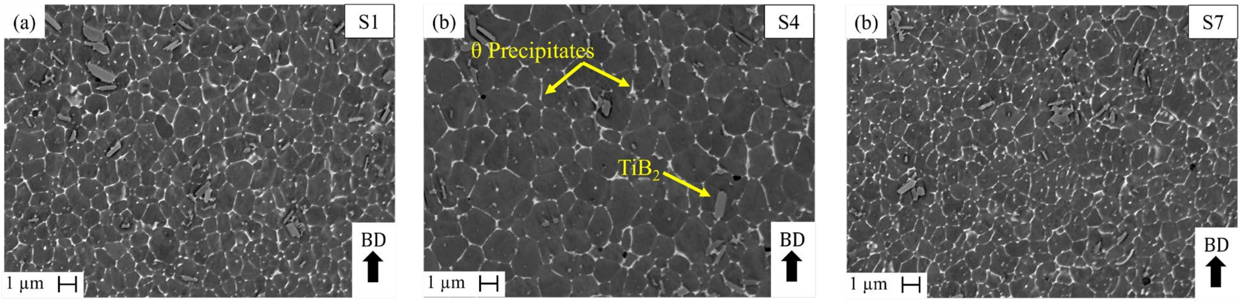

Figure 6-5. SEM micrographs of the contour region microstructure in specimens built with different laser parameters: (a) S1 (850 mm/s, 50 µm), (b) S4 (350 mm/s, 50 µm), and (c) S7 (850 mm/s, 100 µm). The average grain size is shown in the top right corner of each image.

Typical optical micrographs from cross-sections of as-built fatigue specimens with different contour scan parameters (listed in Table 1) are illustrated in Figure 6-6. The porosity content in the bulk region was identical (0.30 ± 0.20%) for all samples due to identical LPBF fabrication parameters. This was determined from the relative bulk density measured by the Archimedes method according to ASTM B962-17 [271]. Samples were ground prior to density measurement to remove the contour layer.

The size and number of subsurface pores in the contour region increased significantly when the contour scan speed decreased from 850 to 350 mm/s (S1 to S4). A similar trend was previously observed for the AlSi10Mg [272] and 6061 [273] aluminum alloys when the scan speed dropped from 1200 to 100 mm/s and from 800 to 400 mm/s, respectively, due to the keyhole pore formation mechanism. The critical scan speed for keyhole pore formation increases with the laser power [273]. However, scan speed reduction increases the laser energy density when the laser power is kept constant. Consequently, metal evaporation causes keyhole pore formation and vapor cavity collapse within the melt pool [274,275]. Figure 6-7 (a)-(b) show keyhole defects observed in contours fabricated with a low scan speed (350 mm/s). The melt pool boundary is illustrated using a yellow dashed line with keyhole pore concentration apparent at the bottom of the melt pool in Figure 6-7 (b).

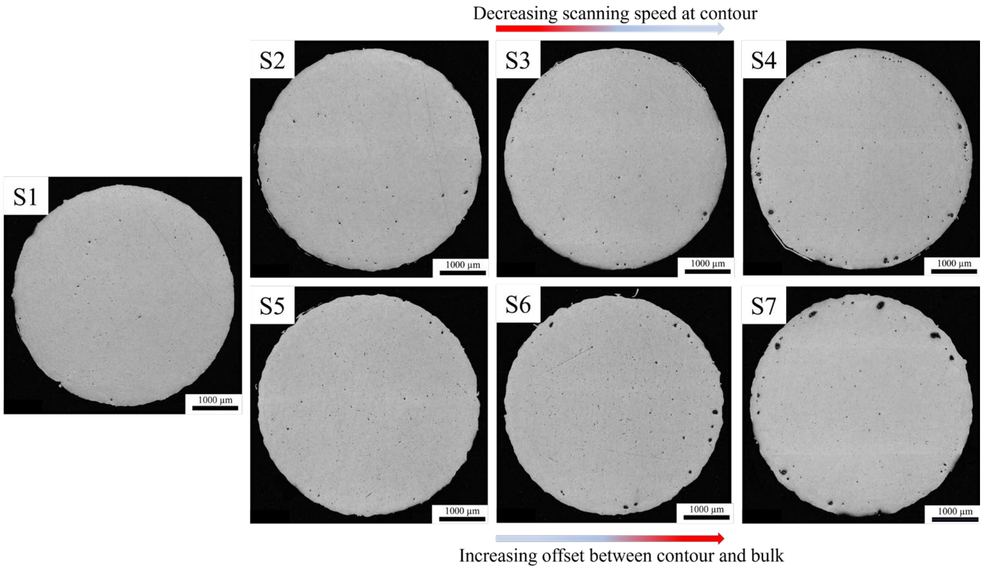

Figure 6-6. Optical micrographs from gauge cross-section of the as-built LCF specimens. The contour condition for each condition ID is presented in Table 6.1. These images were taken prior to LCF testing.

The pore size and volume fraction increased with the contour laser offset distance in Figure 6-6 (S1, S5, S6, and S7 conditions). Most pores were elongated with sizes ranging between 40 to 200 μm and located between the bulk and contour scan regions. These morphologies and sizes are characteristic of lack of fusion pores arising from insufficient consolidation between metal powder particles in the bulk/contour interface [276–278]. Figure 6-7 (c)-(d) show lack of fusion voids when a large contour offset (100 µm) is used. Non-melted powder particles were observed within the void presented in Figure 6-7 (d). The lack of fusion pores generally appear larger and more elongated compared to the smaller and rounder keyhole pores [279].

Lack of fusion defects can also be generated when the contour melt pool shrinks due to high laser speed [71]. As the melt pool becomes smaller, the critical offset distance for lack of fusion formation decreases. In this case, the defects form closer to the surface and are occasionally connected to the surface. Here, the specimens S6 and S7 were fabricated with the largest offset distance (75, 100µm) and highest laser scan speed contour (850 mm/s). They also exhibited the highest amount of lack of fusion subsurface voids connected to the surface.

The use of the double contour laser pass in the S5 condition did not change the amount of porosity when compared to the single pass specimen S1 in Figure 6-6. The addition of a second contour pass on LPBF-built 300 maraging steel was reported to be beneficial to reduce porosity along the surface of the LPBF specimens [280]. These contradictory results suggest that material or laser parameters influence the effect of second laser contour passes on surface defects, and more investigations are required to better understand the phenomenon.

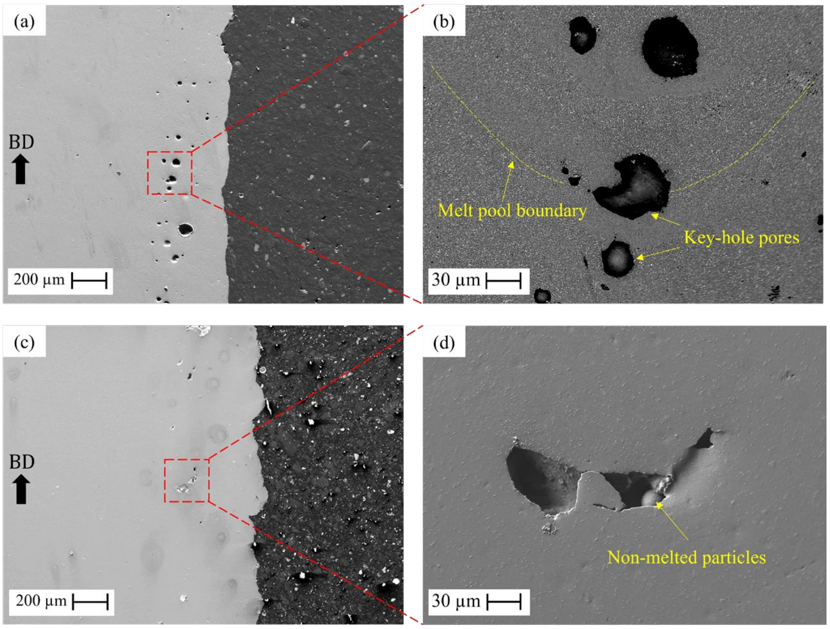

Figure 6-7. SEM micrograph showing the two types of pores observed below the surface of specimens processed with different laser contour parameters. (a) Low magnification, and (b) high magnification back-scattered images showing keyhole porosities generated by low laser contour

scanning speed (350 mm/s) in S4 condition. The melt pool boundary is highlighted using a dashed line, and keyhole pores using yellow arrows. (c) Low magnification and (d) high magnification secondary electron images showing lack of fusion voids containing non-melted particles in S7 condition built using a large laser contour offset (100 µm) and high contour scan speed (850 mm/s).

6.4.2 As-built surface roughness analysis

The effects of laser contour scan speed and offset distance on different surface roughness parameters (R_a, R_q, R_v, R_z, and R_t) for all the conditions investigated in this study are presented in Figure 6-8. All surface roughness parameters increased with increasing scan speed in Figure 6-8 (a) and (b).

Arithmetic roughness (R_a) increased from 3.84 ± 0.49 to 7.43 ± 0.41 µm with increasing scan speed (Figure 6-8 (a)). Root mean square roughness (R_q) was very similar to R_a for each condition because both represent global variation of the roughness profile. The maximum profile valley depth (R_v) increased from 9.93 ± 0.90 to 20.05 ± 3.50 µm by increasing the scan speed from 350 to 850 mm/s. R_v represents the deepest valley with respect to the median line and is often used to relate surface roughness to fatigue behavior [71]. The maximum height (R_z) and total height (R_t) of the profile increased by 126 % and 110 %, respectively, as contour scan increased by 143% in Figure 6-8 (b). Similar trends were previously reported for AlSi10Mg [281] and Hastelloy X [282] fabricated by LPBF.

On the contrary, all the surface roughness parameters were insensitive to contour offset distance, as shown in Figure 6-8 (c) and (d). For example, R_a (7.80-8.12 µm) and R_v (20.35-23.10 µm) remained relatively constant, when larger offset distances were used. The surface roughness of LPBF components is generally reported to be more sensitive to the scan parameters controlling the laser energy density, like laser power, scan speed, and hatch spacing [283]. In Figure 6-8 (c) and (d), the laser energy density was constant due to the same speed (850 mm/s) used in their laser contour scans.

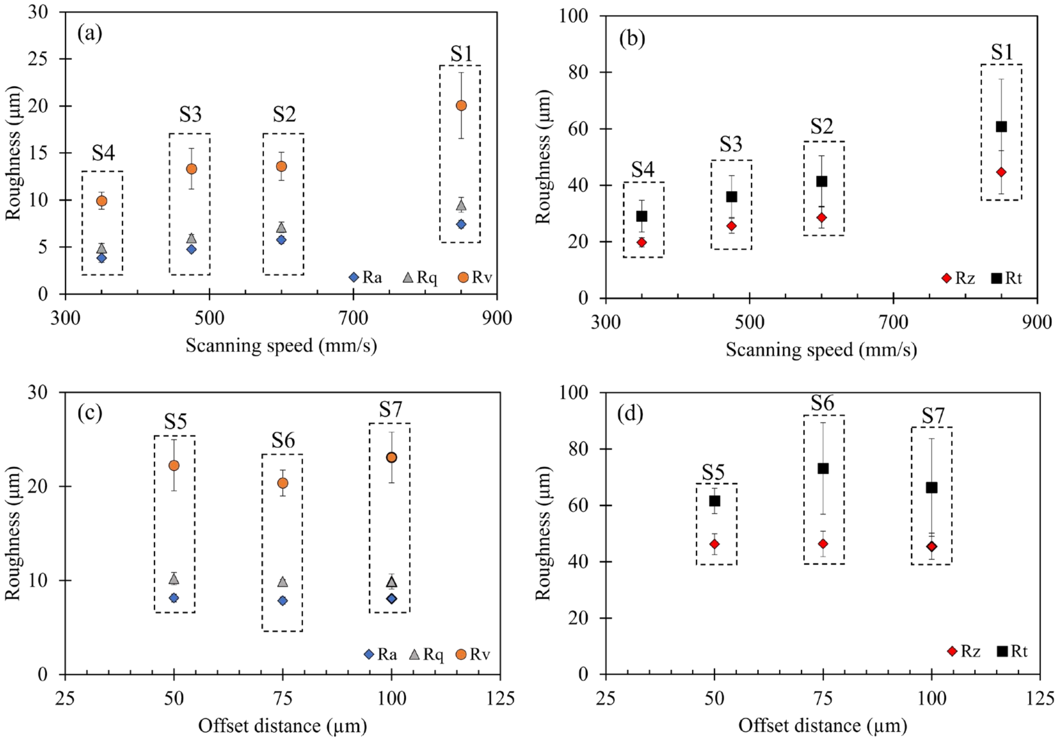

Figure 6-8. Surface roughness parameters for the as-built A20X specimens are shown as functions of (a, b) laser contour scan speed and (c, d) offset distance. Conditions grouped in (a) and (b) have the same contour offset distance (50 μm) but different scan speeds. Conditions grouped in (c) and (d) have the same contour scan speed (850 mm/s) but different offset distances.

The effect of laser scan speed on surface roughness is explained in Figure 6-9. The surface roughness in LPBF-printed metals is highly affected by the melt pool geometry [284,285]. At high laser scan speeds, the melt pool depth/width ratio is low and oval-shaped melt pools are created. When the laser scan speed decreases, the depth/width ratio increases favoring more circular melt pools [92,257]. The effect of stacking oval-shaped melt pool (low depth/width ratio) in Figure 6-9 (a) is compared with more circular-shaped melt pool (high depth/width ratio) in Figure 6-9 (c). The low depth/width ratio creates deeper valleys between the melt pools and a rougher surface. Accordingly, conditions S1 (850 mm/s) in Figure 6-9 (b) exhibits higher surface roughness. By decreasing the scan speed, the melt pool becomes bigger reducing the angle of intersection between the stacked melt pools [284]. This reduces the depth of valleys, as shown in Figure 6-9 (c), creating a smoother surface. This is shown in Figure 6-9 (d) where condition S4 (35mm/s) has a low surface roughness. Higher depth/width ratio also reduces the amount of melt pool intersections due to more re-melting, reducing the number of surface valleys [284].

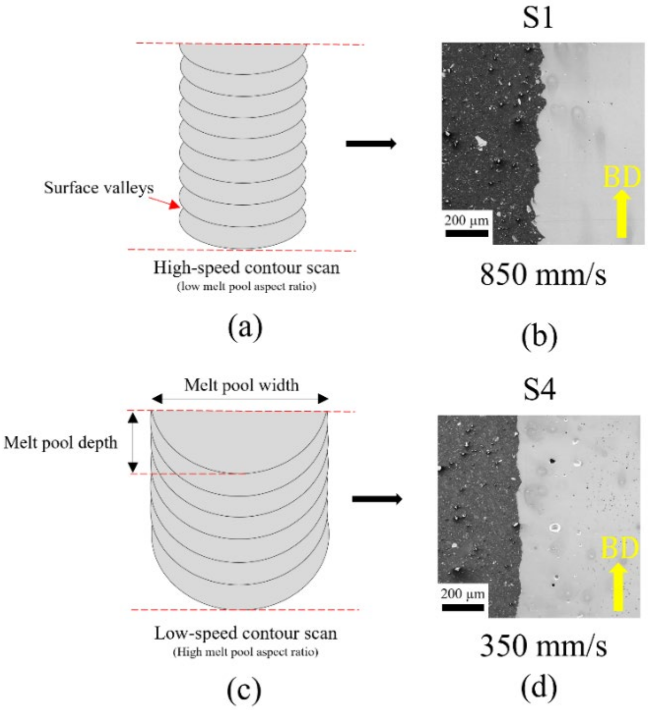

Figure 6-9. Schematic representation of the effect of laser scan speed on surface roughness. (a) Deep valleys are created when melt pools are small due to high laser scan speed. (b) Shallow valleys are created when melt pools are large and deep due to low laser scan speed. SEM image comparing the surface roughness created by (c) high (S1 (850 mm/s)) and (d) low (S4 (350 mm/s)) laser scan speed.

Typical 3D surface micrographs are shown in Figure 6-10. The color red and blue denote peaks and valleys present on the surface, respectively. The surface of sample S1 (850 mm/s), in Figure 6-10 (a), consisted of numerous hills and valleys with a maximum depth of 10 μm. Decreasing the laser contour scanning speed resulted in shallower valleys and improved surface finish. This was determined by comparing the evolution of the surface roughness between Figure 6-10 (a) and (d). The valleys in Figure 6-10 (d) (condition S4 (350 mm/s)) were almost four times shallower compared to Figure 6-10 (a) (sample S1 (850 mm/s)). Changing the offset distance did not change the surface characteristics of LPBF A20X. The conditions S6 (75 μm) and S7 (100 μm), shown in Figure 6-10 (e) and (f), had very similar surface roughness as condition S1 (50 μm) in Figure 6-10

(a) due to the same laser contour scan speed (850 mm/s). These observations agree with the results presented in Figure 6-8. Moreover, the specimen fabricated with double contour scan (S5 in Figure 6-10 (g)) exhibited very similar surface roughness to specimens S1, S6, and S7 with maximum valleys around 10 µm.

Surface anomalies (referred as surface connected particles) caused by spattering and partially melted particles [286] were also observed on the surface of specimens, as highlighted by white arrows in Figure 6-10. Such particle sizes were mostly around 10 µm, but some larger ones up to 45 µm were also observed on the surface of the specimens using SEM (not shown here). The instance of these particles increased with scan speed (see Figure 6-10 (a) and (d)). According to Khairallah et al. [286], deficient volume energy results in formation of partially and non-melted particles on the surface of LPBF components. Low contour scan speeds increased the energy density and consequently reduced the occurrence of the surface-connected particles. In the samples fabricated with an identical contour scan speed, but different offset distances, (in Figure 6-10 (a),(e),(f), and (g)), the amount of surface-connected particles did not show noticeable change as the energy density remained constant. Therefore, the surface roughness shown in Figure 6-8 is the combination of two factors: i) depth of the valleys and ii) surface connected particles. In this study, both phenomena increased with laser scan speed but remained insensitive to the offset distance.

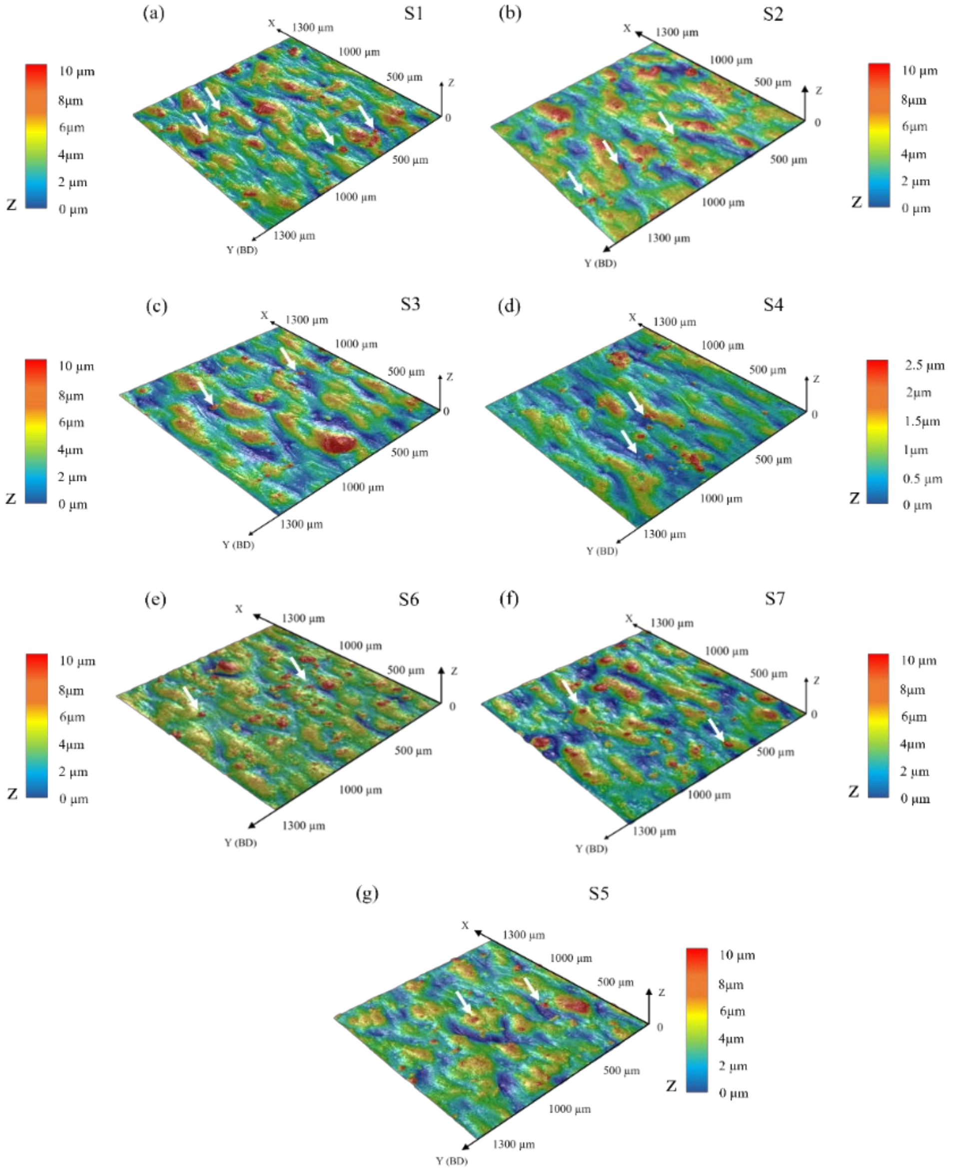

Figure 6-10. Optical 3D micrographs showing the surface roughness of as-printed specimens with different laser contour scan speeds and offset distances: (a) S1, (b) S2, (c) S3, (d) S4, (e) S6, and (f) S7. In (g), the condition S5 with double contour scan strategy is shown. Details for all conditions are listed in Table 1. White arrows highlight the surface connected particles.

6.4.3 Effect of laser contour parameters on LCF

The low cycle fatigue life of as-printed A20X as a function of contour scan parameters and surface roughness is presented in Figure 6-11. Modification of offset distance between contour and the bulk scan showed no effect on the fatigue performance (See Figure 6-11 (a)). This is because changing the contour offset distance did not affect the surface roughness, as shown in Figure 6-8. On the contrary, changing contour scan speed exhibited a profound effect on the fatigue behavior and surface roughness of A20X as shown in Figure 6-8 and Figure 6-11 (a), respectively.

Figure 6-11(b) shows the effect of surface roughness parameters on A20X LCF behavior. Improving the arithmetic average roughness (R_a) increased the lifetime of the A20X significantly. Sample S4 exhibited the longest fatigue lifetime (19367±1857 cycles) amongst all the studied conditions owing to its superior surface finish (R_a = 3.84 μm) resulting from a low-speed contour scan. By increasing the laser contour scan speed, the surface roughness increased, and the LCF life became shorter. Samples with different contour offset distances (S1, S5, S6, and S7) showed similar LCF life (~5300 to 6700 cycles) and surface roughness (R_a ~ 8 μm). This is due to the constant contour scan speed (850 mm/s) used for these conditions. The effect of R_v (depth of deepest valley on the surface with respect to median line) on the LCF life is more noticeable with a steeped curve in Figure 6-11 (b). Increasing R_v from 9.93 ± 0.89 μm to 23.07 ± 2.7 μm resulted in a 60-70 % shorter LCF life.

The contour offset distance and laser scan speed significantly affected the number and size of subsurface porosities, generally known to be detrimental to LCF properties [287]. However, the sub-surface porosities did not influence the LCF behavior in this study. On the one hand, condition S4 (N_f=19367±1857 cycles) showed the longest fatigue lifetime despite having the highest amount of sub-surface pores in Figure 6-6. On the other hand, sample S1 (Nf =6542±718 cycles), with almost no subsurface pores, exhibited a significantly shorter LCF life. Finally, conditions S1 and S7 (Nf = 6495±118 cycles)have different amounts of subsurface porosities but show similar LCF life due to similar surface roughness, as shown in Figure 6-11 (a).

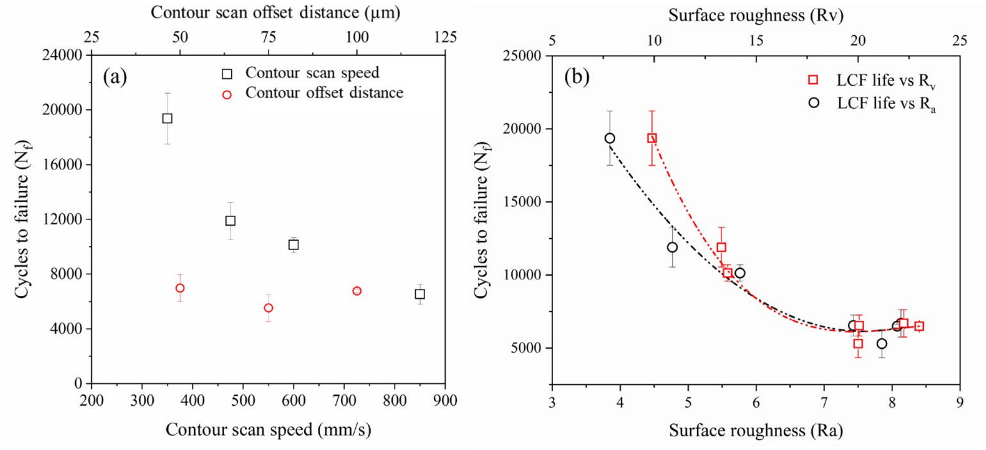

Figure 6-11. Fatigue lifetime of A20X alloy as a function of (a) contour parameters and (b) arithmetic surface roughness (R_a) and depth of deepest valley on the surface with respect to median line (R_v).

6.4.4 Fracture analysis

The previous section showed that surface roughness dominated the LCF life and that subsurface voids did not affect the LCF behavior of the as-printed A20X. This is because all the cracks initiated at the surface of the specimens under the testing condition used in this study. Figure 6-12 (a) shows the typical surface of a specimen after failure. Multiple secondary cracks (see yellow arrows) were observed along the surface valleys (see yellow dashed lines) formed by the laser contour scanning.

Figure 6-12 (b) shows a side view of a typical melt pool valley. These valleys create notch-like features favorable for LCF crack initiation [288–290]. Deeper valleys result in higher stress concentration factor and a shorter fatigue life [71]. Accordingly, the effect of R_v, representing the deepest surface valley, was more noticeable on the LCF life in Figure 6-11 (b) than R_a, representing the average valley depth. Moreover, lack of fusion defects can form on the surface of the specimen when high contour scan speeds are used. This is shown in Figure 6-12 (c) where non-melted particles revealed the occurrence of lack of fusion. These defects are deeper than normal melt pool valleys and more likely to initiate the cracks during LCF test.

Surface-connected particles were also observed on the surface of all the specimens. As discussed before (Section 3.2), these particles contribute to the average roughness (Ra) of the specimens. A large amount of these particles was observed at the surface of specimen S1 (Figure 6-12 (a)) since it was fabricated with high contour scan speed (850 mm/s). However, there was no evidence suggesting these particles contribute to crack initiation in this study.

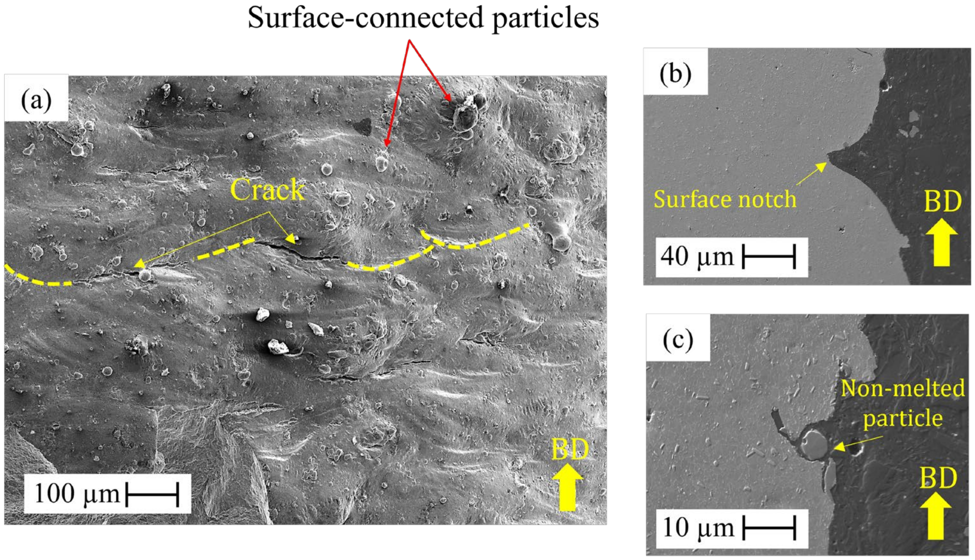

Figure 6-12. Typical surface image of LCF tested specimen (S1 condition). (a) SEM surface image showing secondary crack formation (yellow arrows) along melt pool boundaries (yellow dashed line). (b) Side view of a valley formed along a melt boundary. (c) Side view of a lack of fusion region observed at the surface of the specimens.

The fracture surfaces for the three conditions with the highest LCF life are shown in Figure 6-13. The high magnification images show cracks initiating from the valleys (see red dashed lines). The samples with deeper valleys (samples S2 and S3 in Figure 6-13(a) and (b)) had shorter LCF lives (S2 = 10139±562 cycles and S3=11900 ±1360 cycles). Sample S4 had a significantly lower surface roughness (see Fig. 8). Accordingly, cracks initiated from a shallow valley in Figure 6-13 (c) and exhibits the highest LCF life (N_f =19367 ±1857 cycles).

Decreasing the laser scan speed from condition S2 to S4 also increased the amount and size of subsurface porosities, as shown in Figure 6-6. However, these pores did not connect with the surface, thus, did not contribute to the initiation of cracks, as shown in Figure 6-13. This agrees with observations made in section 3.3.

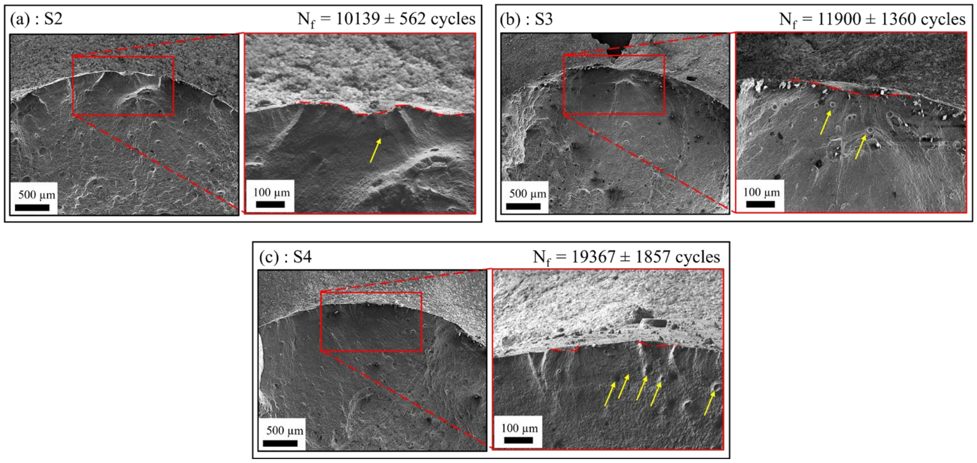

Figure 6-13. Fracture surface showing valley crack initiations in (a) sample S2 (600 mm/s, 50 µm), (b) sample S3 (475 mm/s, 50 µm) and (c) sample S4 (350 mm/s, 50 µm). The red dashed lines highlight surface valleys causing crack initiation. Yellow arrows indicate subsurface keyhole pores.

The fracture surfaces for the four conditions with the shortest LCF life are shown in Figure 6-14. In all the cases, cracks initiated along large valleys connected to subsurface non-fused regions (see red dashed lines). These features were favored by the high laser scan speed (850 mm/s) and high offset distance (≥50 µm). The combination of the non-fused regions with surface valleys creates large surface defects promoting early crack initiation and a short LCF life (between 5300-6700 cycles).

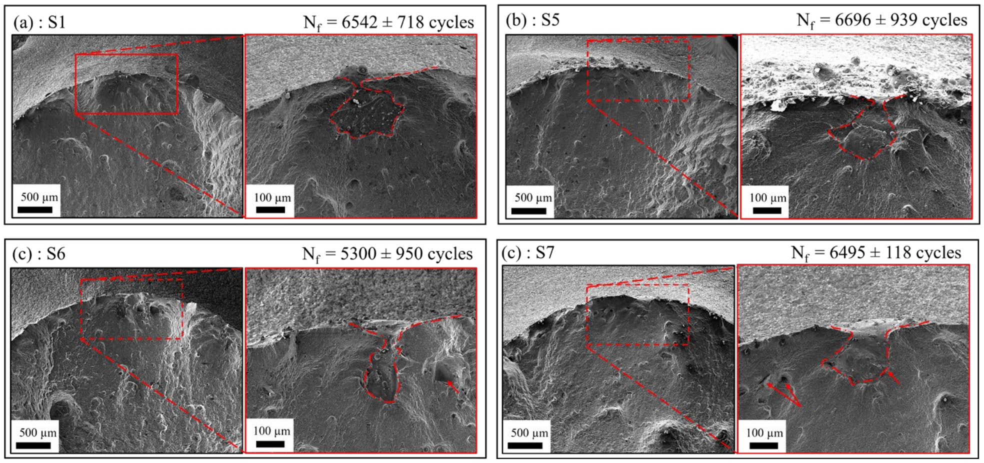

Figure 6-14. Fracture surface of samples showing cracks initiating at surface valleys connected to lack of fusion pores in (a) Condition S1 (850 mm/s, 100 µm), (b) S5 condition with double contour

scanning (850 mm/s, 50 μm), (c) S6 condition (850 mm/s, 100 μm) and (d) S7 condition (850 mm/s, 100 μm). The red arrows indicate lack of fusion pores.

6.5 Conclusions

The effect of contour scanning parameters, including the scan speed and offset distance, on the surface roughness and fatigue resistance of LPBF A20X was studied. Mechanical testing and microscopic characterization techniques were utilized to investigate the role of surface and subsurface defects on the fatigue performance of the alloy. Based on the observations in this study, the following outcomes were concluded:

1- Microstructural analysis performed on the bulk of all the studied specimens revealed a homogenous microstructure made of fine and equiaxed grains (1.09 μm) with random crystallographic orientations. The measured bulk density of all the specimens was 99.7±0.2 %. Al_2Cu (θ) precipitates (4-5% volume fraction) decorated the grain boundaries with very few small precipitates (< 200 nm) found inside the grains. Titanium diboride (TiB_2) particles with sizes below 1 μm were also observed.

2- The average grain size in the contour region increased from 1.04 μm to 1.48 μm when the laser contour speed decreased from 850 mm/s to 350 mm/s. The precipitates size and volume fraction were not affected by the laser conditions employed in this study (contours and bulk).

3- Modification of contour scanning parameters also resulted in the appearance of sub-surface voids. Decreasing scanning speed resulted in the emergence of numerous round subsurface defects caused by keyholing (20-125 μm). Increasing scan speed and offset distance increased the number of elongated voids formed due to the lack of fusion mechanism (40-200 μm).

4- The roughness of A20X alloy is highly affected by laser contour scan speed. Decreasing the scanning speed from 850 to 350 mm/s improved the arithmetic surface roughness from 7.43 ± 0.41 to 3.84 ± 0.49. However, offset variation between 50-100 μm did not influence the overall surface roughness of the as-printed A20X.

5- The fatigue performance of A20X was affected by its surface roughness. Enhancing the maximum profile valley depth (R_v) by 50.5 % extended the fatigue lifetime of the alloy by 200%. The best fatigue performance was obtained when a laser contour scan speed of 350 mm/s was employed with an offset distance of 50 μm.

6- Subsurface pores caused by keyholes and lack of fusion mechanisms did not contribute to crack initiation when not connected to the surface. In this case, they showed no effect on the LCF performance of the as-printed A20X. However, LCF life decreases when lack of fusion pores become connected with the surface valleys. This occurs when the laser scan speed is high and the offset distance is large.

CHAPTER 7 CONCLUSION AND SUGGESTION FOR FUTURE WORK

7.1 Optimizing Strength and Fatigue of A20X Alloy

This PhD research focused on optimizing the tensile strength, corrosion resistance, and fatigue properties of LPBF A20X alloys. These properties are essential for integrating aluminum alloys into the fabrication of large aircraft components such as sumps, bearing housings, frames, heat exchangers, and stationary flow path components using AM.

The first two sections of this thesis focused on post-fabrication methods, investigating various heat treatment protocols for LPBF A20X, including direct aging and conventional age-hardening treatments. The study evaluated the effects of these treatments on the alloy's microstructure, mechanical properties, and corrosion resistance. A double-aging treatment—consisting of a low-temperature aging step to promote uniform precipitate nucleation, followed by a higher-temperature step for precipitate growth—proved to be the optimal heat treatment approach for LPBF A20X. Pre-aging at 165°C for 4 hours, followed by aging at 185°C for 10–12 hours, achieved the T7 temper nearly 3 times faster than single-step aging, while improving tensile properties by 5–10% compared to existing heat treatments.

Improving the surface roughness of LPBF parts is crucial for enhancing their performance, particularly in demanding applications such as aircraft engines subjected to cyclic loading. From a mechanical perspective, surface roughness generally acts as a stress concentrator, reducing fatigue life. Traditional finishing methods, such as vibratory finishing and shot peening, are often unsuitable for large and complex components, especially those with internal regions like cooling passages.

This thesis presents a laser contour scanning strategy to improve the surface roughness of LPBF components. The application of low-speed contour scans resulted in the formation of rounder melt pools, which produced shallower surface valleys upon stacking. The optimal average roughness of approximately 4 μm was achieved using a low-speed contour scan at 350 mm/s with a low offset distance of 50 μm.

The combination of optimized heat treatments for LPBF A20X and an in-process laser contour scanning procedure enables significant improvements in tensile strength and fatigue properties without adversely affecting the material's corrosion resistance. Through optimized heat treatment, the tensile strength of the A20X alloy increased by 33.4%, when compared to the as-printed condition, while laser contour optimization extended its fatigue life by approximately 200%. These enhancements ensure that the mechanical performance of A20X components meets the stringent requirements of their intended applications.

7.2 Conclusions

Overall, the findings of this study are fundamental to understanding the response of LPBF aluminum alloys to heat treatment and provide insightful information on the effect of in-process surface optimization techniques on fatigue performance. The main findings of these studies are as follows:

Direct aging:

1- The microstructure of as-printed A20X contained dispersed incoherent Al_2Cu (θ) ($\{110\}_{\theta} \parallel \{220\}_{Al}$) within an FCC aluminum matrix. As direct aging proceeded, the θ precipitates grew larger while maintaining a constant volume fraction. The average size of the precipitates increased by approximately 100% without the formation of other metastable precipitates such as θ′ or Ω, confirming the absence of a supersaturated solution in the as-printed A20X.

2- Direct aging of A20X LPBF resulted in a loss of material hardness. As temperature and time increased, hardness decreased by up to 23.7% from its initial level. Likewise, the alloy's yield strength and ultimate strength both experienced significant declines of 27% and 19.4%, respectively, after exposure to 220°C for 30 hours. This decline is attributed to the growth of precipitates during aging and the lack of metastable precipitates (θ′ and Ω).

3- In the as-printed A20X, the Mg/Ag solute wall was observed near grain boundaries. The serrated plastic flow observed in the as-printed A20X was caused by the entrapment of moving dislocations by these solute atoms. After direct aging, the Mg/Ag wall gradually disappeared, reducing the serrations in the plastic flow.

4- In A20X, Ti and TiB_2 promote heterogenous grain nucleation. This allows the solute atoms (Cu, Mg, and Ag) to be rejected into the liquid phase even at the high cooling rates associated with LPBF. This leads to the formation of continuous intermetallic films along grain boundaries.

Solution and aging treatment:

1- Solutioning and aging resulted in significant hardening of LPBF A20X. Peak hardness was attained through the coexistence of coherent (Ω) and non-coherent (θ) precipitates. In double-aging treatment, the fine-spaced precipitates formed during the first aging step grew rapidly to the optimized size without causing significant grain growth.

2- After solution treatment, the grain size of LPBF A20X increased for all aging temperatures evaluated until approaching peak hardness conditions. Longer heat treatments resulted in larger grain sizes up to 6 μm. The optimal combination of mechanical properties and fine grain size was obtained through the double-aging treatment process (165 °C for 4 hours followed by 185 °C for 12 hours).

3- Heterogeneous plastic deformation, characterized by the yield point phenomenon and serrations, was only noted in the as-printed A20X alloy during room temperature testing. This behavior was eliminated through solution and aging treatments, which reduced dislocation density and consumed solute atoms during precipitation.

4- Age hardening led to notable improvements in the room temperature yield and tensile strengths of A20X. Notably, the developed heat treatment, specifically the double-aging process, demonstrated superior mechanical properties compared to single-aged treatments. This superiority can be attributed to the finer grain size (3.01 ± 0.98 μm) and smaller precipitate spacing achieved through the double-aging approach.

5- Within the as-printed A20X, corrosion selectively targeted intragranular regions due to their low solute content. The dissolution of precipitates shifted corrosion behavior from intragranular to intergranular. Under both single- and double-aged conditions, corrosion primarily occurred along grain boundaries and the secondary particle/matrix interface, driven by galvanic reactions between the matrix and secondary phases.

Laser contour scanning and fatigue performance:

1- Adjustments to contour scanning parameters led to the formation of sub-surface voids. Lowering the scanning speed led to the emergence of multiple round subsurface defects, which were attributed to the keyholing phenomena (20–125 μm). Conversely, increasing scan speed and offset distance resulted in an increase in the number of elongated voids, which were formed due to inadequate fusion mechanisms (40–200 μm).

2- Laser contour scan parameters significantly affected the surface roughness of LPBF A20X. Lowering the scanning speed from 850 to 350 mm/s resulted in enhancement of the arithmetic surface roughness, improving from 7.43 ± 0.41 to 3.84 ± 0.49. Interestingly, variations in offset between 50 and 100 µm did not affect the overall surface roughness of the as-printed A20X.

3- There was a strong correlation between surface roughness and fatigue performance of LPBF A20X. A higher maximum profile valley depth (R_v) resulted in a remarkable extension of the alloy's fatigue lifetime. Laser contour scan speed of 350 mm/s coupled with an offset distance of 50 µm resulted in optimal fatigue performance.

4- Subsurface pores resulting from keyholing and lack of fusion mechanisms did not influence crack initiation when isolated from the surface. Under these circumstances, they exhibited no impact on the low-cycle fatigue (LCF) performance of the as-printed A20X. However, the LCF lifespan diminishes when pores from insufficient fusion become linked with surface valleys. This phenomenon arises particularly under conditions of high laser scan speeds and large offset distances.

The findings of this study offer valuable insights into optimizing the heat treatment processes and laser contour scanning of LPBF A20X, with a focus on achieving an optimal balance between tensile properties, fatigue performance, and heat treatment duration. These conclusions provide useful information on the processing of A20X, which holds relevance for other LPBF aluminum alloys.

7.3 Limitations and suggestions for future work:

1- The study focused solely on water quenching, overlooking the impact of different cooling rates after solution treatment, which significantly influence precipitation kinetics.

Understanding these differences is crucial, as they can have substantial impact on the resulting microstructure and mechanical properties of the alloy. Future research could address this gap by investigating the effects of different quenching media, such as oil or air, and examining how these alternatives influence the microstructure and mechanical performance. This expanded scope would provide a more comprehensive understanding of the optimal cooling processes needed to enhance the properties of the A20X alloy.

2- In this study, the primary focus was on examining the effect of heat treatment on the tensile properties of the material at both room and elevated temperatures. While this approach provided valuable insights into the material's strength and performance under static loading conditions, it did not address the significant impact of precipitation on the material's cyclic fatigue behavior. Understanding how the material performs under cyclic loading is crucial, especially in critical applications. Future studies should explore the cyclic behavior of the material across a range of temperatures to gain a more comprehensive understanding of its fatigue performance. This would allow researchers to assess how microstructural evolutions, influenced by various heat treatments, affect the cyclic behavior of the material. Such investigations would be instrumental in optimizing heat treatment protocols to enhance both the static and dynamic performance of the material, ensuring its reliability and longevity in real-world applications.

3- Deformation-assisted precipitation significantly enhanced the ductility of LPBF A20X. Further investigation of this behavior would be beneficial to better understand the precipitation kinetics and mechanisms during plastic deformation. Extensive TEM investigations to determine the precipitate type and habitat plane would provide valuable insights into the dynamic precipitation behavior. Additionally, the effect of plastic deformation parameters, such as strain rate and temperature, should be explored.

REFERENCES

[1] N.T. Aboulkhair, M. Simonelli, L. Parry, I. Ashcroft, C. Tuck, R. Hague, 3D printing of Aluminium alloys: Additive Manufacturing of Aluminium alloys using selective laser melting, Prog Mater Sci 106 (2019) 100578. https://doi.org/10.1016/j.pmatsci.2019.100578.

[2] VELO 3D, Blending Metal AM & Traditional Manufacturing for Next-Generation Heat Exchangers, (n.d.). https://velo3d.com/wp-content/uploads/2022/09/PWR-Advanced-Cooling-Technology-Case-Study.pdf (accessed August 9, 2024).

[3] A.J. Pinkerton, [INVITED] Lasers in additive manufacturing, Opt Laser Technol 78 (2016) 25–32. https://doi.org/10.1016/J.OPTLASTEC.2015.09.025.

[4] E. Santecchia, S. Spigarelli, M. Cabibbo, metals Material Reuse in Laser Powder Bed Fusion: Side Effects of the Laser-Metal Powder Interaction, (n.d.). https://doi.org/10.3390/met10030341.

[5] R.J. Friel, Power ultrasonics for additive manufacturing and consolidating of materials, Power Ultrasonics: Applications of High-Intensity Ultrasound (2015) 313–335. https://doi.org/10.1016/B978-1-78242-028-6.00013-2.

[6] P. Vora, K. Mumtaz, I. Todd, N. Hopkinson, AlSi12 in-situ alloy formation and residual stress reduction using anchorless selective laser melting, Addit Manuf 7 (2015) 12–19. https://doi.org/10.1016/J.ADDMA.2015.06.003.

[7] F. Trevisan, F. Calignano, M. Lorusso, J. Pakkanen, A. Aversa, E.P. Ambrosio, M. Lombardi, P. Fino, D. Manfredi, G. Requena, materials On the Selective Laser Melting (SLM) of the AlSi10Mg Alloy: Process, Microstructure, and Mechanical Properties, MDPI (n.d.). https://doi.org/10.3390/ma10010076.

[8] N.T. Aboulkhair, N.M. Everitt, I. Maskery, I. Ashcroft, C. Tuck, Selective laser melting of aluminum alloys, MRS Bull (2017). https://doi.org/10.1557/MRS.2017.63/TABLES/2.

[9] X.P. Li, G. Ji, Z. Chen, A. Addad, Y. Wu, H.W. Wang, J. Vleugels, J. van Humbeeck, J.P. Kruth, Selective laser melting of nano-TiB2 decorated AlSi10Mg alloy with high fracture

strength and ductility, Acta Mater 129 (2017) 183–193. https://doi.org/10.1016/J.ACTAMAT.2017.02.062.

[10] D.D. Gu, W. Meiners, K. Wissenbach, R. Poprawe, Laser additive manufacturing of metallic components: materials, processes and mechanisms, Https://Doi.Org/10.1179/1743280411Y.0000000014 57 (2013) 133–164. https://doi.org/10.1179/1743280411Y.0000000014.

[11] E.O. Olakanmi, R.F. Cochrane, K.W. Dalgarno, A review on selective laser sintering/melting (SLS/SLM) of aluminium alloy powders: Processing, microstructure, and properties, Prog Mater Sci 74 (2015) 401–477. https://doi.org/10.1016/J.PMATSCI.2015.03.002.

[12] Aluminum and Aluminum Alloys Introduction and Overview, (2001). https://doi.org/10.1361/autb2001p351.

[13] D. Rabinovich, The allure of aluminium, Nature Chemistry 2013 5:1 5 (2012) 76–76. https://doi.org/10.1038/nchem.1535.

[14] J. Hatch, Aluminum : Properties and Physical Metallurgy - ASM International Aluminum : Properties and Physical Metallurgy - ASM International Publisher : Aluminum Association Inc . and ASM International, (1984) 424.

[15] C.R. ’Monish, Understanding the Effect of Heat Treatment on Microstructure and Mechanical properties of A205, Master’s Thesis, Aalto Universit, 2019.

[16] M.F. Ashby, D.R.H. (David R.H. Jones, Engineering materials 2 : an introduction to microstructures, processing and design, (2006) 451.

[17] S.N. Naik, S.M. Walley, The Hall-Petch and inverse Hall-Petch relations and the hardness of nanocrystalline metals, (n.d.). https://doi.org/10.1007/s10853-019-04160-w.

[18] D.R. Askeland, Dispersion Strengthening by Phase Transformation and Heat Treatment, The Science and Engineering of Materials (1996) 316–349. https://doi.org/10.1007/978-1-4899-2895-5_11.

[19] X. Yu, L. Wang, T6 heat-treated AlSi10Mg alloys additive-manufactured by selective laser melting, Procedia Manuf 15 (2018) 1701–1707. https://doi.org/10.1016/J.PROMFG.2018.07.265.

[20] J. Fiocchi, A. Tuissi, C.A. Biffi, Heat treatment of aluminium alloys produced by laser powder bed fusion: A review, Mater Des 204 (2021). https://doi.org/10.1016/j.matdes.2021.109651.

[21] A. Mehta, L. Zhou, T. Huynh, S. Park, H. Hyer, S. Song, Y. Bai, D.D. Imholte, N.E. Woolstenhulme, D.M. Wachs, Y. Sohn, Additive manufacturing and mechanical properties of the dense and crack free Zr-modified aluminum alloy 6061 fabricated by the laser-powder bed fusion, Addit Manuf 41 (2021). https://doi.org/10.1016/J.ADDMA.2021.101966.

[22] S.Z. Uddin, L.E. Murr, C.A. Terrazas, P. Morton, D.A. Roberson, R.B. Wicker, Processing and characterization of crack-free aluminum 6061 using high-temperature heating in laser powder bed fusion additive manufacturing, Addit Manuf 22 (2018) 405–415. https://doi.org/10.1016/J.ADDMA.2018.05.047.

[23] P.A. Rometsch, Y. Zhu, X. Wu, A. Huang, Review of high-strength aluminium alloys for additive manufacturing by laser powder bed fusion, Mater Des 219 (2022). https://doi.org/10.1016/j.matdes.2022.110779.

[24] S.I. Shakil, A. Hadadzadeh, B. Shalchi Amirkhiz, H. Pirgazi, M. Mohammadi, M. Haghshenas, Additive manufactured versus cast AlSi10Mg alloy: Microstructure and micromechanics, Results in Materials 10 (2021) 100178. https://doi.org/10.1016/J.RINMA.2021.100178.

[25] S. Liu, H. Zhu, G. Peng, J. Yin, X. Zeng, Microstructure prediction of selective laser melting AlSi10Mg using finite element analysis, Mater Des 142 (2018) 319–328. https://doi.org/10.1016/J.MATDES.2018.01.022.

[26] S.L. Sing, S. Huang, G.D. Goh, G.L. Goh, C.F. Tey, J.H.K. Tan, W.Y. Yeong, Emerging metallic systems for additive manufacturing: In-situ alloying and multi-metal processing in laser powder bed fusion, Prog Mater Sci 119 (2021) 100795. https://doi.org/10.1016/J.PMATSCI.2021.100795.

[27] Z.G. Zhu, X.H. An, W.J. Lu, Z.M. Li, F.L. Ng, X.Z. Liao, U. Ramamurty, S.M.L. Nai, J. Wei, Selective laser melting enabling the hierarchically heterogeneous microstructure and excellent mechanical properties in an interstitial solute strengthened high entropy alloy, Mater Res Lett 7 (2019) 453–459. https://doi.org/10.1080/21663831.2019.1650131/SUPPL_FILE/TMRL_A_1650131_SM4652.DOCX.

[28] Y. Chew, G.J. Bi, Z.G. Zhu, F.L. Ng, F. Weng, S.B. Liu, S.M.L. Nai, B.Y. Lee, Microstructure and enhanced strength of laser aided additive manufactured CoCrFeNiMn high entropy alloy, Materials Science and Engineering: A 744 (2019) 137–144. https://doi.org/10.1016/J.MSEA.2018.12.005.

[29] J. Xu, T. Ma, R.L. Peng, S. Hosseini, Effect of post-processes on the microstructure and mechanical properties of laser powder bed fused IN718 superalloy, Addit Manuf 48 (2021). https://doi.org/10.1016/J.ADDMA.2021.102416.

[30] W.M. Tucho, P. Cuvillier, A. Sjolyst-Kverneland, V. Hansen, Microstructure and hardness studies of Inconel 718 manufactured by selective laser melting before and after solution heat treatment, Materials Science and Engineering: A 689 (2017) 220–232. https://doi.org/10.1016/J.MSEA.2017.02.062.

[31] K. Gabrysiak, T. Gustmann, J. Freudenberger, K. Neufeld, L. Giebeler, C. Leyens, U. Kühn, Development and characterization of a metastable Al-Mn-Ce alloy produced by laser powder bed fusion, Additive Manufacturing Letters 1 (2021) 100017. https://doi.org/10.1016/J.ADDLET.2021.100017.

[32] M.L. Montero Sistiaga, R. Mertens, B. Vrancken, X. Wang, B. Van Hooreweder, J.P. Kruth, J. Van Humbeeck, Changing the alloy composition of Al7075 for better processability by selective laser melting, J Mater Process Technol 238 (2016) 437–445. https://doi.org/10.1016/J.JMATPROTEC.2016.08.003.

[33] Q. Tan, J. Zhang, N. Mo, Z. Fan, Y. Yin, M. Bermingham, Y. Liu, H. Huang, M.X. Zhang, A novel method to 3D-print fine-grained AlSi10Mg alloy with isotropic properties via inoculation with LaB6 nanoparticles, Addit Manuf 32 (2020). https://doi.org/10.1016/J.ADDMA.2019.101034.

[34] J.H. Martin, D. Yahata, J.M. Hundley, J.A. Mayer, T.A. Schaedler, T.M. Pollock, 3D printing of high-strength aluminium alloys, Nature Publishing Group (2017). https://doi.org/10.1038/nature23894.

[35] R. Du, Q. Gao, S. Wu, S. Lü, X. Zhou, Influence of TiB2 particles on aging behavior of in-situ TiB2/Al-4.5Cu composites, Mater Sci Eng A Struct Mater 721 (2018) 244–250. https://doi.org/10.1016/J.MSEA.2018.02.099.

[36] M. Ghasri-Khouzani, H. Karimialavijeh, M. Pröbstle, R. Batmaz, W. Muhammad, A. Chakraborty, T.D. Sabiston, J.P. Harvey, É. Martin, Processability and characterization of A20X aluminum alloy fabricated by laser powder bed fusion, Mater Today Commun (2023) 105555. https://doi.org/10.1016/j.mtcomm.2023.105555.

[37] V.S. Zolotorevsky, N.A. Belov, M. v Glazoff, Chapter one - Alloying Elements and Dopants: Phase Diagrams, in: V.S. Zolotorevsky, N.A. Belov, M. v Glazoff (Eds.), Casting Aluminum Alloys, Elsevier, Amsterdam, 2007: pp. 1–93. https://doi.org/https://doi.org/10.1016/B978-008045370-5.50003-1.

[38] J.C. Williams, E.A. Starke, Progress in structural materials for aerospace systems, Acta Mater 51 (2003) 5775–5799. https://doi.org/10.1016/j.actamat.2003.08.023.

[39] G. Riontino, P. Mengucci, S. Abis, Precipitation sequence in an Al-Cu-Mg-Ag-Zn alloy, Philosophical Magazine A 72 (1995) 765–782. https://doi.org/10.1080/01418619508243799.

[40] J.Z. Liu, S.S. Yang, S.B. Wang, J.H. Chen, C.L. Wu, The influence of Cu/Mg atomic ratios on precipitation scenarios and mechanical properties of Al-Cu-Mg alloys, J Alloys Compd 613 (2014) 139–142. https://doi.org/10.1016/J.JALLCOM.2014.06.045.

[41] J.A. Taylor, B.A. Parker, I.J. Polmear, Precipitation in AI-Cu-Mg-Ag casting alloy, Metal Science 12 (1978) 478–482. https://doi.org/10.1179/030634578790433341.

[42] J.M. Rosalie, L. Bourgeois, Silver segregation to θ′ (Al 2Cu)-Al interfaces in Al-Cu-Ag alloys, Acta Mater 60 (2012) 6033–6041. https://doi.org/10.1016/J.ACTAMAT.2012.07.039.

[43] J. Hatch, Aluminum : properties and physical metallurgy, American Society for Metals, Metals Park Ohio, 1988.

[44] K.M. Knowles, W.M. Stobbs, The structure of {111} age-hardening precipitates in Al–Cu–Mg–Ag alloys, Acta Crystallographica Section B 44 (1988) 207–227. https://doi.org/10.1107/S0108768187012308.

[45] L. Reich, M. Murayama, K. Hono, Evolution of Ω phase in an Al-Cu-Mg-Ag alloy -a three-dimensional atom probe study, Acta Mater 46 (1998) 6053–6062. https://doi.org/10.1016/S1359-6454(98)00280-8.

[46] C.R. Hutchinson, X. Fan, S.J. Pennycook, G.J. Shiflet, On the origin of the high coarsening resistance of Ω plates in Al–Cu–Mg–Ag Alloys, 2001. https://doi.org/https://doi.org/10.1016/S1359-6454(01)00155-0.

[47] J. Forde, The elevated temperature performance of cast aluminium alloys and the development of a cast aluminium-copper metal matrix composite, in: 2015.

[48] M. Indriyati, Effect of TiB2 addition on the microstructure and mechanical properties of Al-Cu-Mg-Ag alloy, (2016). http://webcat.warwick.ac.uk/record=b3102855~S15 (accessed January 12, 2022).

[49] Y.M. Youssef, R.J. Dashwood, P.D. Lee, Effect of clustering on particle pushing and solidification behaviour in TiB2 reinforced aluminium PMMCs, Compos Part A Appl Sci Manuf 36 (2005) 747–763. https://doi.org/10.1016/J.COMPOSITESA.2004.10.027.

[50] P.L. Schaffer, D.N. Miller, A.K. Dahle, Crystallography of engulfed and pushed TiB2 particles in aluminium, Scr Mater 57 (2007) 1129–1132. https://doi.org/10.1016/J.SCRIPTAMAT.2007.08.009.

[51] Z. Fan, Y. Wang, Y. Zhang, T. Qin, X.R. Zhou, G.E. Thompson, T. Pennycook, T. Hashimoto, Grain refining mechanism in the Al/Al–Ti–B system, Acta Mater 84 (2015) 292–304. https://doi.org/10.1016/J.ACTAMAT.2014.10.055.

[52] A. Kordijazi, D. Weiss, S. Das, S. Behera, H.M. Roshan, P. Rohatgi, Effect of Solidification Time on Microstructure, Wettability, and Corrosion Properties of A205-T7 Aluminum Alloys, International Journal of Metalcasting 15 (2021) 2–12. https://doi.org/10.1007/S40962-020-00457-8.

[53] X.Y. Liu, Q.L. Pan, Z.L. Lu, S.F. Cao, Y. bin He, W. bin Li, Effects of solution treatment on the microstructure and mechanical properties of Al–Cu–Mg–Ag alloy, Undefined 31 (2010) 4392–4397. https://doi.org/10.1016/J.MATDES.2010.04.058.

[54] ECKART AM | Homepage | Eckart Germany, (n.d.). https://www.eckart.net/de/en/microsite/am (accessed June 17, 2022).

[55] Y.K. Xiao, H. Chen, Z.Y. Bian, T.T. Sun, H. Ding, Q. Yang, Y. Wu, Q. Lian, Z. Chen, H.W. Wang, Enhancing strength and ductility of AlSi10Mg fabricated by selective laser melting by TiB2 nanoparticles, J Mater Sci Technol 109 (2022) 254–266. https://doi.org/10.1016/J.JMST.2021.08.030.

[56] M. Avateffazeli, P.E. Carrion, B. Shachi-Amirkhiz, H. Pirgazi, M. Mohammadi, N. Shamsaei, M. Haghshenas, Correlation between tensile properties, microstructure, and processing routes of an Al–Cu–Mg–Ag–TiB2 (A205) alloy: Additive manufacturing and casting, Materials Science and Engineering A 841 (2022). https://doi.org/10.1016/J.MSEA.2022.142989.

[57] H. Karimialavijeh, M. Ghasri-Khouzani, A. Chakraborty, J.-P. Harvey, É. Martin, Comparison of Additively Manufactured and Cast Aluminum A205 Alloy, in: S. Broek (Ed.), Light Metals 2023, Springer Nature Switzerland, Cham, 2023: pp. 488–492.

[58] J. Barode, A. Vayyala, E. Virgillito, A. Aversa, J. Mayer, P. Fino, M. Lombardi, Revisiting heat treatments for additive manufactured parts: A case study of A20X alloy, Mater Des 225 (2023) 111566. https://doi.org/10.1016/J.MATDES.2022.111566.

[59] W. Li, S. Li, J. Liu, A. Zhang, Y. Zhou, Q. Wei, C. Yan, Y. Shi, Effect of heat treatment on AlSi10Mg alloy fabricated by selective laser melting: Microstructure evolution, mechanical properties and fracture mechanism, Materials Science and Engineering: A 663 (2016) 116–125. https://doi.org/10.1016/J.MSEA.2016.03.088.

[60] H. jung Kang, H. sung Jang, S. hyo Oh, P. hwan Yoon, G. heun Lee, J. young Park, E. soo Kim, Y. suk Choi, Effects of solution treatment temperature and time on the porosities and mechanical properties of vacuum die-casted and T6 heat-treated Al–Si–Mg alloy, Vacuum 193 (2021) 110536. https://doi.org/10.1016/J.VACUUM.2021.110536.

[61] S.P. Ringer, K. Hono, I.J. Polmear, T. Sakurai, Nucleation of precipitates in aged AlCuMg(Ag) alloys with high Cu:Mg ratios, Acta Mater 44 (1996) 1883–1898. https://doi.org/10.1016/1359-6454(95)00314-2.

[62] R.N. Lumley, Fundamentals of aluminium metallurgy : production, processing and applications, Woodhead Pub, 2011.

[63] J.H. Auld, Structure of metastable precipitate in some Al–Cu–Mg–Ag alloys, Http://Dx.Doi.Org/10.1179/Mst.1986.2.8.784 2 (2013) 784–787. https://doi.org/10.1179/MST.1986.2.8.784.

[64] S. Kerry, V.D. Scott, Structure and orientation relationship of precipitates formed in Al-Cu-Mg-Ag alloys, Http://Dx.Doi.Org/10.1179/030634584790420069 18 (2013) 289–294. https://doi.org/10.1179/030634584790420069.

[65] D. Petschke, F. Lotter, T.E.M. Staab, Revisiting the crystal structure of the equilibrium S (Al2CuMg) phase in Al–Cu–Mg alloys using X-ray absorption spectroscopy (XAFS), Materialia (Oxf) 6 (2019) 100341. https://doi.org/10.1016/J.MTLA.2019.100341.

[66] B.C. Muddle, I.J. Polmear, The precipitate Ω phase in Al-Cu-Mg-Ag alloys, Acta Metallurgica 37 (1989) 777–789. https://doi.org/10.1016/0001-6160(89)90005-9.

[67] S. Kumar, T.K.G. Namboodhiri, Precipitation hardening and hydrogen embrittlement of aluminum alloy AA7020, Bulletin of Materials Science 2011 34:2 34 (2011) 311–321. https://doi.org/10.1007/S12034-011-0066-8.

[68] R. Casati, M. Coduri, M. Riccio, A. Rizzi, M. Vedani, Development of a high strength Al–Zn–Si–Mg–Cu alloy for selective laser melting, J Alloys Compd 801 (2019) 243–253. https://doi.org/10.1016/j.jallcom.2019.06.123.

[69] B.S. Murty, S.A. Kori, M. Chakraborty, Grain refinement of aluminium and its alloys by heterogeneous nucleation and alloying, Http://Dx.Doi.Org/10.1179/095066001225001049 47 (2013) 3–29. https://doi.org/10.1179/095066001225001049.

[70] D. Kong, C. Dong, S. Wei, X. Ni, L. Zhang, R. Li, L. Wang, C. Man, X. Li, About metastable cellular structure in additively manufactured austenitic stainless steels, Addit Manuf 38 (2021) 101804. https://doi.org/10.1016/J.ADDMA.2020.101804.

[71] J. Gockel, L. Sheridan, B. Koerper, B. Whip, The influence of additive manufacturing processing parameters on surface roughness and fatigue life, Int J Fatigue 124 (2019) 380–388. https://doi.org/10.1016/J.IJFATIGUE.2019.03.025.

[72] J. Musekamp, T. Reiber, H.C. Hoche, M. Oechsner, M. Weigold, E. Abele, Influence of LPBF-Surface Characteristics on Fatigue Properties of Scalmalloy®, Metals (Basel) 11 (2021) 1961. https://doi.org/10.3390/met11121961.

[73] T. Reiber, J. Rüdesheim, M. Weigold, E. Abele, J. Musekamp, M. Oechsner, Influence of contour scans on surface roughness and pore formation using Scalmalloy® manufactured by laser powder bed fusion (PBF-LB), Materwiss Werksttech 52 (2021) 468–481. https://doi.org/10.1002/mawe.202000287.

[74] T. Buchenau, M. Amkreutz, H. Bruening, B. Mayer, Influence of Contour Scan Variation on Surface, Bulk and Mechanical Properties of LPBF-Processed AlSi7Mg0.6, Materials 16 (2023) 3169. https://doi.org/10.3390/ma16083169.

[75] J. Fu, S. Qu, J. Ding, X. Song, M.W. Fu, Comparison of the microstructure, mechanical properties and distortion of stainless steel 316 L fabricated by micro and conventional laser powder bed fusion, Addit Manuf 44 (2021). https://doi.org/10.1016/j.addma.2021.102067.

[76] A. Chakraborty, R. Tangestani, R. Batmaz, W. Muhammad, P. Plamondon, A. Wessman, L. Yuan, É. Martin, In-process failure analysis of thin-wall structures made by laser powder bed fusion additive manufacturing, J Mater Sci Technol 98 (2022) 233–243. https://doi.org/10.1016/j.jmst.2021.05.017.

[77] A. Chakraborty, R. Tangestani, W. Muhammad, T. Sabiston, J.P. Masse, R. Batmaz, A. Wessman, É. Martin, Micro-cracking mechanism of RENÉ 108 thin-wall components built by laser powder bed fusion additive manufacturing, Mater Today Commun 30 (2022). https://doi.org/10.1016/j.mtcomm.2022.103139.

[78] R. Tangestani, T. Sabiston, A. Chakraborty, W. Muhammad, L. Yuan, É. Martin, An Efficient Track-Scale Model for Laser Powder Bed Fusion Additive Manufacturing: Part 1-Thermal Model, Front Mater 8 (2021). https://doi.org/10.3389/fmats.2021.753040.

[79] R. Tangestani, T. Sabiston, A. Chakraborty, L. Yuan, N. Krutz, É. Martin, An Efficient Track-Scale Model for Laser Powder Bed Fusion Additive Manufacturing: Part 2—Mechanical Model, Front Mater 8 (2021). https://doi.org/10.3389/fmats.2021.759669.

[80] A. Thatte, A. Loghin, E. Martin, V. Dheeradhada, Y. Shin, B. Ananthasayanam, Multi-scale coupled physics models and experiments for performance and life prediction of supercritical CO2 turbomachinery components, in: ASME, 2016.

[81] É. Martin, W. Muhammad, A.J. Detor, I. Spinelli, A. Wessman, D. Wei, "Strain-annealed" grain boundary engineering process investigated in Hastelloy-X, Materialia (Oxf) 9 (2020). https://doi.org/10.1016/J.MTLA.2019.100544.

[82] M. Ghasri-Khouzani, H. Peng, R. Attardo, P. Ostiguy, J. Neidig, R. Billo, D. Hoelzle, M.R. Shankar, Direct metal laser-sintered stainless steel: comparison of microstructure and hardness between different planes, International Journal of Advanced Manufacturing Technology 95 (2018) 4031–4037. https://doi.org/10.1007/s00170-017-1528-y.

[83] F. Belloli, A.G. Demir, B. Previtali, Understanding the deformation mechanisms of horizontal internal channels during the LPBF of 18Ni300 maraging steel, J Manuf Process 71 (2021) 237–248. https://doi.org/10.1016/j.jmapro.2021.07.063.

[84] X. Quelennec, E. Martin, L. Jiang, J.J. Jonas, Work hardening and kinetics of dynamic recrystallization in hot deformed austenite, J Phys Conf Ser 240 (2010) 012082. https://doi.org/10.1088/1742-6596/240/1/012082.

[85] J. Francis, A. Sabbaghi, M. Ravi Shankar, M. Ghasri-Khouzani, L. Bian, Efficient distortion prediction of additively manufactured parts using Bayesian model transfer between material systems, Journal of Manufacturing Science and Engineering, Transactions of the ASME 142 (2020). https://doi.org/10.1115/1.4046408.

[86] S. Li, X. Lan, Z. Wang, S. Mei, Microstructure and mechanical properties of Ti-6.5Al-2Zr-Mo-V alloy processed by Laser Powder Bed Fusion and subsequent heat treatments, Addit Manuf 48 (2021). https://doi.org/10.1016/j.addma.2021.102382.

[87] W.W. Wits, M. de Smit, K. Al-Hamdani, A.T. Clare, Laser powder bed fusion of a Magnesium-SiC metal matrix composite, Procedia CIRP 81 (2019) 506–511. https://doi.org/10.1016/j.procir.2019.03.137.

[88] É. Martin, L. Jiang, S. Godet, J.J. Jonas, The combined effect of static recrystallization and twinning on texture in magnesium alloys AM30 and AZ31, International Journal of Materials Research 100 (2009) 576–583. https://doi.org/10.3139/146.110060.

[89] J. Singh, M.-S. Kim, L. Kaushik, J.-H. Kang, D. Kim, E. Martin, S.-H. Choi, Twinning-detwinning behavior of E-form Mg alloy sheets during in-plane reverse loading, Int J Plast 127 (2020) 102637. https://doi.org/10.1016/j.ijplas.2019.11.016.

[90] T.H. Park, M.S. Baek, H. Hyer, Y. Sohn, K.A. Lee, Effect of direct aging on the microstructure and tensile properties of AlSi10Mg alloy manufactured by selective laser melting process, Mater Charact 176 (2021). https://doi.org/10.1016/j.matchar.2021.111113.

[91] S. Mondol, S. Kashyap, S. Kumar, K. Chattopadhyay, Improvement of high temperature strength of 2219 alloy by Sc and Zr addition through a novel three-stage heat treatment route, Materials Science and Engineering A 732 (2018) 157–166. https://doi.org/10.1016/j.msea.2018.07.003.

[92] M. Ghasri-Khouzani, H. Karimialavijeh, R. Tangestani, M. Pröbstle, É. Martin, Single-track study of A20X aluminum alloy fabricated by laser powder bed fusion: Modeling and experiments, Opt Laser Technol 162 (2023) 109276. https://doi.org/10.1016/J.OPTLASTEC.2023.109276.

[93] R.A. Michi, A. Plotkowski, A. Shyam, R.R. Dehoff, S.S. Babu, Towards high-temperature applications of aluminium alloys enabled by additive manufacturing, International Materials Reviews 67 (2022) 298–345. https://doi.org/10.1080/09506608.2021.1951580.

[94] B.A. Fulcher, D.K. Leigh, T.J. Watt, COMPARISON OF ALSI10MG AND AL 6061 PROCESSED THROUGH DMLS, n.d.

[95] G. Li, S.D. Jadhav, A. Martín, M.L. Montero-Sistiaga, J. Soete, M.S. Sebastian, C.M. Cepeda-Jiménez, K. Vanmeensel, Investigation of Solidification and Precipitation Behavior of Si-Modified 7075 Aluminum Alloy Fabricated by Laser-Based Powder Bed Fusion, Metall Mater Trans A Phys Metall Mater Sci 52 (2021) 194–210. https://doi.org/10.1007/s11661-020-06073-9.

[96] S.Z. Uddin, L.E. Murr, C.A. Terrazas, P. Morton, D.A. Roberson, R.B. Wicker, Processing and characterization of crack-free aluminum 6061 using high-temperature heating in laser

powder bed fusion additive manufacturing, Addit Manuf 22 (2018) 405–415. https://doi.org/10.1016/j.addma.2018.05.047.

[97] H.B. Henderson, J.A. Hammons, A.A. Baker, S.K. McCall, T.T. Li, A. Perron, Z.C. Sims, R.T. Ott, F. Meng, M.J. Thompson, D. Weiss, O. Rios, Enhanced thermal coarsening resistance in a nanostructured aluminum-cerium alloy produced by additive manufacturing, Mater Des 209 (2021). https://doi.org/10.1016/j.matdes.2021.109988.

[98] Q. Tan, J. Zhang, Q. Sun, Z. Fan, G. Li, Y. Yin, Y. Liu, M.X. Zhang, Inoculation treatment of an additively manufactured 2024 aluminium alloy with titanium nanoparticles, Acta Mater 196 (2020) 1–16. https://doi.org/10.1016/j.actamat.2020.06.026.

[99] B. Huang, Y. Liu, Z. Zhou, W. Cheng, X. Liu, Selective laser melting of 7075 aluminum alloy inoculated by Al–Ti–B: Grain refinement and superior mechanical properties, Vacuum 200 (2022) 111030. https://doi.org/10.1016/j.vacuum.2022.111030.

[100] P. Mair, L. Kaserer, J. Braun, N. Weinberger, I. Letofsky-Papst, G. Leichtfried, Microstructure and mechanical properties of a TiB2-modified Al–Cu alloy processed by laser powder-bed fusion, Materials Science and Engineering A 799 (2021). https://doi.org/10.1016/j.msea.2020.140209.

[101] N.M. Siddesh Kumar, Dhruthi, G.K. Pramod, P. Samrat, M. Sadashiva, A Critical Review on Heat Treatment of Aluminium Alloys, Mater Today Proc 58 (2022) 71–79. https://doi.org/10.1016/J.MATPR.2021.12.586.

[102] H. Zhang, Y. Wang, J.J. Wang, D.R. Ni, D. Wang, B.L. Xiao, Z.Y. Ma, Achieving superior mechanical properties of selective laser melted AlSi10Mg via direct aging treatment, J Mater Sci Technol 108 (2022) 226–235. https://doi.org/10.1016/j.jmst.2021.07.059.

[103] T.H. Park, M.S. Baek, H. Hyer, Y. Sohn, K.A. Lee, Effect of direct aging on the microstructure and tensile properties of AlSi10Mg alloy manufactured by selective laser melting process, Mater Charact 176 (2021). https://doi.org/10.1016/j.matchar.2021.111113.

[104] X. Li, D. Li, G. Li, Q. Cai, Microstructure, mechanical properties, aging behavior, and corrosion resistance of a laser powder bed fusion fabricated Al–Zn–Mg–Cu–Ta alloy, Materials Science and Engineering A 832 (2022). https://doi.org/10.1016/j.msea.2021.142364.

[105] J.C. Pereira, E. Gil, L. Solaberrieta, M. San Sebastián, Y. Bilbao, P.P. Rodríguez, Comparison of AlSi7Mg0.6 alloy obtained by selective laser melting and investment casting processes: Microstructure and mechanical properties in as-built/as-cast and heat-treated conditions, Materials Science and Engineering A 778 (2020). https://doi.org/10.1016/j.msea.2020.139124.

[106] Y. Wang, X. Lin, N. Kang, Z. Wang, Y. Liu, W. Huang, Influence of post-heat treatment on the microstructure and mechanical properties of Al-Cu-Mg-Zr alloy manufactured by selective laser melting, J Mater Sci Technol 111 (2022) 35–48. https://doi.org/10.1016/j.jmst.2021.09.036.

[107] Y. Geng, Q. Wang, Y. Wang, Q. Zang, S. Mi, J. Xu, Y. Xiao, Y. Wu, J. Luan, Microstructural evolution and strengthening mechanism of high-strength AlSi8.1 Mg1.4 alloy produced by selective laser melting, Mater Des 218 (2022). https://doi.org/10.1016/j.matdes.2022.110674.

[108] X.X. Zhang, A. Lutz, H. Andrä, M. Lahres, D. Sittig, E. Maawad, W.M. Gan, D. Knoop, An additively manufactured and direct-aged AlSi3.5Mg2.5 alloy with superior strength and ductility: micromechanical mechanisms, Int J Plast 146 (2021). https://doi.org/10.1016/j.ijplas.2021.103083.

[109] M. Laleh, E. Sadeghi, R.I. Revilla, Q. Chao, N. Haghdadi, A.E. Hughes, W. Xu, I. De Graeve, M. Qian, I. Gibson, M.Y. Tan, Heat treatment for metal additive manufacturing, Prog Mater Sci 133 (2023) 101051. https://doi.org/10.1016/j.pmatsci.2022.101051.

[110] J. Fiocchi, A. Tuissi, C.A. Biffi, Heat treatment of aluminium alloys produced by laser powder bed fusion: A review, Mater Des 204 (2021). https://doi.org/10.1016/J.MATDES.2021.109651.

[111] M. Avateffazeli, S.I. Shakil, M.F. Khan, H. Pirgazi, N. Shamsaei, M. Haghshenas, The effect of heat treatment on fatigue response of laser powder bed fused Al-Cu-Mg-Ag-TiB2 (A20X) alloy, Mater Today Commun 35 (2023). https://doi.org/10.1016/J.MTCOMM.2023.106009.

[112] M. Avateffazeli, S.I. Shakil, M.F. Khan, H. Pirgazi, N. Shamsaei, M. Haghshenas, The effect of heat treatment on fatigue response of laser powder bed fused Al-Cu-Mg-Ag-TiB2

(A20X) alloy, Mater Today Commun 35 (2023) 106009. https://doi.org/10.1016/j.mtcomm.2023.106009.

[113] ASTM E112-13, Standard Test Methods for Determining Average Grain Size, ASTM E112-13 (2021).

[114] D. Bardel, M. Perez, D. Nelias, A. Deschamps, C.R. Hutchinson, D. Maisonnette, T. Chaise, J. Garnier, F. Bourlier, Coupled precipitation and yield strength modelling for non-isothermal treatments of a 6061 aluminium alloy, Acta Mater 62 (2014) 129–140. https://doi.org/10.1016/J.ACTAMAT.2013.09.041.

[115] D. Sasamori, T. Nonaka, A. Takahashi, S. Kayano, T. Yamashita, R. Irii, T. Tanikoshi, M. Akagawa, ImageJ, U.S. National Institutes of Health, Bethesda, Maryland, USA, Http://Rsb.Info.Nih.Gov/Ij/ 69 (2009) 1225–1231. https://doi.org/10.6009/JJRT.2013_JSRT_69.11.1225.

[116] G.K. Williamson, R.E. Smallman, III. Dislocation densities in some annealed and cold-worked metals from measurements on the X-ray debye-scherrer spectrum, Https://Doi.Org/10.1080/14786435608238074 1 (2006) 34–46. https://doi.org/10.1080/14786435608238074.

[117] L. Xi, S. Guo, D. Gu, M. Guo, K. Lin, Microstructure development, tribological property and underlying mechanism of laser additive manufactured submicro-TiB2 reinforced Al-based composites, J Alloys Compd 819 (2020) 152980. https://doi.org/10.1016/j.jallcom.2019.152980.

[118] Y.K. Xiao, Z.Y. Bian, Y. Wu, G. Ji, Y.Q. Li, M.J. Li, Q. Lian, Z. Chen, A. Addad, H.W. Wang, Effect of nano-TiB2 particles on the anisotropy in an AlSi10Mg alloy processed by selective laser melting, J Alloys Compd 798 (2019) 644–655. https://doi.org/10.1016/J.JALLCOM.2019.05.279.

[119] J.C. Werenskiold, A. Deschamps, Y. Bréchet, Characterization and modeling of precipitation kinetics in an Al-Zn-Mg alloy, 2000. www.elsevier.com/locate/msea.

[120] R.A. Michi, K. Sisco, S. Bahl, L.F. Allard, K.B. Wagner, J.D. Poplawsky, D.N. Leonard, R.R. Dehoff, A. Plotkowski, A. Shyam, Microstructural evolution and strengthening

mechanisms in a heat-treated additively manufactured Al–Cu–Mn–Zr alloy, Materials Science and Engineering A 840 (2022). https://doi.org/10.1016/j.msea.2022.142928.

[121] M. Liu, N. Takata, A. Suzuki, M. Kobashi, M. Kato, Enhancement in strength and ductility of laser powder bed fused Al–12Si alloy by introducing nanoscale precipitates, Additive Manufacturing Letters 1 (2021) 100008. https://doi.org/10.1016/j.addlet.2021.100008.

[122] R. Ferragut, A. Dupasquier, C.E. Macchi, A. Somoza, R.N. Lumley, I.J. Polmear, Vacancy–solute interactions during multiple-step ageing of an Al–Cu–Mg–Ag alloy, Scr Mater 60 (2009) 137–140. https://doi.org/10.1016/J.SCRIPTAMAT.2008.09.011.

[123] P. Mair, L. Kaserer, J. Braun, N. Weinberger, I. Letofsky-Papst, G. Leichtfried, Microstructure and mechanical properties of a TiB2-modified Al–Cu alloy processed by laser powder-bed fusion, Materials Science and Engineering A 799 (2021). https://doi.org/10.1016/J.MSEA.2020.140209.

[124] S.P. Ringer, K. Hono, I.J. Polmear, T. Sakurai, Nucleation of precipitates in aged Al Cu Mg (Ag) alloys with high Cu:Mg ratios, Acta Mater 44 (1996) 1883–1898. https://doi.org/10.1016/1359-6454(95)00314-2.

[125] Q. Tan, Y. Yin, A. Prasad, G. Li, Q. Zhu, D.H. StJohn, M.X. Zhang, Demonstrating the roles of solute and nucleant in grain refinement of additively manufactured aluminium alloys, Addit Manuf 49 (2022). https://doi.org/10.1016/J.ADDMA.2021.102516.

[126] D. Drozdenko, K. Fekete, P. Dobroň, M. Knapek, K. Máthis, P. Minárik, M. Yamasaki, Y. Kawamura, The yield point phenomenon in ultrafine-grained dilute Mg-Zn-Y alloys, Mater Lett 330 (2023). https://doi.org/10.1016/j.matlet.2022.133315.

[127] M. Bishop, K.E. Fletcher, Diffusion in Aluminium, International Materials Reviews 17 (1972).

[128] V. Lacaille, C. Morel, E. Feulvarch, G. Kermouche, J.-M. Bergheau, Finite element analysis of the grain size effect on diffusion in polycrystalline materials, Comput Mater Sci 95 (2014) 187–191. https://doi.org/10.1016/j.commatsci.2014.07.026.

[129] C.A. Biffi, P. Bassani, J. Fiocchi, M. Albu, A. Tuissi, Selective laser melting of AlCu-TiB2 alloy using pulsed wave laser emission mode: processability, microstructure and

mechanical properties, Mater Des 204 (2021) 109628. https://doi.org/10.1016/j.matdes.2021.109628.

[130] F. Bakare, L. Schieren, B. Rouxel, L. Jiang, T. Langan, A. Kupke, M. Weiss, T. Dorin, The impact of L12 dispersoids and strain rate on the Portevin-Le-Chatelier effect and mechanical properties of Al–Mg alloys, Materials Science and Engineering: A 811 (2021) 141040. https://doi.org/10.1016/j.msea.2021.141040.

[131] P. He, R.F. Webster, V. Yakubov, H. Kong, Q. Yang, S. Huang, M. Ferry, J.J. Kruzic, X. Li, Fatigue and dynamic aging behavior of a high strength Al-5024 alloy fabricated by laser powder bed fusion additive manufacturing, Acta Mater 220 (2021) 117312. https://doi.org/10.1016/j.actamat.2021.117312.

[132] A.B. Spierings, K. Dawson, K. Kern, F. Palm, K. Wegener, SLM-processed Sc- and Zr-modified Al-Mg alloy: Mechanical properties and microstructural effects of heat treatment, Materials Science and Engineering A 701 (2017) 264–273. https://doi.org/10.1016/j.msea.2017.06.089.

[133] X. Nie, H. Zhang, H. Zhu, Z. Hu, Y. Qi, X. Zeng, On the role of Zr content into Portevin-Le Chatelier (PLC) effect of selective laser melted high strength Al-Cu-Mg-Mn alloy, Mater Lett 248 (2019) 5–7. https://doi.org/10.1016/j.matlet.2019.03.112.

[134] M. Avateffazeli, P.E. Carrion, B. Shachi-Amirkhiz, H. Pirgazi, M. Mohammadi, N. Shamsaei, M. Haghshenas, Correlation between tensile properties, microstructure, and processing routes of an Al–Cu–Mg–Ag–TiB2 (A205) alloy: Additive manufacturing and casting, Materials Science and Engineering A 841 (2022). https://doi.org/10.1016/J.MSEA.2022.142989.

[135] S. Zhao, C. Meng, F. Mao, W. Hu, G. Gottstein, Influence of severe plastic deformation on dynamic strain aging of ultrafine grained Al–Mg alloys, Acta Mater 76 (2014) 54–67. https://doi.org/10.1016/j.actamat.2014.05.004.

[136] T.A. Lebedkina, M.A. Lebyodkin, T.T. Lamark, M. Janeček, Y. Estrin, Effect of equal channel angular pressing on the Portevin–Le Chatelier effect in an Al3Mg alloy, Materials Science and Engineering: A 615 (2014) 7–13. https://doi.org/10.1016/j.msea.2014.07.064.

[137] X. Nie, H. Zhang, H. Zhu, Z. Hu, Y. Qi, X. Zeng, On the role of Zr content into Portevin-Le Chatelier (PLC) effect of selective laser melted high strength Al-Cu-Mg-Mn alloy, Mater Lett 248 (2019) 5–7. https://doi.org/10.1016/j.matlet.2019.03.112.

[138] F. Bakare, L. Schieren, B. Rouxel, L. Jiang, T. Langan, A. Kupke, M. Weiss, T. Dorin, The impact of L12 dispersoids and strain rate on the Portevin-Le-Chatelier effect and mechanical properties of Al–Mg alloys, Materials Science and Engineering: A 811 (2021) 141040. https://doi.org/10.1016/j.msea.2021.141040.

[139] Z. Hu, Y. Qi, X. Nie, H. Zhang, H. Zhu, The Portevin-Le Chatelier (PLC) effect in an Al-Cu aluminum alloy fabricated by selective laser melting, Mater Charact 178 (2021) 111198. https://doi.org/10.1016/j.matchar.2021.111198.

[140] A. Mogucheva, D. Yuzbekova, R. Kaibyshev, T. Lebedkina, M. Lebyodkin, Effect of Grain Refinement on Jerky Flow in an Al-Mg-Sc Alloy, Metallurgical and Materials Transactions A 47 (2016) 2093–2106. https://doi.org/10.1007/s11661-016-3381-2.

[141] X. Nie, H. Zhang, H. Zhu, Z. Hu, Y. Qi, X. Zeng, On the role of Zr content into Portevin-Le Chatelier (PLC) effect of selective laser melted high strength Al-Cu-Mg-Mn alloy, Mater Lett 248 (2019) 5–7. https://doi.org/10.1016/j.matlet.2019.03.112.

[142] T.A. Lebedkina, M.A. Lebyodkin, T.T. Lamark, M. Janeček, Y. Estrin, Effect of equal channel angular pressing on the Portevin–Le Chatelier effect in an Al3Mg alloy, Materials Science and Engineering: A 615 (2014) 7–13. https://doi.org/10.1016/j.msea.2014.07.064.

[143] L. Zhang, R.L. Narayan, H.M. Fu, U. Ramamurty, W.R. Li, Y.D. Li, H.F. Zhang, Tuning the microstructure and metastability of β-Ti for simultaneous enhancement of strength and ductility of Ti-based bulk metallic glass composites, Acta Mater 168 (2019) 24–36. https://doi.org/10.1016/j.actamat.2019.02.002.

[144] A.H.V. Pavan, R.L. Narayan, S.-H. Li, K. Singh, U. Ramamurty, Mechanical behavior and dynamic strain ageing in Haynes®282 superalloy subjected to accelerated ageing, Materials Science and Engineering: A 832 (2022) 142486. https://doi.org/10.1016/j.msea.2021.142486.

[145] N. Nayan, S.V.S. Narayana Murty, R. Sarkar, A.K. Mukhopadhyay, S. Ahlawat, S.K. Sarkar, M.J.N. V. Prasad, I. Samajdar, The Anisotropy of Serrated Flow Behavior of Al-

Cu-Li (AA2198) Alloy, Metallurgical and Materials Transactions A 50 (2019) 5066–5078. https://doi.org/10.1007/s11661-019-05431-6.

[146] L.P. Kubin, Y. Estrin, Evolution of dislocation densities and the critical conditions for the Portevin-Le Châtelier effect, Acta Metallurgica et Materialia 38 (1990) 697–708. https://doi.org/10.1016/0956-7151(90)90021-8.

[147] Z. Hu, Y. Qi, X. Nie, H. Zhang, H. Zhu, The Portevin-Le Chatelier (PLC) effect in an Al-Cu aluminum alloy fabricated by selective laser melting, Mater Charact 178 (2021) 111198. https://doi.org/10.1016/j.matchar.2021.111198.

[148] M. Okayasu, K. Ota, S. Takeuchi, H. Ohfuji, T. Shiraishi, Influence of microstructural characteristics on mechanical properties of ADC12 aluminum alloy, Materials Science and Engineering: A 592 (2014) 189–200. https://doi.org/10.1016/j.msea.2013.10.098.

[149] D. Song, G. Wang, Z. Zhou, E.E. Klu, B. Gao, A. Ma, Y. Wu, J. Sun, J. Jiang, X. Ma, Developing a high-strength Al–11Si alloy with improved ductility by combining ECAP and cryorolling, Materials Science and Engineering: A 773 (2020) 138880. https://doi.org/10.1016/j.msea.2019.138880.

[150] S. Samat, M.Z. Omar, A.H. Baghdadi, I.F. Mohamed, A. Rajabi, A.M. Aziz, Microstructural evolution, dislocation density and tensile properties of Al–6.5Si–2.1Cu–0.35Mg alloy produced by different casting processes, J Mater Sci Technol 95 (2021) 145–157. https://doi.org/10.1016/j.jmst.2021.02.074.

[151] A. Mandal, R. Maiti, M. Chakraborty, B.S. Murty, Effect of TiB2 particles on aging response of Al-4Cu alloy, Materials Science and Engineering A 386 (2004) 296–300. https://doi.org/10.1016/J.MSEA.2004.07.026.

[152] C. Bartels, D. Raabe, G. Gottstein, U. Huber, Investigation of the precipitation kinetics in an A16061/TiB2 metal matrix composite, Materials Science and Engineering: A 237 (1997) 12–23. https://doi.org/10.1016/S0921-5093(97)00104-4.

[153] M. Zhang, J. Wang, B. Wang, C. Xue, X. Liu, Quantifying the effects of Sc and Ag on the microstructure and mechanical properties of Al–Cu alloys, Materials Science and Engineering A 831 (2022). https://doi.org/10.1016/j.msea.2021.142355.

[154] P.S. De, J.Q. Su, R.S. Mishra, A stress–strain model for a two-phase ultrafine-grained aluminum alloy, Scr Mater 64 (2011) 57–60. https://doi.org/10.1016/j.scriptamat.2010.09.003.

[155] Z. Li, N. Limodin, A. Tandjaoui, P. Quaegebeur, J.-F. Witz, D. Balloy, In-situ 3D characterization of tensile damage mechanisms in A319 aluminium alloy using X-ray tomography and digital volume correlation, Materials Science and Engineering: A 794 (2020) 139920. https://doi.org/10.1016/j.msea.2020.139920.

[156] S.R. Narasimharaju, W. Zeng, T.L. See, Z. Zhu, P. Scott, X. Jiang, S. Lou, A comprehensive review on laser powder bed fusion of steels: Processing, microstructure, defects and control methods, mechanical properties, current challenges and future trends, J Manuf Process 75 (2022) 375–414. https://doi.org/10.1016/J.JMAPRO.2021.12.033.

[157] K. Nopová, J. Jaroš, O. Červinek, L. Pantělejev, S. Gneiger, S. Senck, D. Koutný, Processing of AZ91D Magnesium Alloy by Laser Powder Bed Fusion, Applied Sciences 2023, Vol. 13, Page 1377 13 (2023) 1377. https://doi.org/10.3390/APP13031377.

[158] H. Hyer, L. Zhou, G. Benson, B. McWilliams, K. Cho, Y. Sohn, Additive manufacturing of dense WE43 Mg alloy by laser powder bed fusion, Addit Manuf 33 (2020) 101123. https://doi.org/10.1016/J.ADDMA.2020.101123.

[159] M.K. Zadeh, M. Yeganeh, M.T. Shoushtari, H. Ramezanalizadeh, F. Seidi, Microstructure, corrosion behavior, and biocompatibility of Ti-6Al-4 V alloy fabricated by LPBF and EBM techniques, Mater Today Commun 31 (2022) 103502. https://doi.org/10.1016/j.mtcomm.2022.103502.

[160] C.M. Cepeda-Jiménez, F. Potenza, E. Magalini, V. Luchin, A. Molinari, M.T. Pérez-Prado, Effect of energy density on the microstructure and texture evolution of Ti-6Al-4V manufactured by laser powder bed fusion, Mater Charact 163 (2020) 110238. https://doi.org/10.1016/j.matchar.2020.110238.

[161] A. Chakraborty, R. Tangestani, K. Esmati, T. Sabiston, L. Yuan, É. Martin, Mitigating inherent micro-cracking in laser additively manufactured RENÉ 108 thin-wall components, Thin-Walled Structures 184 (2023) 110514. https://doi.org/https://doi.org/10.1016/j.tws.2022.110514.

[162] A. Chakraborty, W. Muhammad, J.-P. Masse, R. Tangestani, M. Ghasri-Khouzani, A. Wessman, É. Martin, Role of alloy composition on micro-cracking mechanisms in additively manufactured Ni-based superalloys, Acta Mater 255 (2023) 119089. https://doi.org/10.1016/j.actamat.2023.119089.

[163] A. Chakraborty, R. Tangestani, R. Batmaz, W. Muhammad, P. Plamondon, A. Wessman, L. Yuan, É. Martin, In-process failure analysis of thin-wall structures made by laser powder bed fusion additive manufacturing, J Mater Sci Technol 98 (2022) 233–243. https://doi.org/10.1016/j.jmst.2021.05.017.

[164] Q. Zhong, K. Wei, Z. Lu, X. Yue, T. Ouyang, X. Zeng, High power laser powder bed fusion of Inconel 718 alloy: Effect of laser focus shift on formability, microstructure and mechanical properties, J Mater Process Technol 311 (2023) 117824. https://doi.org/10.1016/j.jmatprotec.2022.117824.

[165] R. Tangestani, T. Sabiston, A. Chakraborty, L. Yuan, N. Krutz, É. Martin, An Efficient Track-Scale Model for Laser Powder Bed Fusion Additive Manufacturing: Part 2—Mechanical Model, Front Mater 8 (2021) 759669. https://doi.org/10.3389/FMATS.2021.759669/BIBTEX.

[166] R. Tangestani, T. Sabiston, A. Chakraborty, W. Muhammad, L. Yuan, É. Martin, An Efficient Track-Scale Model for Laser Powder Bed Fusion Additive Manufacturing: Part 1-Thermal Model, Front Mater 8 (2021) 753040. https://doi.org/10.3389/FMATS.2021.753040/BIBTEX.

[167] J. Bi, Z. Lei, Y. Chen, X. Chen, X. Qin, Z. Tian, Effect of process parameters on formability and surface quality of selective laser melted Al-Zn-Sc-Zr alloy from single track to block specimen, Opt Laser Technol 118 (2019) 132–139. https://doi.org/10.1016/j.optlastec.2019.05.008.

[168] H. Karimialavijeh, A. Chakraborty, M. Proebstle, E. Martin, Effect of Shot Peening on Fatigue Properties of A20X Fabricated by Laser Powder Bed Fusion, in: S. Wagstaff (Ed.), Light Metals 2024, Springer Nature Switzerland, Cham, 2024: pp. 278–284.

[169] R. Tangestani, A. Chakraborty, T. Sabiston, L. Yuan, M. Ghasri-Khouzani, E. Martin, Multi-scale model to simulate stress directionality in laser powder bed fusion: Application

to thin-wall part failure, Mater Des 232 (2023) 112147. https://doi.org/10.1016/j.matdes.2023.112147.

[170] R. Tangestani, T. Sabiston, A. Chakraborty, L. Yuan, N. Krutz, É. Martin, An Efficient Track-Scale Model for Laser Powder Bed Fusion Additive Manufacturing: Part 2—Mechanical Model, Front Mater 8 (2021). https://doi.org/10.3389/fmats.2021.759669.

[171] A. Chakraborty, R. Tangestani, K. Esmati, T. Sabiston, L. Yuan, É. Martin, Mitigating inherent micro-cracking in laser additively manufactured RENÉ 108 thin-wall components, Thin-Walled Structures 184 (2023) 110514. https://doi.org/10.1016/j.tws.2022.110514.

[172] A. Chakraborty, W. Muhammad, J.-P. Masse, R. Tangestani, M. Ghasri-Khouzani, A. Wessman, E. Martin, Role of alloy composition on micro-cracking mechanisms in additively manufactured Ni-based superalloys, Acta Mater 255 (2023) 119089. https://doi.org/10.1016/j.actamat.2023.119089.

[173] S.Z. Uddin, L.E. Murr, C.A. Terrazas, P. Morton, D.A. Roberson, R.B. Wicker, Processing and characterization of crack-free aluminum 6061 using high-temperature heating in laser powder bed fusion additive manufacturing, Addit Manuf 22 (2018) 405–415. https://doi.org/10.1016/j.addma.2018.05.047.

[174] C.E. Roberts, D. Bourell, T. Watt, J. Cohen, A Novel Processing Approach for Additive Manufacturing of Commercial Aluminum Alloys, Phys Procedia 83 (2016) 909–917. https://doi.org/10.1016/j.phpro.2016.08.095.

[175] G. Li, S.D. Jadhav, A. Martín, M.L. Montero-Sistiaga, J. Soete, M.S. Sebastian, C.M. Cepeda-Jiménez, K. Vanmeensel, Investigation of Solidification and Precipitation Behavior of Si-Modified 7075 Aluminum Alloy Fabricated by Laser-Based Powder Bed Fusion, Metallurgical and Materials Transactions A 52 (2021) 194–210. https://doi.org/10.1007/s11661-020-06073-9.

[176] F. Alghamdi, X. Song, A. Hadadzadeh, B. Shalchi-Amirkhiz, M. Mohammadi, M. Haghshenas, Post heat treatment of additive manufactured AlSi10Mg: On silicon morphology, texture and small-scale properties, Materials Science and Engineering: A 783 (2020) 139296. https://doi.org/10.1016/j.msea.2020.139296.

[177] X. Zhang, H. Zheng, W. Yu, A review on solidification cracks in high-strength aluminum alloys via laser powder bed fusion, Mater Today Proc 70 (2022) 465–469. https://doi.org/10.1016/J.MATPR.2022.09.366.

[178] A. Aversa, G. Marchese, A. Saboori, E. Bassini, D. Manfredi, S. Biamino, D. Ugues, P. Fino, M. Lombardi, New Aluminum Alloys Specifically Designed for Laser Powder Bed Fusion: A Review, Materials 12 (2019) 1007. https://doi.org/10.3390/ma12071007.

[179] Q. Tan, J. Zhang, Q. Sun, Z. Fan, G. Li, Y. Yin, Y. Liu, M.X. Zhang, Inoculation treatment of an additively manufactured 2024 aluminium alloy with titanium nanoparticles, Acta Mater 196 (2020) 1–16. https://doi.org/10.1016/J.ACTAMAT.2020.06.026.

[180] H. Zhang, Y. Wang, J.J. Wang, D.R. Ni, D. Wang, B.L. Xiao, Z.Y. Ma, Achieving superior mechanical properties of selective laser melted AlSi10Mg via direct aging treatment, J Mater Sci Technol 108 (2022) 226–235. https://doi.org/10.1016/j.jmst.2021.07.059.

[181] Y. Wang, X. Lin, N. Kang, Z. Wang, Y. Liu, W. Huang, Influence of post-heat treatment on the microstructure and mechanical properties of Al-Cu-Mg-Zr alloy manufactured by selective laser melting, J Mater Sci Technol 111 (2022) 35–48. https://doi.org/10.1016/J.JMST.2021.09.036.

[182] H. Karimialavijeh, M. Ghasri-Khouzani, A. Chakraborty, M. Pröbstle, É. Martin, Direct aging of additively manufactured A20X aluminum alloy, J Alloys Compd 968 (2023) 172071. https://doi.org/10.1016/j.jallcom.2023.172071.

[183] S.I. Shakil, A.S. Zoeram, M. Avateffazeli, M. Roscher, H. Pirgazi, B. Shalchi-Amirkhiz, B. Poorganji, M. Mohammadi, M. Haghshenas, Ambient-temperature time-dependent deformation of cast and additive manufactured Al-Cu-Mg-Ag-TiB2 (A205), Micron 156 (2022). https://doi.org/10.1016/J.MICRON.2022.103246.

[184] F. Jiang, L. Tang, S. Li, H. Ye, M.M. Attallah, Z. Yang, Achieving strength-ductility balance in a laser powder bed fusion fabricated TiB2/Al–Cu-Mg-Ag alloy, J Alloys Compd 945 (2023) 169311. https://doi.org/10.1016/j.jallcom.2023.169311.

[185] H. Karimialavijeh, A. Chakraborty, M. Proebstle, K. Oishi, J.-P. Harvey, E. Martin, Heat Treatment of A20X Alloy Manufactured Using Laser Powder Bed Fusion, in: S. Wagstaff (Ed.), Light Metals 2024, Springer Nature Switzerland, Cham, 2024: pp. 376–382.

[186] G. Liu, G.J. Zhang, X.D. Ding, J. Sun, K.H. Chen, Modeling the strengthening response to aging process of heat-treatable aluminum alloys containing plate/disc- or rod/needle-shaped precipitates, Materials Science and Engineering: A 344 (2003) 113–124. https://doi.org/10.1016/S0921-5093(02)00398-2.

[187] B.A. Chen, G. Liu, R.H. Wang, J.Y. Zhang, L. Jiang, J.J. Song, J. Sun, Effect of interfacial solute segregation on ductile fracture of Al–Cu–Sc alloys, Acta Mater 61 (2013) 1676–1690. https://doi.org/10.1016/J.ACTAMAT.2012.11.043.

[188] ASTM, ASTM E92-17- Standard Test Methods for Vickers Hardness and Knoop Hardness of Metallic Materials, (2023).

[189] D. Li, S. Guruvenket, S. Hassani, E. Bousser, M. Azzi, J.A. Szpunar, J.E. Klemberg-Sapieha, Effect of Cr interlayer on the adhesion and corrosion enhancement of nanocomposite TiN-based coatings deposited on stainless steel 410, Thin Solid Films 519 (2011) 3128–3134. https://doi.org/10.1016/j.tsf.2010.12.020.

[190] M. Liang, L. Chen, G. Zhao, Y. Guo, Effects of solution treatment on the microstructure and mechanical properties of naturally aged EN AW 2024 Al alloy sheet, J Alloys Compd 824 (2020) 153943. https://doi.org/10.1016/j.jallcom.2020.153943.

[191] Y. Zou, L. Cao, X. Wu, Y. Wang, X. Sun, H. Song, M.J. Couper, Effect of ageing temperature on microstructure, mechanical property and corrosion behavior of aluminum alloy 7085, J Alloys Compd 823 (2020) 153792. https://doi.org/10.1016/j.jallcom.2020.153792.

[192] S. Liu, Q. Li, H. Lin, L. Sun, T. Long, L. Ye, Y. Deng, Effect of quench-induced precipitation on microstructure and mechanical properties of 7085 aluminum alloy, Mater Des 132 (2017) 119–128. https://doi.org/10.1016/j.matdes.2017.06.054.

[193] F.J. Humphreys, M.G. Ardakani, Grain boundary migration and Zener pinning in particle-containing copper crystals, Acta Mater 44 (1996) 2717–2727. https://doi.org/10.1016/1359-6454(95)00421-1.

[194] F.N. Rhines, K.R. Craig, R.T. DeHoff, Mechanism of steady-state grain growth in aluminum, Metallurgical Transactions 5 (1974) 413–425. https://doi.org/10.1007/BF02644109.

[195] M. Takeda, Y. Maeda, A. Yoshida, K. Yabuta, S. Konuma, T. Endo, Discontinuity of G.P.(I) zone and θ′-phase in an Al-Cu alloy, Scr Mater 41 (1999) 643–649. https://doi.org/10.1016/S1359-6462(99)00137-2.

[196] Y. Zheng, Y. Liu, N. Wilson, S. Liu, X. Zhao, H. Chen, J. Li, Z. Zheng, L. Bourgeois, J.-F. Nie, Solute segregation induced sandwich structure in Al-Cu(-Au) alloys, Acta Mater 184 (2020) 17–29. https://doi.org/10.1016/j.actamat.2019.11.011.

[197] J.M. Silcock, T.J. Heal, H.K. Hardy, Structural ageing characteristics of binary aluminium-copper alloys, J. Inst. Metals 82 (1954).

[198] L.M. Wang, H.M. Flower, T.C. Lindley, Precipitation of the ω phase in 2024 and 2124 aluminium alloys, Scr Mater 41 (1999) 391–396. https://doi.org/10.1016/S1359-6462(99)00150-5.

[199] T. Gladman, Precipitation hardening in metals, Materials Science and Technology 15 (1999) 30–36. https://doi.org/10.1179/026708399773002782.

[200] J.C. Werenskiold, A. Deschamps, Y. Bréchet, Characterization and modeling of precipitation kinetics in an Al–Zn–Mg alloy, Materials Science and Engineering: A 293 (2000) 267–274. https://doi.org/10.1016/S0921-5093(00)01247-8.

[201] Q. Lu, J. Hu, T. Yang, Y. Wang, Y. Xiao, X. Li, N. Xiao, J. Wang, Z. Wang, H. Li, L. Li, K. Li, Y. Du, Revisiting the effect of Ag additions on Ω precipitation and heat resistance of Al–Cu–Mg–Si–Ag alloys, Materials Science and Engineering: A 885 (2023) 145539. https://doi.org/10.1016/j.msea.2023.145539.

[202] S.J. Kang, J.-M. Zuo, H.N. Han, M. Kim, Ab initio study of growth mechanism of omega precipitates in Al-Cu-Mg-Ag alloy and similar systems, J Alloys Compd 737 (2018) 207–212. https://doi.org/10.1016/j.jallcom.2017.12.010.

[203] R. Schwab, V. Ruff, On the nature of the yield point phenomenon, Acta Mater 61 (2013) 1798–1808. https://doi.org/10.1016/j.actamat.2012.12.003.

[204] D. Drozdenko, K. Fekete, P. Dobroň, M. Knapek, K. Máthis, P. Minárik, M. Yamasaki, Y. Kawamura, The yield point phenomenon in ultrafine-grained dilute Mg-Zn-Y alloys, Mater Lett 330 (2023) 133315. https://doi.org/10.1016/j.matlet.2022.133315.

[205] J.G. Morris, Lüders bands in Al—Mg alloys, Materials Science and Engineering 5 (1970) 299–302. https://doi.org/10.1016/0025-5416(70)90021-2.

[206] H. Conrad, Thermally activated deformation of metals, JOM 16 (1964) 582–588. https://doi.org/10.1007/BF03378292.

[207] D. Li, R.H. Wagoner, The nature of yielding and anelasticity in metals, Acta Mater 206 (2021) 116625. https://doi.org/10.1016/j.actamat.2021.116625.

[208] P. Dai, X. Luo, Y. Yang, Z. Kou, B. Huang, J. Zang, J. Ru, High temperature tensile properties, fracture behaviors and nanoscale precipitate variation of an Al–Zn–Mg–Cu alloy, Progress in Natural Science: Materials International 30 (2020) 63–73. https://doi.org/10.1016/j.pnsc.2020.01.007.

[209] A. Deschamps, G. Fribourg, Y. Bréchet, J.L. Chemin, C.R. Hutchinson, In situ evaluation of dynamic precipitation during plastic straining of an Al–Zn–Mg–Cu alloy, Acta Mater 60 (2012) 1905–1916. https://doi.org/10.1016/j.actamat.2012.01.002.

[210] M. Bignon, P. Shanthraj, J.D. Robson, Modelling dynamic precipitation in pre-aged aluminium alloys under warm forming conditions, Acta Mater 234 (2022) 118036. https://doi.org/10.1016/j.actamat.2022.118036.

[211] K. Teichmann, C.D. Marioara, K.O. Pedersen, K. Marthinsen, The effect of simultaneous deformation and annealing on the precipitation behaviour and mechanical properties of an Al–Mg–Si alloy, Materials Science and Engineering: A 565 (2013) 228–235. https://doi.org/10.1016/j.msea.2012.12.042.

[212] M. Cai, D.P. Field, G.W. Lorimer, A systematic comparison of static and dynamic ageing of two Al–Mg–Si alloys, Materials Science and Engineering: A 373 (2004) 65–71. https://doi.org/10.1016/j.msea.2003.12.035.

[213] A. Pineau, A.A. Benzerga, T. Pardoen, Failure of metals I: Brittle and ductile fracture, Acta Mater 107 (2016) 424–483. https://doi.org/10.1016/j.actamat.2015.12.034.

[214] A. Skowronek, A. Grajcar, Effect of Deformation Temperature on the Mechanical Behavior and Stability of Retained Austenite in TRIP-Assisted Medium-C Multiphase Steel, Materials 13 (2020). https://doi.org/10.3390/MA13112433.

[215] N. Hansen, Hall–Petch relation and boundary strengthening, Scr Mater 51 (2004) 801–806. https://doi.org/10.1016/J.SCRIPTAMAT.2004.06.002.

[216] K. Yang, W. Li, P. Niu, X. Yang, Y. Xu, Cold sprayed AA2024/Al2O3 metal matrix composites improved by friction stir processing: Microstructure characterization, mechanical performance and strengthening mechanisms, J Alloys Compd 736 (2018) 115–123. https://doi.org/10.1016/J.JALLCOM.2017.11.132.

[217] X. Feng, H. Liu, S. Suresh Babu, Effect of grain size refinement and precipitation reactions on strengthening in friction stir processed Al–Cu alloys, Scr Mater 65 (2011) 1057–1060. https://doi.org/10.1016/J.SCRIPTAMAT.2011.09.009.

[218] C. Genevois, A. Deschamps, A. Denquin, B. Doisneau-Cottignies, Quantitative investigation of precipitation and mechanical behaviour for AA2024 friction stir welds, Acta Mater 53 (2005) 2447–2458. https://doi.org/10.1016/J.ACTAMAT.2005.02.007.

[219] I. Le May, Relations between Yield Stress and Precipitate Size, Metal Science 8 (1974) 435–436. https://doi.org/10.1179/msc.1974.8.1.435.

[220] J. Yang, C. Liu, P. Ma, L. Chen, L. Zhan, N. Yan, Superposed hardening from precipitates and dislocations enhances strength-ductility balance in Al-Cu alloy, Int J Plast 158 (2022) 103413. https://doi.org/10.1016/j.ijplas.2022.103413.

[221] J. da Costa Teixeira, L. Bourgeois, C.W. Sinclair, C.R. Hutchinson, The effect of shear-resistant, plate-shaped precipitates on the work hardening of Al alloys: Towards a prediction of the strength–elongation correlation, Acta Mater 57 (2009) 6075–6089. https://doi.org/10.1016/j.actamat.2009.08.034.

[222] X. Shang, M.W. Fu, H. Zhang, J. Liu, X. Zhou, T. Ying, X. Zeng, Unraveling the transformation of ductile damage mechanisms of void evolution and strain localization based on deformation heterogeneity, Int J Plast 171 (2023) 103785. https://doi.org/10.1016/j.ijplas.2023.103785.

[223] A. Martucci, A. Aversa, D. Manfredi, F. Bondioli, S. Biamino, D. Ugues, M. Lombardi, P. Fino, Low-Power Laser Powder Bed Fusion Processing of Scalmalloy®, Materials 15 (2022) 3123. https://doi.org/10.3390/ma15093123.

[224] K. Schmidtke, F. Palm, A. Hawkins, C. Emmelmann, Process and Mechanical Properties: Applicability of a Scandium modified Al-alloy for Laser Additive Manufacturing, Phys Procedia 12 (2011) 369–374. https://doi.org/10.1016/j.phpro.2011.03.047.

[225] S.I. Shakil, L. González-Rovira, L. Cabrera-Correa, J. de Dios López-Castro, M. Castillo-Rodríguez, F.J. Botana, M. Haghshenas, Insights into laser powder bed fused Scalmalloy®: investigating the correlation between micromechanical and macroscale properties, Journal of Materials Research and Technology 25 (2023) 4409–4424. https://doi.org/10.1016/j.jmrt.2023.06.228.

[226] M. Rafieazad, P. Fathi, A. Nasiri, M. Haghshenas, M. Mohammadi, Isotropic corrosion performance of the newly developed L-PBF-A205 aluminum alloy, Mater Lett 291 (2021) 129541. https://doi.org/10.1016/j.matlet.2021.129541.

[227] L. Kuchariková, T. Liptáková, E. Tillová, D. Kajánek, E. Schmidová, Role of Chemical Composition in Corrosion of Aluminum Alloys, Metals (Basel) 8 (2018) 581. https://doi.org/10.3390/met8080581.

[228] Y. Kim, R.G. Buchheit, A characterization of the inhibiting effect of Cu on metastable pitting in dilute Al–Cu solid solution alloys, Electrochim Acta 52 (2007) 2437–2446. https://doi.org/10.1016/j.electacta.2006.08.054.

[229] Y. Kim, R.G. Buchheit, P.G. Kotula, Effect of alloyed Cu on localized corrosion susceptibility of Al–Cu solid solution alloys—Surface characterization by XPS and STEM, Electrochim Acta 55 (2010) 7367–7375. https://doi.org/10.1016/j.electacta.2010.06.069.

[230] Y. Baek, G.S. Frankel, Electrochemical Quartz Crystal Microbalance Study of Corrosion of Phases in AA2024, J Electrochem Soc 150 (2003) B1. https://doi.org/10.1149/1.1524172.

[231] I.L. Muller, J.R. Galvele, Pitting potential of high purity binary aluminium alloys—I. Al□Cu alloys. Pitting and intergranular corrosion, Corros Sci 17 (1977) 179–193. https://doi.org/10.1016/0010-938X(77)90044-0.

[232] J.R. Scully, D.E. Peebles, A.D. Romig, D.R. Frear, C.R. Hills, Metallurgical factors influencing the corrosion of aluminum, Al-Cu, and Al-Si alloy thin films in dilute hydrofluoric solution, Metallurgical Transactions A 23 (1992) 2641–2655. https://doi.org/10.1007/BF02658068.

[233] J.F. Li, Z. Ziqiao, J. Na, T. Chengyu, Localized corrosion mechanism of 2×××-series Al alloy containing S(Al2CuMg) and θ′(Al2Cu) precipitates in 4.0% NaCl solution at pH 6.1, Mater Chem Phys 91 (2005) 325–329. https://doi.org/10.1016/j.matchemphys.2004.11.034.

[234] Z. Wang, P. Zhang, X. Zhao, S. Rao, The Corrosion Behavior of Al-Cu-Li Alloy in NaCl Solution, Coatings 12 (2022). https://doi.org/10.3390/coatings12121899.

[235] J.R. Galvele, S.M. De Micheli, Mechanism of intergranular corrosion of Al-Cu alloys, Corros Sci 10 (1970) 795–807. https://api.semanticscholar.org/CorpusID:94095586.

[236] I.L. Muller, J.R. Galvele, Pitting potential of high purity binary aluminium alloys—I. Al□Cu alloys. Pitting and intergranular corrosion, Corros Sci 17 (1977) 179–193. https://doi.org/10.1016/0010-938X(77)90044-0.

[237] J. Li, J. Dang, A Summary of Corrosion Properties of Al-Rich Solid Solution and Secondary Phase Particles in Al Alloys, Metals 2017, Vol. 7, Page 84 7 (2017) 84. https://doi.org/10.3390/MET7030084.

[238] Y. Ren, B. Han, H. Wu, J. Wang, B. Liu, B. Wei, Z. Jiao, I. Baker, Copper segregation-mediated formation of nanotwins and 9R phase in titanium alloys produced by laser powder bed fusion, Scr Mater (2022) 115115. https://doi.org/10.1016/j.scriptamat.2022.115115.

[239] H. Yin, P. Li, Micropore-propagation-based model of fatigue life analysis of SLM manufactured Ti-6Al-4V, Int J Fatigue (2022) 107352. https://doi.org/10.1016/j.ijfatigue.2022.107352.

[240] S. Wei, P. Kumar, K.B. Lau, D. Wuu, L.-L. Liew, F. Wei, S.L. Teo, A. Cheong, C.K. Ng, B. Zhang, C.C. Tan, P. Wang, U. Ramamurty, Effect of heat treatment on the microstructure and mechanical properties of 2.4 GPa grade maraging steel fabricated by laser powder bed fusion, Addit Manuf 59 (2022) 103190. https://doi.org/10.1016/j.addma.2022.103190.

[241] M. Ghasri-Khouzani, H. Peng, R. Attardo, P. Ostiguy, J. Neidig, R. Billo, D. Hoelzle, M.R. Shankar, Direct metal laser-sintered stainless steel: comparison of microstructure and hardness between different planes, The International Journal of Advanced Manufacturing Technology 95 (2018) 4031–4037. https://doi.org/10.1007/s00170-017-1528-y.

[242] M. Ghasri-Khouzani, H. Peng, R. Attardo, P. Ostiguy, J. Neidig, R. Billo, D. Hoelzle, M.R. Shankar, Comparing microstructure and hardness of direct metal laser sintered AlSi10Mg

alloy between different planes, J Manuf Process 37 (2019) 274–280. https://doi.org/10.1016/j.jmapro.2018.12.005.

[243] A. Khorasani, I. Gibson, J.K. Veetil, A.H. Ghasemi, A review of technological improvements in laser-based powder bed fusion of metal printers, The International Journal of Advanced Manufacturing Technology 108 (2020) 191–209. https://doi.org/10.1007/s00170-020-05361-3.

[244] W. Muhammad, R. Batmaz, A. Natarajan, E. Martin, Effect of binder jetting microstructure variability on low cycle fatigue behavior of 316L, Materials Science and Engineering: A 839 (2022) 142820. https://doi.org/10.1016/j.msea.2022.142820.

[245] E. Martin, A. Natarajan, S. Kottilingam, R. Batmaz, Binder jetting of “Hard-to-Weld” high gamma prime nickel-based superalloy RENÉ 108, Addit Manuf 39 (2021) 101894. https://doi.org/10.1016/j.addma.2021.101894.

[246] E. Malekipour, H. El-Mounayri, Common defects and contributing parameters in powder bed fusion AM process and their classification for online monitoring and control: a review, International Journal of Advanced Manufacturing Technology 95 (2018) 527–550. https://doi.org/10.1007/s00170-017-1172-6.

[247] D.B. Witkin, D. Patel, T. v. Albright, G.E. Bean, T. McLouth, Influence of surface conditions and specimen orientation on high cycle fatigue properties of Inconel 718 prepared by laser powder bed fusion, Int J Fatigue 132 (2020). https://doi.org/10.1016/j.ijfatigue.2019.105392.

[248] M. Muhammad, P.D. Nezhadfar, S. Thompson, A. Saharan, N. Phan, N. Shamsaei, A comparative investigation on the microstructure and mechanical properties of additively manufactured aluminum alloys, Int J Fatigue 146 (2021) 106165. https://doi.org/10.1016/J.IJFATIGUE.2021.106165.

[249] E. Maleki, S. Bagherifard, M. Bandini, M. Guagliano, Surface post-treatments for metal additive manufacturing: Progress, challenges, and opportunities, Addit Manuf 37 (2021). https://doi.org/10.1016/j.addma.2020.101619.

[250] G. Li, X. Li, C. Guo, Y. Zhou, Q. Tan, W. Qu, X. Li, X. Hu, M.-X. Zhang, Q. Zhu, Investigation into the effect of energy density on densification, surface roughness and loss

of alloying elements of 7075 aluminium alloy processed by laser powder bed fusion, Opt Laser Technol 147 (2022) 107621. https://doi.org/10.1016/j.optlastec.2021.107621.

[251] A. Maamoun, Y. Xue, M. Elbestawi, S. Veldhuis, Effect of Selective Laser Melting Process Parameters on the Quality of Al Alloy Parts: Powder Characterization, Density, Surface Roughness, and Dimensional Accuracy, Materials 11 (2018) 2343. https://doi.org/10.3390/ma11122343.

[252] A. Majeed, A. Ahmed, A. Salam, M.Z. Sheikh, Surface quality improvement by parameters analysis, optimization and heat treatment of AlSi10Mg parts manufactured by SLM additive manufacturing, International Journal of Lightweight Materials and Manufacture 2 (2019) 288–295. https://doi.org/10.1016/j.ijlmm.2019.08.001.

[253] F. Calignano, D. Manfredi, E.P. Ambrosio, L. Iuliano, P. Fino, Influence of process parameters on surface roughness of aluminum parts produced by DMLS, The International Journal of Advanced Manufacturing Technology 67 (2013) 2743–2751. https://doi.org/10.1007/s00170-012-4688-9.

[254] J.C. Fox, S.P. Moylan, B.M. Lane, Effect of Process Parameters on the Surface Roughness of Overhanging Structures in Laser Powder Bed Fusion Additive Manufacturing, Procedia CIRP 45 (2016) 131–134. https://doi.org/10.1016/j.procir.2016.02.347.

[255] T. Mishurova, K. Artzt, J. Haubrich, G. Requena, G. Bruno, Exploring the correlation between subsurface residual stresses and manufacturing parameters in laser powder bed fused ti-6al-4v, Metals (Basel) 9 (2019). https://doi.org/10.3390/met9020261.

[256] M. Bonesso, P. Rebesan, C. Gennari, S. Mancin, R. Dima, A. Pepato, I. Calliari, Effect of Particle Size Distribution on Laser Powder Bed Fusion Manufacturability of Copper, BHM Berg- Und Hüttenmännische Monatshefte 166 (2021) 256–262. https://doi.org/10.1007/s00501-021-01107-0.

[257] T. Reiber, J. Rüdesheim, M. Weigold, E. Abele, J. Musekamp, M. Oechsner, Influence of contour scans on surface roughness and pore formation using Scalmalloy® manufactured by laser powder bed fusion (PBF-LB), Materwiss Werksttech 52 (2021) 468–481. https://doi.org/10.1002/mawe.202000287.

[258] C. Pauzon, T. Mishurova, M. Fischer, J. Ahlström, T. Fritsch, G. Bruno, E. Hryha, Impact of contour scanning and helium-rich process gas on performances of Alloy 718 lattices produced by laser powder bed fusion, Mater Des 215 (2022). https://doi.org/10.1016/j.matdes.2022.110501.

[259] J. Musekamp, T. Reiber, H.C. Hoche, M. Oechsner, M. Weigold, E. Abele, Influence of LPBF-surface characteristics on fatigue properties of Scalmalloy®, Metals (Basel) 11 (2021). https://doi.org/10.3390/met11121961.

[260] T. Yang, T. Liu, W. Liao, H. Wei, C. Zhang, X. Chen, K. Zhang, Effect of processing parameters on overhanging surface roughness during laser powder bed fusion of AlSi10Mg, J Manuf Process 61 (2021) 440–453. https://doi.org/10.1016/j.jmapro.2020.11.030.

[261] F. Calignano, D. Manfredi, E.P. Ambrosio, L. Iuliano, P. Fino, Influence of process parameters on surface roughness of aluminum parts produced by DMLS, The International Journal of Advanced Manufacturing Technology 67 (2013) 2743–2751. https://doi.org/10.1007/s00170-012-4688-9.

[262] A. Majeed, A. Ahmed, A. Salam, M.Z. Sheikh, Surface quality improvement by parameters analysis, optimization and heat treatment of AlSi10Mg parts manufactured by SLM additive manufacturing, International Journal of Lightweight Materials and Manufacture 2 (2019) 288–295. https://doi.org/10.1016/j.ijlmm.2019.08.001.

[263] A. Maamoun, Y. Xue, M. Elbestawi, S. Veldhuis, Effect of Selective Laser Melting Process Parameters on the Quality of Al Alloy Parts: Powder Characterization, Density, Surface Roughness, and Dimensional Accuracy, Materials 11 (2018) 2343. https://doi.org/10.3390/ma11122343.

[264] S.I. Shakil, A.S. Zoeram, H. Pirgazi, B. Shalchi-Amirkhiz, B. Poorganji, M. Mohammadi, M. Haghshenas, Microstructural-micromechanical correlation in an Al–Cu–Mg–Ag–TiB2 (A205) alloy: additively manufactured and cast, Materials Science and Engineering A 832 (2022). https://doi.org/10.1016/j.msea.2021.142453.

[265] C.A. Biffi, P. Bassani, J. Fiocchi, M. Albu, A. Tuissi, Selective laser melting of AlCu-TiB2 alloy using pulsed wave laser emission mode: processability, microstructure and

mechanical properties, Mater Des 204 (2021). https://doi.org/10.1016/j.matdes.2021.109628.

[266] ISO 21920-2:2021, Geometrical product specifications (GPS) — Surface texture: Profile — Part 2: Terms, definitions and surface texture parameters, 2021.

[267] ASTM E606/E606M-21, Standard Test Method for Strain-Controlled Fatigue Testing, 2021.

[268] ASTM E8/E8M-22, Standard Test Methods for Tension Testing of Metallic Materials, (2022).

[269] M. Avateffazeli, S.I. Shakil, A. Hadadzadeh, B. Shalchi-Amirkhiz, H. Pirgazi, M. Mohammadi, M. Haghshenas, On microstructure and work hardening behavior of laser powder bed fused Al-Cu-Mg-Ag-TiB2 and AlSi10Mg alloys, Mater Today Commun 35 (2023) 105804. https://doi.org/10.1016/j.mtcomm.2023.105804.

[270] M.H. Ghoncheh, M. Sanjari, A.S. Zoeram, E. Cyr, B.S. Amirkhiz, A. Lloyd, M. Haghshenas, M. Mohammadi, On the microstructure and solidification behavior of new generation additively manufactured Al-Cu-Mg-Ag-Ti-B alloys, Addit Manuf 37 (2021). https://doi.org/10.1016/J.ADDMA.2020.101724.

[271] ASTM B962-17,Standard Test Methods for Density of Compacted or Sintered Powder Metallurgy (PM) Products Using Archimedes' Principle, (2017).

[272] H. Hyer, L. Zhou, S. Park, G. Gottsfritz, G. Benson, B. Tolentino, B. McWilliams, K. Cho, Y. Sohn, Understanding the Laser Powder Bed Fusion of AlSi10Mg Alloy, Metallography, Microstructure, and Analysis 9 (2020) 484–502. https://doi.org/10.1007/s13632-020-00659-w.

[273] A. Mehta, L. Zhou, T. Huynh, S. Park, H. Hyer, S. Song, Y. Bai, D.D. Imholte, N.E. Woolstenhulme, D.M. Wachs, Y. Sohn, Additive manufacturing and mechanical properties of the dense and crack free Zr-modified aluminum alloy 6061 fabricated by the laser-powder bed fusion, Addit Manuf 41 (2021). https://doi.org/10.1016/j.addma.2021.101966.

[274] K. Kempen, L. Thijs, J. van Humbeeck, J.P. Kruth, Processing AlSi10Mg by selective laser melting: Parameter optimisation and material characterisation, Materials Science and

Technology (United Kingdom) 31 (2015) 917–923. https://doi.org/10.1179/1743284714Y.0000000702.

[275] Y. Huang, T.G. Fleming, S.J. Clark, S. Marussi, K. Fezzaa, J. Thiyagalingam, C.L.A. Leung, P.D. Lee, Keyhole fluctuation and pore formation mechanisms during laser powder bed fusion additive manufacturing, Nat Commun 13 (2022) 1170. https://doi.org/10.1038/s41467-022-28694-x.

[276] L. Englert, S. Czink, S. Dietrich, V. Schulze, How defects depend on geometry and scanning strategy in additively manufactured AlSi10Mg, J Mater Process Technol 299 (2022). https://doi.org/10.1016/j.jmatprotec.2021.117331.

[277] S. Tammas-Williams, H. Zhao, F. Léonard, F. Derguti, I. Todd, P.B. Prangnell, XCT analysis of the influence of melt strategies on defect population in Ti-6Al-4V components manufactured by Selective Electron Beam Melting, Mater Charact 102 (2015) 47–61. https://doi.org/10.1016/j.matchar.2015.02.008.

[278] S. Shrestha, K. Chou, Formation of keyhole and lack of fusion pores during the laser powder bed fusion process, Manuf Lett 32 (2022) 19–23. https://doi.org/10.1016/j.mfglet.2022.01.005.

[279] H. KYOGOKU, T.-T. IKESHOJI, A review of metal additive manufacturing technologies: Mechanism of defects formation and simulation of melting and solidification phenomena in laser powder bed fusion process, Mechanical Engineering Reviews 7 (2020) 19-00182-19–00182. https://doi.org/10.1299/mer.19-00182.

[280] C. Grosjean, J.-C. Borneat, R. Hauteville, F. Lefebvre, T. Joffre, Effects of channel contour laser strategies on fatigue properties and residual stresses of laser powder bed printed maraging steel, The International Journal of Advanced Manufacturing Technology 123 (2022) 3109–3120. https://doi.org/10.1007/s00170-022-10246-8.

[281] F. Calignano, D. Manfredi, E.P. Ambrosio, L. Iuliano, P. Fino, Influence of process parameters on surface roughness of aluminum parts produced by DMLS, International Journal of Advanced Manufacturing Technology 67 (2013) 2743–2751. https://doi.org/10.1007/s00170-012-4688-9.

[282] F. Wang, X.H. Wu, D. Clark, On direct laser deposited Hastelloy X: Dimension, surface finish, microstructure and mechanical properties, Materials Science and Technology 27 (2011) 344–356. https://doi.org/10.1179/026708309X12578491814591.

[283] A.H. Maamoun, Y.F. Xue, M.A. Elbestawi, S.C. Veldhuis, Effect of selective laser melting process parameters on the quality of al alloy parts: Powder characterization, density, surface roughness, and dimensional accuracy, Materials 11 (2018). https://doi.org/10.3390/ma11122343.

[284] B. Whip, L. Sheridan, J. Gockel, The effect of primary processing parameters on surface roughness in laser powder bed additive manufacturing, The International Journal of Advanced Manufacturing Technology 103 (2019) 4411–4422. https://doi.org/10.1007/s00170-019-03716-z.

[285] T. Zhang, L. Yuan, Understanding surface roughness on vertical surfaces of 316 L stainless steel in laser powder bed fusion additive manufacturing, Powder Technol 411 (2022) 117957. https://doi.org/10.1016/J.POWTEC.2022.117957.

[286] S.A. Khairallah, A.T. Anderson, A. Rubenchik, W.E. King, Laser powder-bed fusion additive manufacturing: Physics of complex melt flow and formation mechanisms of pores, spatter, and denudation zones, Acta Mater 108 (2016) 36–45. https://doi.org/10.1016/j.actamat.2016.02.014.

[287] R. Molaei, A. Fatemi, N. Sanaei, J. Pegues, N. Shamsaei, S. Shao, P. Li, D.H. Warner, N. Phan, Fatigue of additive manufactured Ti-6Al-4V, Part II: The relationship between microstructure, material cyclic properties, and component performance, Int J Fatigue 132 (2020) 105363. https://doi.org/10.1016/J.IJFATIGUE.2019.105363.

[288] A.J. McMillan, R. Jones, Combined effect of both surface finish and sub-surface porosity on component strength under repeated load conditions, Engineering Reports 2 (2020) e12248. https://doi.org/10.1002/ENG2.12248.

[289] C. Ye, C. Zhang, J. Zhao, Y. Dong, Effects of Post-processing on the Surface Finish, Porosity, Residual Stresses, and Fatigue Performance of Additive Manufactured Metals: A Review, Journal of Materials Engineering and Performance 2021 30:9 30 (2021) 6407–6425. https://doi.org/10.1007/S11665-021-06021-7.

[290] N. Sanaei, A. Fatemi, Analysis of the effect of surface roughness on fatigue performance of powder bed fusion additive manufactured metals, Theoretical and Applied Fracture Mechanics 108 (2020) 102638. https://doi.org/10.1016/J.TAFMEC.2020.102638.